


Spring 2012

# Fabrication and characterization of hybrid energy harvesting microdevices

Zhongcheng Gong

Follow this and additional works at: <https://digitalcommons.latech.edu/dissertations>

 Part of the [Electrical and Computer Engineering Commons](#), and the [Nanoscience and Nanotechnology Commons](#)

---

**FABRICATION AND CHARACTERIZATION  
OF HYBRID ENERGY HARVESTING  
MICRODEVICES**

by

Zhongcheng Gong, B.E., M.S.

A Dissertation Presented in Partial Fulfillment  
of the Requirement for the Degree  
Doctor of Philosophy

**COLLEGE OF ENGINEERING AND SCIENCE  
LOUISIANA TECH UNIVERSITY**

May 2012

UMI Number: 3515931

All rights reserved

INFORMATION TO ALL USERS

The quality of this reproduction is dependent upon the quality of the copy submitted.

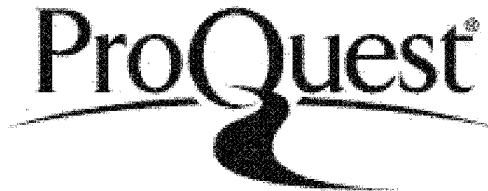
In the unlikely event that the author did not send a complete manuscript and there are missing pages, these will be noted. Also, if material had to be removed, a note will indicate the deletion.



UMI 3515931

Published by ProQuest LLC 2012. Copyright in the Dissertation held by the Author.  
Microform Edition © ProQuest LLC.

All rights reserved. This work is protected against  
unauthorized copying under Title 17, United States Code.



ProQuest LLC  
789 East Eisenhower Parkway  
P.O. Box 1346  
Ann Arbor, MI 48106-1346

LOUISIANA TECH UNIVERSITY

THE GRADUATE SCHOOL

3-2012

Date

We hereby recommend that the dissertation prepared under our supervision  
by Zhongcheng Gong

entitled Fabrication and Characterization of Hybrid Energy Harvesting Microdevices

be accepted in partial fulfillment of the requirements for the Degree of  
Doctor of Philosophy

Long Que

Supervisor of Dissertation Research

Head of Department

College of Engineering & Science

Department

Recommendation concurred in:

Chester Wilson

Hisham E. Hegab

Advisory Committee

Randal E. Null

Shengnian Wang

Approved: [Signature]  
Director of Graduate Studies

Approved: [Signature]  
Dean of the Graduate School

[Signature]  
Dean of the College

## ABSTRACT

In this dissertation, a hybrid energy harvesting system based on a lead zirconate titanate (PZT) and carbon nanotube film (CNF) cantilever structure has been designed, fabricated and studied. It has the ability to harvest light and thermal radiation energy from ambient energy and convert them to electricity.

The proposed micro-scale energy harvesting device consists of a composite cantilever beam (SU-8/CNF/Pt/PZT/Pt) which is fixed on a silicon based anchor and two electrode pads for wire bonding. The CNF acts as an antenna to receive radiation energy and convert it to heat energy and then transfer to the whole cantilever structure. The CNF will also convert the radiation energy to a non-uniform distributed static charge. These are two major reasons that cause the cantilever to bend and give the ability of cyclic bending back and forth of the cantilever. The PZT layer, in turn, converts the mechanical energy of repeated deformation of the cantilever to electricity by the piezoelectric effect.

First, the cyclic bending capability of the composite cantilever when receiving radiation energy, named self-reciprocation, has been evaluated by copper-CNF cantilever structures and the proposed mechanisms have been discussed. Based on this idea, a prototype macro-scale device with PZT and CNF integrated has been used to verify the possibility of harvesting energy from light and thermal sources by the self-reciprocation phenomenon. Open circuit voltage (OCV) output recorded from the prototype device showed continuous oscillation while a constant radiation source was presented.

The proposed micro-scale energy harvesting device was then designed and the fabrication process flow has been developed using surface and bulk micromachining techniques. The fabricated device was polarized in a strong electric field at raised temperature to boost the piezoelectric coefficient. A validation step is designed to pick out the working devices before testing. The functioned device was then tested and successfully demonstrated to harvest energy from light and thermal sources. The result showed the power density of the micro-scale device is 4,445 times higher than the macro-scale prototype device calculated from the maximum power transfer theorem.

It was found that the electric output of the micro-scale device contains not only the AC component as the prototype device but also a DC bias shift added to the AC component. An equivalent structure model of the micro-scale device was established to study the electric output characteristic. It was realized that the DC bias shift is generated from the thermoelectric effect (Seebeck effect) by controlled experiments and analysis.

The performance of the micro device was studied under different levels of light and thermal radiation conditions. The relationship between output (both DC and AC components of open circuit voltage and short circuit current) and input (light and thermal energy) were analyzed by the least square regression method.

The device was taken out of the laboratory to demonstrate its ability to harvest energy in ambient conditions. Both the DC and AC components of the open circuit voltage (electricity) were able to be generated from the solar and wind energy. The power density generated from a single device was about  $4 \mu\text{W}/\text{cm}^2$ . Further enhancement of the power density was proved by concentrating solar energy on the device with a magnifier and operating an arrayed device.

## APPROVAL FOR SCHOLARLY DISSEMINATION

The author grants to the Prescott Memorial Library of Louisiana Tech University the right to reproduce, by appropriate methods, upon request, any or all portions of this Dissertation. It is understood that "proper request" consists of the agreement, on the part of the requesting party, that said reproduction is for his personal use and that subsequent reproduction will not occur without written approval of the author of this Dissertation. Further, any portions of the Dissertation used in books, papers, and other works must be appropriately referenced to this Dissertation.

Finally, the author of this Dissertation reserves the right to publish freely, in the literature, at any time, any or all portions of this Dissertation.

Author Y. M. G. G.  
Date 3-16-2012

## TABLE OF CONTENTS

LIST OF TABLES .....	ix
LIST OF FIGURES .....	x
ACKNOWLEDGEMENTS .....	xvi
CHAPTER ONE INTRODUCTION .....	1
1.1 Renewable Energy Harvesting.....	2
1.2 Energy Harvesting Mechanisms .....	4
1.2.1 Electromagnetic Induction .....	5
1.2.2 Thermoelectric Effect .....	5
1.2.3 Photovoltaic Effect.....	7
1.2.4 Piezoelectricity.....	8
1.3 Previous Work and Problems.....	10
1.4 Dissertation Objectives .....	15
1.5 Organization of Dissertation .....	15
CHAPTER TWO CARBON NANOTUBE AND CARBON NANOTUBE FILM.....	18
2.1 Introduction.....	18
2.2 Properties of Carbon Nanotube.....	19
2.2.1 Crystal Structure .....	19
2.2.2 Mechanical Properties.....	22
2.2.3 Electrical Properties .....	22
2.2.4 Thermal Properties.....	23
2.2.5 Optical Properties.....	25
2.3 Synthesis of Carbon Nanotube Film.....	27
2.4 Carbon Nanotube Film Characteristics.....	29
2.4.1 Optical Properties of Carbon Nanotube Film .....	29
2.4.2 Photovoltaic Properties of Carbon Nanotube Film .....	30
2.5 Summary .....	32
CHAPTER THREE SELF-RECIPROCATION PHENOMENON.....	33
3.1 Overview.....	33
3.2 Observation of Self-Reciprocation Phenomenon.....	35
3.2.1 Sample Configuration .....	35



3.2.2 Experiment Setup and Testing Conditions .....	36
3.2.3 Measurements Results .....	38
3.3 Fourier Analysis.....	43
3.3.1 Discrete Fourier Transform and Fast Fourier Transform .....	43
3.3.2 Results and Analysis .....	44
3.4 Proposed Mechanism of Self-Reciprocation .....	47
3.5 Summary .....	49
CHAPTER FOUR DESIGN, FABRICATION, AND DEMONSTRATION OF MACRO- SCALE PROTOTYPES .....	51
4.1 Introduction.....	51
4.2 Prototype Design and Fabrication.....	52
4.3 Experiments Setup and Measurements .....	53
4.3.1 Displacement versus Open Circuit Voltage.....	53
4.3.2 Solar Energy Harvesting and Power Output.....	57
4.4 Disadvantage of Prototypes .....	60
4.5 Summary .....	61
CHAPTER FIVE DESIGN AND FABRICATION OF THE FIRST GENERATION MICRO-SCALE ENERGY HARVESTING DEVICE.....	62
5.1 Introduction.....	62
5.2 Device Configuration and Layout Design .....	63
5.3 Micro Fabrication Processes, Results and Discussion .....	65
5.4 Summary .....	76
CHAPTER SIX INITIAL TESTING AND ANALYSIS FOR MICRO-SCALE ENERGY HARVESTING DEVICE.....	78
6.1 Introduction.....	78
6.2 Poling and Device Validation .....	79
6.3 Experiments Details.....	81
6.4 Results and Discussion .....	83
6.5 Summary .....	89
CHAPTER SEVEN FURTHER ANALYSIS AND CONSIDERATION OF MICRO- SCALE ENERGY HARVESTING DEVICE .....	91
7.1 Analysis of DC Shift.....	91
7.2 Further Study of Micro-scale Energy Harvesting Device.....	100
7.2.1 Energy Generation under Different Radiation Conditions .....	100
7.2.2 Contribution of CNF .....	104
7.2.3 Performance in the Real Environment.....	107
7.3 Summary .....	109

CHAPTER EIGHT CONCLUSIONS AND FUTURE WORK.....	110
8.1 Conclusions.....	110
8.2 Future Work.....	116
8.2.1 Improvement of Fabrication Processes .....	116
8.2.2 Power Output Enhancement .....	117
APPENDIX A MATLAB CODE FOR FAST FOURIER TRANSFORM .....	122
REFERENCES .....	125

## LIST OF TABLES

Table 1-1	Basic renewable energy forms and sources [8] .....	3
Table 2-1	Comparison of mechanical properties [58, 59] .....	22
Table 3-1	Thickness information for each Cu-CNF cantilever .....	36
Table 3-2	Simulation results of natural resonating frequencies from ANSYS.....	45
Table 5-1	Designed thickness for each layer of the microcantilever.....	63
Table 5-2	Recipe for PZT etching in Tegal 6500 CCP system.....	69
Table 5-3	CNF thickness test from different amount of CNTs and IPA .....	69
Table 5-4	Recipe for etching CNF by ICP oxygen plasma system .....	71
Table 6-1	DC shift and maximum peak-to-peak OCV for thermal energy harvesting...87	
Table 6-2	Comparison of the macro-scale device and the micro-scale device.....	89
Table 7-1	Four conditions for micro-scale device testing .....	100
Table 7-2	Electrical characteristics for different light and thermal conditions .....	101

## LIST OF FIGURES

Figure 2-1	3D view of computer simulated single-wall CNT [56].....	20
Figure 2-2	Relationship of a SWCNT to a graphene sheet by chiral vectors [57] .....	20
Figure 2-3	Two types of SWCNT: (a) Armchair SWCNT; (b) Zigzag SWCNT [3] .....	21
Figure 2-4	Russian-doll model display of MWCNT [56].....	21
Figure 2-5	Thermal conductivity versus temperature for (10, 10) SWCNT [61].....	23
Figure 2-6	Thermal conductivity versus length of (10,10) SWCNT with different temperature [61] .....	24
Figure 2-7	Thermal conductivity versus temperature for different chirality [62] .....	24
Figure 2-8	Photon energy versus absorbance of CNT with different diameter and inset shows the Raman spectra which provide an estimation of the diameter distribution [67] .....	25
Figure 2-9	Photoluminescence map (emission wavelength versus excitation wavelength) in near infrared range of SWCNT for different chirality; from blue to red, intensity is increasing [64] .....	26
Figure 2-10	Synthesis CNF by vacuum filtration method (a) vacuum filtration system, (b) Synthesized CNF formed on MCE membrane, (c) released CNF size compared to a quarter .....	28
Figure 2-11	SEM image shows SWCNT randomly distributed in CNF. ....	28
Figure 2-12	(a) Measured reflectance from a silicon wafer and CNF on silicon at an incident angle of 90°; (b) Measured reflectance from glass and CNF on glass at an incident angle of 45° .....	30
Figure 2-13	Representative measurement of voltage generated by a CNF before, during and after the lamp is on .....	31
Figure 2-14	Representative measurement of (a) short circuit current and (b) resistance generated by a CNF before, during and after the lamp is on .....	32

Figure 3-1	(a) sketch of the Cu-CNF cantilever; (b) a photo of CNF-Cu cantilever.....	35
Figure 3-2	Experiment setup for tip displacement measurement using laser Doppler vibrometer .....	37
Figure 3-3	A representative measured (a) temperature; (b) light power for TL2 lamp (Olympus, Inc.). All the following experiments performed 5 minutes after the lamp is turn on.....	38
Figure 3-4	Representative measurements of the displacement of the tip of the Cu cantilever, Cu plus double-sided tape cantilever and CNF-Cu cantilever. The intensity of light illumination is $64 \text{ mW/cm}^2$ and thermal radiation ( $\Delta T$ ) is $17.6 \text{ }^\circ\text{C}$ .....	39
Figure 3-5	Measured self-reciprocating characteristics of CNF-Cu cantilevers with variable CNF thickness and fixed thickness ( $50 \text{ }\mu\text{m}$ ) Cu cantilever: (a) CNF thickness $5 \text{ }\mu\text{m}$ ; (b) CNF thickness $10 \text{ }\mu\text{m}$ ; (c) CNF thickness $25 \text{ }\mu\text{m}$ ; (d) CNF thickness $50 \text{ }\mu\text{m}$ .....	40
Figure 3-6	With the same CNF-Cu cantilever (Cu: $50 \text{ }\mu\text{m}$ thick, CNF: $10 \text{ }\mu\text{m}$ thick) at different light intensity and thermal radiation: (a) $14 \text{ mW/cm}^2$ , $3.9 \text{ }^\circ\text{C}$ , (b) $34 \text{ mW/cm}^2$ , $7.8 \text{ }^\circ\text{C}$ , (c) $40 \text{ mW/cm}^2$ , $16.4 \text{ }^\circ\text{C}$ , (d) $64 \text{ mW/cm}^2$ , $17.6 \text{ }^\circ\text{C}$ .....	41
Figure 3-7	With the same $100 \text{ }\mu\text{m}$ -thick Cu but different CNF thicknesses including (a) $5 \text{ }\mu\text{m}$ , (b) $10 \text{ }\mu\text{m}$ , (c) $25 \text{ }\mu\text{m}$ and (d) $50 \text{ }\mu\text{m}$ . The intensity of light illumination is $64 \text{ mW/cm}^2$ and thermal radiation ( $\Delta T$ ) is $17.6 \text{ }^\circ\text{C}$ .....	42
Figure 3-8	Procedure of signal processing for conducting Fourier analysis .....	45
Figure 3-9	Representative self-reciprocating frequencies of the CNF-Cu cantilevers (Cu: $50 \text{ }\mu\text{m}$ thick, CNF: from $10$ to $50 \text{ }\mu\text{m}$ thick) by Fourier transform of measured displacement responses under light and thermal radiations: (a) CNF $10 \text{ }\mu\text{m}$ ; (b) CNF $25 \text{ }\mu\text{m}$ ; (c) CNF $50 \text{ }\mu\text{m}$ .....	46
Figure 4-1	(a) Sketch of the prototype CNF-PZT cantilever; (b) a photo of the prototype CNF-PZT cantilever comparing with a dime dollar .....	52
Figure 4-2	Setup for measuring the real-time tip displacement and open circuit voltage of the CNF-PZT cantilever using a laser Doppler vibrometer and an oscilloscope when the cantilever exposed to light and thermal radiation.....	54

Figure 4-3	(a) Sketch of real-time displacement of a CNF-PZT cantilever upon exposure to light and thermal radiation (not to scale); (b) measured displacement in the self-reciprocation region.....	55
Figure 4-4	(a) measured OCVs with light intensity of $0.042 \text{ W/cm}^2$ and thermal radiation (temperature change) of $13.5 \text{ }^\circ\text{C}$ . The light intensity is measured at wavelength of $780 \text{ nm}$ ; (b) real-time displacement and corresponding OCV of self-reciprocation region.....	56
Figure 4-5	Optical spectrum of the Sun System SS-2MH 400 Sun Simulator (measured wavelength from $400\text{nm}$ to $1100\text{nm}$ ).....	57
Figure 4-6	Representative OCVs from solar energy harvesting using a sun simulator .....	58
Figure 4-7	Equivalent circuit of an energy harvester and the circuit with a load resistor $R_L$ for the power measurement.....	58
Figure 4-8	Measured average voltage and corresponding electrical power generated over load resistances with light intensity $0.025 \text{ W/cm}^2$ thermal radiations (temperature change) of $15 \text{ }^\circ\text{C}$ .....	59
Figure 4-9	Optimal and maximum power output from the macro scale CNF-PZT cantilever which has $30 \text{ }\mu\text{m}$ CNF with the light intensity of $0.13 \text{ W/cm}^2$ and thermal radiation (temperature change) of $22 \text{ }^\circ\text{C}$ .....	60
Figure 5-1	(a) 3D Sketch of microcantilever array; (b) cross section view of a microcantilever. (Not to scale).....	63
Figure 5-2	Top view of the energy harvesting microdevice. It consists of electrodes, anchor and cantilever .....	64
Figure 5-3	Layout design of different dimensions of energy harvesting microdevices in Tanner L-Edit .....	64
Figure 5-4	Microfabrication processes flow for energy harvesting microcantilever: (a) to (d) patterning bottom electrodes using bi-layer lift-off process; (e) thin-film PZT growth; (f) to (g) patterning top electrodes using bi-layer lift-off process; (h) to (i) etching PZT thin-film; (j) transfer CNF; (k) pattern SU-8; (l) etching CNF; (m) patterning cantilever releasing window; (n) release cantilever; (o) remove S1813.....	65

Figure 5-5	Bottom electrode is patterned on the substrate by bi-layer lift-off process .....	66
Figure 5-6	Micrograph of the whole device with bottom and top electrode and the $\text{PbTiO}_3$ plus PZT layer in between the micro-cantilever .....	68
Figure 5-7	Setup of compress loading for transferring CNF tightly onto the substrate .....	70
Figure 5-8	A photo shows CNF transferred to a patterned 4-inch silicon wafer .....	70
Figure 5-9	Etching profile of CNF (a) before etching; (b) after 15 minutes etching.....	72
Figure 5-10	Etching profile of SU-8 before and after 5 minutes etching .....	72
Figure 5-11	$\text{O}_2$ plasma ICP etching result: (a) before ICP etching; (b) after ICP etching .....	73
Figure 5-12	Micrograph of device with etching window .....	74
Figure 5-13	Micrograph of a released cantilever .....	75
Figure 5-14	SEM images of (a) one of fabricated devices showing the released cantilever and the electrodes; (b) close-up showing the released cantilever .....	76
Figure 5-15	A 3-D image showing the released microcantilever and the cavity underneath by a confocal laser scanning microscope .....	76
Figure 6-1	Poling effect for piezoelectric material. Direction of the arrows stands for the polarization direction of each unit grain in PZT crystal.....	80
Figure 6-2	A micro energy harvesting device is electrically accessed by a probe station .....	80
Figure 6-3	Experiments setup for evaluating the light and thermal energy harvesting from a single micro-energy harvesting device .....	82
Figure 6-4	Optical spectrum of Olympus TL-2 incandescent lamp .....	83
Figure 6-5	Open circuit voltage (OCV) output characteristics response to the Olympus TL-2 white light source ( $0.21 \text{ W/cm}^2$ at wavelength of $600 \text{ nm}$ ) of a single micro energy harvesting device with a released cantilever (solid line) and another device without releasing the cantilever (dashed line).....	84

Figure 6-6	OCV output for the micro energy harvesting devices.....	85
Figure 6-7	Short circuit current (SCC) output for a single device exposed to lamp .....	85
Figure 6-8	OCV of a micro device for thermal energy harvesting.....	86
Figure 6-9	OCV output for harvesting light and thermal energy from Olympus lamp (0.21 W/cm <sup>2</sup> at wavelength of 600 nm, 30 °C) and hotplate at 50 °C .....	88
Figure 7-1	Schematic diagram of the electrical output pattern from the micro-scale device .....	91
Figure 7-2	Cross-section structure sketch of the micro-energy harvesting device.....	92
Figure 7-3	(a) energy band diagram of metal and p-type semiconductor before contact; (b) energy band diagram of metal and p-type semiconductor after forming the Schottky junction when $\phi_m < \phi_s$ .....	93
Figure 7-4	Voltage generation between hot and cold ends of Si-Pt circuit from thermoelectric effect. (RT = Room Temperature).....	94
Figure 7-5	New layout design of the micro-energy harvesting device.....	95
Figure 7-6	Voltage generation from thermoelectric effect (a) irradiation on the anchor region; (b) irradiation on the bottom electrode pad region ....	96
Figure 7-7	OCV output when the irradiation is on (a) anchor region; (b) bottom electrode pad region .....	97
Figure 7-8	Equivalent structure sketch of the micro-energy harvesting device fabricated on an oxidized Si wafer .....	98
Figure 7-9	OCV output when the irradiation is on the anchor region with the device fabricated on oxidized wafer .....	99
Figure 7-10	Cantilever curled up after release with thermal SiO <sub>2</sub> as the bottom layer....	99
Figure 7-11	Relationship between (a) light intensity and DC component of OCV; (b) light intensity and AC component of OCV; (c) temperature difference and DC component of OCV; (d) temperature difference and AC component of OCV.....	102



Figure 7-12 Relationship between (a) light intensity and the DC component of SCC; (b) light intensity and the AC component of SCC; (c) temperature difference and the DC component of SCC; (d) temperature difference and the AC component of SCC.....103

Figure 7-13 Least square fitting model for (a) linear fit of light intensity and DC component of OCV; (b) 2 degree polynomial fit of light intensity and AC component of OCV.....103

Figure 7-14 Example of surface fitting of DC component of OCV with light intensity and temperature difference using first order polynomial method .....104

Figure 7-15 Control experiments to examine the contribution of CNF (a) Maximum DC shift; (b) AC oscillation.....105

Figure 7-16 Control experiments to examine the contribution of PZT (a) Maximum DC shift; (b) AC oscillation.....107

Figure 7-17 Open circuit voltage (OCV) recorded in outside environment (clear sky, temperature 87 °F, wind speed 5 mph, solar intensity 0.03 W/cm<sup>2</sup> at 780 nm and 0.33 W/cm<sup>2</sup> at 635 nm) presented in solid line; indoor environment testing without radiation energy presented in dashed line .....108

Figure 8-1 Relaxing of a composite micro cantilever by replacing thermal oxide layer to PECVD oxide and add PECVD SiN<sub>x</sub> layer [42] .....117

Figure 8-2 Sketch of the micro-lens integrated micro-energy harvesting system .....119

Figure 8-3 OCV output when focused sun light spot scans across the device. “On” stands for focused light spot on the device; “off” stands for device off focus.....119

Figure 8-4 Tandem device layout for increasing the OCV output.....120

Figure 8-5 (a) OCV output of a tandem device; (b) close-up view of AC output .....120

## ACKNOWLEDGEMENTS

I am very grateful to my advisor, Dr. Long Que, for his generous time and commitment. Throughout my doctoral work, he encouraged me to develop independent thinking and research skills. He continually stimulated my analytical thinking and greatly assisted me with scientific writing.

I am also very grateful for having an exceptional doctoral committee and wish to thank Dr. Chester Wilson, Dr. Randal E. Null, Dr. Hisham Hegab, Dr. Shengnian Wang, and for their advice and serving on my advisory committee for this dissertation.

I want to thank Dr. Chad O'Neal and his students, Joel Soman and Bo Hou, for providing helpful suggestions and advice on this research project and dissertation. I am also fortunate to have worked with my group members who are still studying here or graduated, and I would like to thank all of them for their mental and emotional support and helpful discussions and advice. They are Siva Prasad Raju, Venu Kotipalli, Shantan Talla, Tianhua Zhang, Pushparaj Pathak, Yuan He, Yi-Hsuan Tseng, Shashi Yadav. I am also grateful to IFM staff members, Mr. Ji Fang, Mr. Donald Tatum, Mr. John McDonald, Mr. Alfred Gunasekaran and Ms. Debbie Wood, for the experimental support.

I would like to thank my family. My parents and grandparents have encouraged me with their love and passion which have given me a constant support for my life. I'm appreciative to my girlfriend Jie Xiong for her care and accompany with me for all these years.

## CHAPTER ONE

### INTRODUCTION

Energy is one of the most significant resources for contemporary human society. People are consuming energy every minute in life from driving vehicles, making phone calls, getting information from networks, etc. Cheaper, cleaner, and higher efficiency energy is always desired by human beings. At present, the major energy resources used by human beings are non-renewable resources, such as fossil fuels, natural gas, etc., as they are long developed and relatively cheap to produce. However, renewable energy draws more and more attention due to its obvious advantages.

On the other hand, micro and nano technology which is under extensive research and development shows much promise for energy applications. Micro and nano technology is the study of matter in the micrometer to nanometer level ( $10^{-6}$  m to  $10^{-9}$  m). Micro and nano technology contains very broad subjects, ranging from basic research, like material science, chemistry, and physics to applications in electrical engineering, mechanical engineering, etc [1, 2]. From traditional integrated circuits which provide the function of “brain” to the whole system, scientists and researchers are also trying to develop miniaturized mechanical components to offer the system ability of the actuation and sensing, like extremities, eyes, and ears of human beings. The whole system is named as *micro/nano-electro-mechanical-system (MEMS/NEMS)*, or *micromachines* in Japan,

or micro system technology (MST) in Europe. They are very small as the name suggested. One specific branch in micro and nano technology is dedicated to energy related subjects as for instance, energy storage and energy harvesting. In energy storage, for example, numerous nanomaterials are under extensive study for enhancing the unit capacitance of the energy storage media used in capacitors or batteries and new nanomaterials are investigated for fuel cell components as a replacement for precious metal [3, 4]. On the other hand, scientists and researchers are taking advantage of micro and nano technology and by combining with traditional energy harvesting mechanisms, to open a promising area of energy harvesting to collect renewable energy from the environment [4]. Similar to integrated circuits where millions or billions of single transistors are integrated into a chip to achieve largely improved performance, the individual micro and nano level renewable energy harvesting device is also designed to work as in a large scale array to attain higher power output for realistic applications [5].

### 1.1 Renewable Energy Harvesting

In recent years, renewable energy harvesting is becoming more and more attractive for reasons such as being spontaneously replenished, cleaner, and lower and lower cost compared to non-renewable energy resources. The technology of utilizing renewable energy resources is named renewable energy harvesting, also known as renewable energy scavenging [6]. Due to their advantages over non-renewable energy resources and an exceedingly promising future, they have drawn more and more attention within both the academic community and industrial companies [7]. As we know, non-renewable energy resources, such as fossil fuel, will be eventually exhausted at the current rate of consumption. Once they are depleted, there will be no more of those

remaining on earth. Renewable energy resources, on the other hand are derived, come from natural resources, such as sunlight, geothermal heat, wind, and tides. Table 1-1 lists major types of renewable energy resources [6, 8, 9].

Renewable literally means naturally replenished. For example, solar energy is the energy resulting from nuclear fusion through the form of solar radiation which includes a broad range of electromagnetic waves. The nuclear fusion of a star, such as the sun in the solar system, is estimated to last at least tens of billions of years on the main sequence of its life, which can be treated as a perpetual energy resource [9].

Renewable energy resources are green and clean compared to non-renewable resources. For instance, solar, wind, and tide are all natural phenomena. The energy scavenging processes will not generate any byproduct to harm the environment [6]. Bioethanol made from common crops is one type of the biofuel which is a major renewable energy resource. It can be used as a fuel for a vehicle in its pure form but is mainly used as a biofuel additive for gasoline to reduce harmful emission from cars [6].

Table 1-1 Basic renewable energy forms and sources [8]

Energy forms	Sources
Mechanical energy	vibration, mechanical stress and strain
Thermal energy	waste energy from furnaces, heaters, and consumer electronics
Light energy	sunlight or all kinds of light (e.g., lamps) inside a building
E-M energy	sunlight, inductors, coils and transformers, etc
Natural energy	wind, water flow, ocean currents, breeze and solar
Human body	combination of mechanical and thermal energy naturally generated from bio-organisms or through actions such as walking and sitting
Other energy	chemical and biological sources

However, renewable energy also has some limitations. Debate about the constraints and opportunities associated with the use of renewable energy exists all the time. One of the issues is flexibility or variability. For example, a steady wind velocity is required to generate power; solar energy is only available during the day time and in good weather conditions. Some other issues include longevity and the costs of renewable energy harvesting infrastructure. Nevertheless, renewable energy resources can last for billions of years.

While debates and constraints always accompany the development of renewable energy, the market of renewable energy is expanding. In the period of economic recession from 2009, industries are pervasively weak. However, renewable energy is continuously growing thanks to the strong government funding and regulations [10].

### 1.2 Energy Harvesting Mechanisms

The term “energy harvesting” used here is the process by which energy is obtained from external sources, such as wind, sunlight, and tide, and then converted to electricity by specific mechanisms. Afterwards, electricity may be consumed immediately or stored in batteries for future use. As listed in the Table 1-1, many different types of energy forms and related sources are available [8]. These renewable energy sources for energy harvesting are freely available in the ambient background for harvest. Researchers and scientists are seeking efficient ways to capture different types of energy from hundreds of years ago. The most common and widely used mechanisms for converting renewable energy to electricity are electromagnetic induction, thermoelectric effect, photovoltaic, and piezoelectricity. Each mechanism has been studied intensively and developed for numerous applications over many decades. All of

these mechanisms have been demonstrated that efficient commercialized products could be developed successfully by engineers.

### 1.2.1 Electromagnetic Induction

The theory of electromagnetic induction was established by Michael Faraday in the year 1831 [11]. However, this phenomenon had already been observed by others. In 1820, Hans Oersted was performing a demonstration on the heating effects of electric current and noticed that a nearby compass needle deflected when current was flowing through his circuit. He had no explanation for the phenomenon, but continued to experiment with it [11]. In 1829 and again in 1830 Francesco Zantedeschi had also published papers on the production of electric currents in closed circuits by moving of a magnet, which anticipating Faraday's classical experiments [12].

Electromagnetic induction is the generation of a voltage across a conductor moving through a magnetic field. The operation of the generator, electric motor, and many other electrical machines are all based on this theory. For energy harvesting, turbine power generation from the hydraulic or wind power generator is widely used.

### 1.2.2 Thermoelectric Effect

The thermoelectric effect was observed by Thomas Seebeck in 1821. He used two dissimilar metals to form a closed circuit, which is the only way to observe the phenomenon. When the two metals are maintained at different temperatures, there was a current flow observed. William Thomson (Lord Kelvin) explained the observed effect macroscopically in 1851 [13]. After the 1930s, the microscopic understanding of the thermoelectric effect is gradually developed [14]. The thermoelectric effect was studied and developed for energy harvesting applications after its observation in 1826 [15]. The

understanding of the thermoelectric effect was constrained to macroscopic scale in the early stage. In addition, the Seebeck coefficients of materials were very small, which leads the efficiency of thermal energy harvesting was very low and not realistic for use. After the 1930s, the microscopic understanding of the thermoelectric effect boosted the development of new materials which possess much higher Seebeck coefficients [15].

The thermoelectric effect, also as known as the Seebeck effect, has been used in the thermoelectric generator which can convert heat or temperature gradient to electrical energy directly and vice-versa [13]. Electrical voltage is generated by a thermoelectric device when a temperature difference is present between two sides. The magnitude of the Seebeck effect is proportional to the Seebeck coefficient which is defined as the potential difference developed per unit temperature difference [13]:

$$S = \frac{dV}{dT}, \quad (1-1)$$

$S$  is the Seebeck coefficient;  $V$  denotes the potential difference generated;  $T$  denotes the temperature difference between two sides. By convention,  $S$  represents the potential of the cold side with respect to the hot side. The following explains the Seebeck effect at the atomic scale. An applied temperature gradient generates charged carriers in the material. Charged carriers could either be electrons or holes. Electrons diffuse from the hot end, where they have higher kinetic energy, to the cold end. The thermally induced current is generated in this process. Since the net diffusion process depends on the mean free path and mean free time which change with electron energy, the Seebeck coefficient could be either positive or negative. In one case, which the mean free path is long, electrons are accumulated at the cold side.  $S$  is then negative. In another case for which the mean free path is short, electrons are scattered by lattice vibrations more frequently and bounce



back.  $S$  is then positive. In thermoelectricity, efficiency is typically expressed as a function of the temperature over which the device is operated, referred to as the dimensionless thermoelectric figure-of-merit  $ZT$  which is expressed as in the following equation [16]:

$$ZT = \frac{S^2 T \sigma}{\mu}, \quad (1-2)$$

where  $S$  is the Seebeck coefficient,  $T$  is the average temperature difference between the hot side and the cold side,  $\sigma$  is the electrical conductivity, and  $\mu$  is the total thermal conductivity [16]. Almost all the conducting materials exhibit thermoelectric properties, but are only treated as thermoelectric material when the  $ZT > 0.5$  [17]. From  $ZT$ , we can expect that a perfect thermoelectric material should have high Seebeck coefficient, high electrical conductivity, and low thermal conductivity.

### 1.2.3 Photovoltaic Effect

The photovoltaic effect was first observed by Edmund Becquerel in 1839. He observed that electric current generated by the action of light shining on an Ag coated Pt electrode immersed in electrolyte [18]. Around 1880s, the first solid state photovoltaic device was constructed [19]. During the 1930s, the theory of metal-semiconductor barrier layers was developed by Walter Schottky, Nevile Mott and others. In the 1950s, the development of high quality silicon wafers for fabricating p-n junctions in silicon leads to much better rectifying action than the Schottky barrier which in turn yields better photovoltaic behavior [19]. The silicon based solar cell started to be used in remote areas and in space for powering satellites. At the same period of time, theoretical study indicated that III-V compound semiconductor materials offer a higher efficiency because of their band structures [19]. In the 1970s, alternative materials, such as amorphous

silicon, polycrystalline silicon, other “thin film” materials and organic conductors were explored for fabricating cheaper photovoltaic devices and improving efficiency [19]. The science of photovoltaics is primarily rooted in this time period. From the 1990s to now, awareness of the need for alternatives to the traditional fossil fuels leads to the growth of funding support for research and development of photovoltaic devices [18]. The continuous, high speed expansion of the solar cell market also reduces the cost. Currently, crystalline silicon photovoltaic cells are being partially replaced by thin-film solar cells which have significantly lower cost but lower efficiency. The demand in thin-film solar cells is rapidly growing and expected to account for 31 percent of the global installed power by 2013 [20].

The photovoltaic effect is the working mechanism for the solar cell which is currently heavily supported by government and investors since the solar cell has relatively higher efficiency and potentially low cost [21]. In quantum theory, light is made up of photons which are a packet of energy. The energy of a photon only depends on frequency which is proportional to energy. When the energy of a photon is sufficient, the electron in the valence band can be excited up to higher energy level where they are free to move and leave a vacancy in the lower energy level named a hole [22]. In a photovoltaic device, some special structures are designed to pull the excited electrons away before they relax back to their ground state to generate power [19].

#### 1.2.4 Piezoelectricity

Piezoelectricity is the direct result of the piezoelectric effect which accumulates charge in certain solid materials which are piezoelectric materials. When those materials are mechanically stressed, they become polarized and result in surface charges leading to

a voltage difference generation between the two surfaces of the material [19]. Usually, the piezoelectric effect is a reversible process. When an electric field is applied to the same material, it will exhibit mechanical strain or distortion. Piezoelectricity is defined by these two complementary effects [13].

The first direct demonstration of the piezoelectric effect was conducted by Pierre and Jacques Curie in 1880 for Rochelle salt and quartz which exhibit a surface charge when they are subjected to mechanical stress. One year later, the converse piezoelectric effect of mechanical deformation, when presented to an electric field, was deduced mathematically by Lippmann then. The complementary experiment was soon confirmed by the Curie brothers [23]. In the following decades, more and more natural crystals capable of piezoelectricity were found. By the year 1910, more than 20 natural crystals were reported to possess piezoelectricity and their piezoelectric constants were defined using tensor analysis [24]. It is worth mentioning that the practical applications of piezoelectric materials were extensively boosted during the World War I. In 1924, the idea of echo sounding using the converse piezoelectric effect was used to develop sonar, which is the first practical piezoelectric device. The successful uses of sonar led to intense research and development of piezoelectric devices [24]. New piezoelectric materials and new applications were continuously explored and developed for the following decades. Lead zirconate titanate (PZT), one of the famous piezoelectric materials which are widely used now, was invented by Yutaka Takagi, Gen Shirane and Etsuro Sawaguchi at the Tokyo Institute of Technology, around 1952 [25]. Cady, who was attracted by the attempts to generate ultrasound waves, dedicated his whole career to the research of piezoelectricity. He published all his results in 1964 and was honored as

the “father of modern piezoelectricity” [24]. Piezoelectric sensors and transducers were manufactured in Europe, USA, Japan and China and gained more and more popularity in a multitude of practical applications worldwide [24]. As we learned, the applications for energy harvesting are one of the most significant. In the next section, more details will be given for the energy harvesting of piezoelectricity.

### 1.3 Previous Work and Problems

As discussed above, continuous research and steady improvement for realizing higher efficiency energy harvesting devices or equipment utilizing each of the energy harvesting mechanisms are underway. The hybrid energy harvesting micro device will mainly relate to three of the aforementioned mechanisms including the photovoltaic, thermoelectric, and piezoelectric effect. Development and improvement for each of these technologies are going to be reviewed in the following sections.

The photovoltaic mechanism is mainly utilized in a solar panel, which is also known as a photovoltaic panel or photovoltaic module, and consists of an array of solar cells. Solar cells are classified into three generations which indicate the order of significance in terms of cost and efficiency.

The first generation solar cells are high-cost and high-efficiency. Extremely pure silicon is used for fabricating the single junction for absorbing the energy of photons and extracted as electric energy at very high efficiency [19]. The high efficiency here is comparing with the theoretical limitation of a single-junction solar cell named the Shockley-Queisser limit or detailed balance limit, which is from 31% to 41% depending on the concentration of incoming light. The Shockley-Queisser limit was first calculated by William Shockley and Hans Queisser at Shockley Semiconductor in 1961 [26]. The

first generation technologies are still the major commercial production which accounts for at least 85% of all solar cells manufactured [20].

The second generation solar cell is developed from the 1970s [19]. It is based on the use of thin-film deposits of semiconducting materials since single crystal materials are expensive to produce. Development of the thin-film based solar cell is not aimed at getting higher efficiency, but to achieve lower manufacturing cost so that a lower cost per watt can be achieved. Due to this reason, thin-film solar cell modules could be mass produced and have been adopted more and more even though the efficiency is typically lower than the first generation silicon based solar cells [20]. Plenty of semiconductor materials have been investigated to produce thin-film solar cell including amorphous silicon (a-Si), polycrystalline cadmium telluride (CdTe), polycrystalline copper indium diselenide (CuInSe<sub>2</sub>) and microcrystalline thin-film silicon (p-Si) [19]. These materials are cheaper to produce and can be applied to large areas by fast chemical or physical deposition techniques.

As stated previously, the efficiency of the p-n junction based solar cell has a limitation of 33.7% assuming a band gap of 1.1 eV, which is called the Shockley-Queisser limit or detailed balance limit [26]. The third generation solar cells, including a group of newly developed concepts, are mainly centered on nano technologies which aim to exceed this limit. These technologies encompassing multi-junction cells [27], intermediate-band cells [28], hot carrier cells [29] and spectrum conversion technology [30] are very promising though they are still under development in lab environments [21].

The thermoelectric effect is used to develop thermoelectric generators (TEGs) for generating small amounts of electricity in the range of  $\mu\text{W}$  to  $\text{mW}$  [31]. The

thermoelectric effect was observed by Thomas Seebeck in 1821 and practical thermoelectric devices emerged in the 1960's [24]. Until recently, thermoelectric generators have been still confined to very limited applications, since the most significant drawback of thermoelectric devices is the low efficiency and low thermoelectric figure-of-merit ( $ZT$ ) when compared with other technologies [32]. Most of the researches are focused on novel material synthesis for improving the thermoelectric figure-of-merit and reducing the cost of thermoelectric material [33, 34]. The research shows that low dimensional structures, such as 2D quantum wells, 1D quantum wires or nanowires, and quantum dots will offer a way to significantly improve thermoelectric figures-of-merit [35]. However, the most recent research found that the "the smaller the better" is not always the case. Researchers have demonstrated that in a set of nanowires which have a radius less than 17nm, decreasing their radii does give rise to an improvement in thermoelectric performance. However, for nanowires which have radii above 17nm, improvement has also been found as the radius increases [36]. TEGs have been developed for replacing the battery for powering some small scale microelectronic devices, which have small power consumption in the range. A TEG device based on silicon technology was developed by H. Glosch which can generate power in the range of  $1.5 \mu\text{W}$  with a temperature difference of  $10^\circ\text{C}$  for operating a small preamplifier and a sensor control system [37]. Thermoelectric devices based on thin-film technology (TFTEGs) have been developed and studied to further improve the efficiency and overcome the fragiling problem of those thermoelectric materials when making miniaturized modules [38]. The power generated by thin-film based devices has been pushed to the milliwatt range and have started to be commercialized [32].

The piezoelectric effect was studied for energy harvesting relatively late, since the 1990's [24]. An initial experiment was conducted for examining the possibility of harvesting energy using the piezo effect and the analysis of the relationship between the input mechanical impact energy and the output electric energy by dropping a steel ball which has the weight of 5.5 grams from 20mm above a piezoelectric transducer. Most of the energy is returned to the free falling ball as kinetic energy when it bounces back. If the ball stuck to the piezoelectric transducer, 52% efficiency will be achieved [39]. The piezoelectric effect was also considered to harvest energy from human body movement, such as walking, breathing, and even blood pressure. 8.4 watts of power was estimated to be achieved from a PZT mounted shoe [23]. How the energy generated by a piezoelectric device can be used for charging different types of capacitors and batteries was studied in 1997 for the first time. They found that the ability of the piezoelectric device to charge the capacitors depended upon its initial voltage and the capacitance of the capacitor. But, for charging batteries, the charging characteristics were unaffected by different types of battery or capacity [40]. Development of the cantilever-based piezoelectric energy harvester started around the year 2000. Piezoelectric material is integrated as a layer of the cantilever structure which is suitable for harvesting alternating mechanic energy, such as vibration energy, from the strain of the piezoelectric layer.  $D_{31}$  configuration is usually used in the device which has the piezoelectric layer sandwiched in between the top and bottom electrode layers since it was easier to manufacture in the early stage [41]. In 2001, Glynne-Jones, et. al. had developed a tapered thick-film PZT generator with a macro scale cantilever beam structure. It confirmed the concept of generating continuous power with a piezoelectric cantilever structure which can produce an output power of 3  $\mu$ W and

had the potential to be much higher [5]. The micro scale MEMS cantilever structure was developed around 2005 for higher energy density [41]. A piezoelectric micro cantilever structure with  $d_{33}$  arrangement was reported by Y.B. Jeon, et. al. The  $d_{33}$  coefficient of the PZT is typically 2 times larger than the  $d_{31}$ , theoretically. One single device can generate power of  $1.01 \mu\text{W}$  at its resonance frequency of 13.9 kHz when a 14nm displacement is present [42]. All of these structures mentioned above need mechanical energy, such as external environment vibration to operate. Cantilever based piezoelectric device has also been evaluated to couple with radioactive sources to achieve excitation and self-reciprocating without ambient vibrations. However, the average output power from this method is typically very low, in the range of less than 1 nW [43].

Hybrid energy harvesting devices, which can utilize more than one of the aforementioned energy generation mechanisms, has started to be considered and developed only in the recent years. Since it harnesses energy from different energy sources using multiple energy generation mechanisms, a broad adaptability and potentially higher efficiency for these kinds of devices are anticipated. A hybrid cell for concurrently harvesting both solar and mechanical energies was developed by Zhonglin Wang's research group. In this device, aligned ZnO nanowires coated with dye form a thin-film solar cell above the silicon substrate and the underside is a jagged array of polymer coated ZnO nanowires in a tooth like configuration which have the piezo effect for harvesting mechanical energies. This design was the first nano scale hybrid energy harvesting device of its kind to harvest two types of energies and it can work both under light and dark conditions [44]. Recently, Fujitsu laboratories Ltd., a Japanese company, have announced a new type of hybrid energy harvesting device for generating electricity



from heat and light. The device consists of two types of semiconductor materials: p-type and n-type semiconductors. By changing the circuit connections, the device can work in photovoltaic or thermoelectric mode for harvesting both energies. Further development of this technology is needed and is expected to be commercialized around 2015 [45].

#### 1.4 Dissertation Objectives

The aim of this dissertation research is to develop and investigate a novel hybrid energy harvesting system which is able to generate power continuously from both light and thermal radiation. First, a unique phenomenon named self-reciprocation will be introduced and demonstrated. Then, a carbon nanotube film (CNF) and lead zirconate titanate (PZT) based macro scale energy harvesting device will be demonstrated to harvest multiple-type energies. Based on this concept, a micro scale device will be developed including the design, fabrication process, and characterization. Further consideration for how to optimize the design and improve the performance will be analyzed last.

#### 1.5 Organization of Dissertation

Chapter One introduces renewable energy harvesting and reviews the investigation and development of four major energy harvesting mechanisms. They are electromagnetic induction, thermoelectric effect, photovoltaic, and piezoelectricity. Related work for developing energy harvesting technology that utilize photovoltaic, thermoelectric, and piezoelectricity has been reviewed. Their advantages and disadvantages have been investigated by comparing previous work. Most recent

examples of research on hybrid energy harvesting systems and their future have been presented.

Chapter Two covers the knowledge of the carbon nanotube (CNT). As a relatively new type of nano material, it has many excellent properties and advantages. The crystal structure, mechanical, electrical, thermal, and optical properties of CNT will be covered and discussed. The method for synthesis of carbon nanotube film (CNF), which is a unique nanomaterial made of a network of CNT using a vacuum filtration method will be described. In the following, the optical and photovoltaic properties of CNF will be studied to show its potential in energy harvesting applications.

Chapter Three will introduce a newly discovered phenomenon, self-reciprocation, which is the key for the energy harvesting system. Composite cantilever structures integrated with CNF will be designed to demonstrate this unique phenomenon. Detailed experimental procedure is conducted to study the characteristics of self-reciprocation. The mechanism of self-reciprocation will be proposed.

Based on the self-reciprocation phenomenon, a prototype macro-scale energy harvesting cantilever device is introduced and demonstrated for harvesting light and thermal energy in Chapter Four.

Chapter Five will discuss the design, fabrication techniques and results for the micro-scale energy harvesting device.

Chapter Six will describe the way to polarize and validate a micro device. Then, initial testing will be done on the working device to demonstrate its ability to harvest energy from light and thermal sources. A comparison of the performance between macro-scale and micro-scale device will be presented.

Further analysis and considerations will be addressed in Chapter Seven. The characteristics of the electrical output will be explained and discussed. The performance of the micro-device at different levels of light and thermal radiation will be studied.

Lastly, Chapter Eight will give the conclusion and summary for the whole dissertation. The future work for improvement of the fabrication and performance will be discussed.

## CHAPTER TWO

### CARBON NANOTUBE AND CARBON NANOTUBE FILM

#### 2.1 Introduction

This work is intimately related to a novel nano material which is named carbon nanotube film (CNF) made from carbon nanotubes (CNTs). CNT was first discovered in 1991 in Japan [46, 47]. Intensive research on CNT found that it has many advanced and unique properties over other traditional materials, such as high mechanical strength, extraordinary thermal and electrical conductivity, which give CNT great potential for applications in many fields, such as electrochemical devices, hydrogen storage for batteries, field emission devices, nanoscale electronic devices, sensors, probes, and energy harvesting [48, 49]. The network of CNT forms a unique nano material which is named carbon nanotube film (CNF). CNF also provides unusual mechanical, electrical, thermal, and optical characteristics. Researchers have demonstrated its multifunctional properties for making electrodes as a replacement for ITO [50], planar sources of polarized broad-band radiation, flexible organic light-emitting diodes [51], actuator [52], and bolometer [53]. Some of them have already been commercialized. Since CNT and CNF are relatively newly discovered, developed, and exhibit predictable excellent properties, there is continuous interest for researchers all around the world to explore new properties and applications.

## 2.2 Properties of Carbon Nanotube

Carbon nanotubes (CNTs) have generated an intense interest among the researchers, scientists and industries since their discovery and with their outstanding properties. They have remarkable electrical, mechanical properties and thermal properties. Carbon nanotubes can be visualized as rolled graphene sheets which sometimes are capped at each end. They are mainly classified into two types. Single-walled carbon nanotubes (SWCNTs) which are made of a single atomic layer of graphene sheet with diameters as small as 0.4 nm and multi-walled carbon nanotubes (MWCNTs) which consist of 2 to 20 concentric tubes one inside the other with outer diameters ranging from 5 to 100nm. CNTs can have lengths ranging from a few micrometers to several micrometers [48, 54]. The nanotubes can be produced by different manufacturing processes for instance arc discharge, laser ablation, chemical vapor deposition (CVD) etc. Arc discharge and laser ablation methods require high temperature and the chirality and purity of nanotubes are difficult to control. CVD process can be used to produce high purity nanotubes with different diameters and structures [55].

### 2.2.1 Crystal Structure

CNTs are classified as single-wall carbon nanotubes (SWCNTs) and multi-wall carbon nanotube (MWCNTs). Figure 2-1 shows the crystal structure of the computer simulated 3D image of one SWCNT [56]. It is actually formed from one atomic layer of graphite known as graphene, which is rolled up into a seamless cylindrical structure. The bonding between carbon atoms of SWCNT is composed of  $sp^2$  hybrid bonds. But, they are not exactly  $sp^2$  bonds since they are not planar as in graphite. The angle between two

$sp^2$  bonds is changed due to the wrapping process [57]. This type of unique bond will give CNT some excellent properties.

The graphene sheet can be rolled along different directions which are defined as the chiral vector or simply chirality. It is represented by a pair of indices  $(n, m)$ .



Figure 2-1 3D view of computer simulated single-wall CNT [56].

Figure 2-2 shows the diagram of the chiral vector [57]. If the wrapping direction is along  $(n, n)$ , it has a specific name of armchair SWCNT, as in Figure 2-3 (a). Similarly, wrapping along  $(n, 0)$  is named Zigzag SWCNT, which is showed in Figure 2-3 (b).

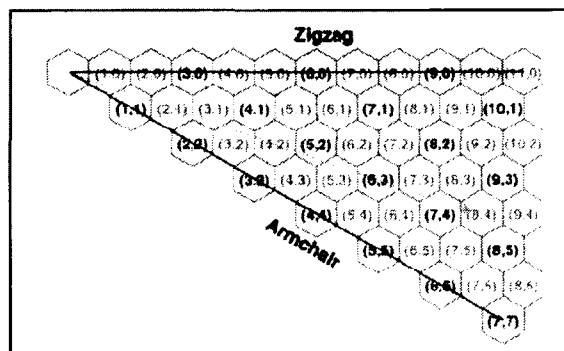


Figure 2-2 Relationship of a SWCNT to a graphene sheet by chiral vectors [57].

Multi-walled nanotubes (MWNT) consist of multiple rolled layers of graphite. The interlayer distance in multi-walled nanotubes is close to the distance between graphene layers in graphite, approximately 3.3 Å. There are two models which can be used to describe the structures of multi-walled nanotubes. One is called the Russian doll model which has the sheets of graphite are arranged in concentric cylinders, as shown in Figure 2-4. Another is named the parchment model. It is a single sheet of graphite rolled in around itself, resembling a scroll of parchment or a rolled newspaper [56].

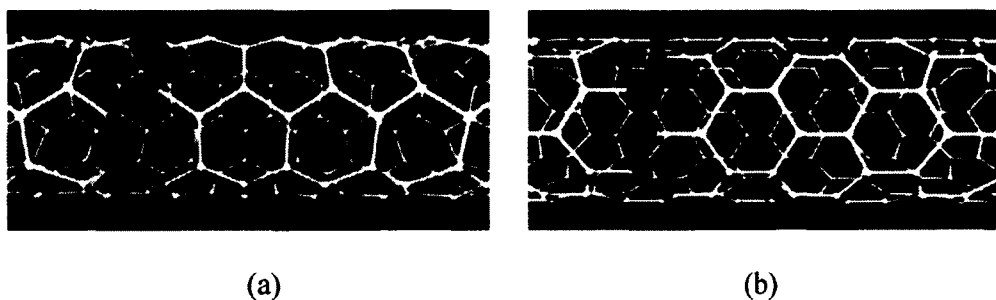


Figure 2-3 Two types of SWCNT: (a) Armchair SWCNT; (b) Zigzag SWCNT [3].

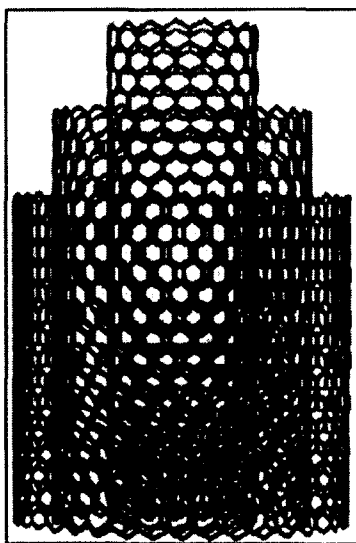


Figure 2-4 Russian-doll model display of MWCNT [56].

### 2.2.2 Mechanical Properties

The data in the Table 2-1 referred to the axial properties of the nanotube [58, 59]. The bonding structure of  $sp^2$  bonds, which is stronger than the  $sp^3$  bonds found in diamond, provides the CNT with their unique strength [57]. Compared to stainless steel, the data shows that the CNT has much better mechanical properties. Simple geometrical considerations suggest that carbon nanotubes should be much softer in the radial direction than along the tube axis. CNTs are indeed rather soft in the radial direction. Even Van der Waals force can bend CNT from its radial direction [59].

Table 2-1 Comparison of mechanical properties [58, 59]

Material	Young's Modulus (TPa)	Tensile Strength (GPa)
Arm Chair SWNT	0.94	126.2
Zigzag SWNT	0.94	94.5
MWNT	0.92	11 to 150
Stainless Steel	0.2	0.65 to 3

### 2.2.3 Electrical Properties

Because of the symmetry and unique electronic structure of graphene, the structure of a nanotube strongly affects its electrical properties. For a given  $(n, m)$  nanotube, if  $n = m$ , the nanotube is metallic and it is thought to be ballistic. Ballistic means its resistance is independent from the length due to the expected small number of defects, which means very long mean-free path. Because of the reduced scattering, metallic SWNTs can transport huge current densities (up to  $10^9$  A/cm<sup>2</sup>) without being damaged, about three orders of magnitude higher than in Cu [56].

If  $n - m$  is a multiple of 3, then the nanotube is semiconducting with a very small band gap, otherwise the nanotube is a moderate semiconductor. Their conductivity has



been shown to be a function of their chirality, the degree of twist as well as their diameter. The details of electronic properties of SWNTs are not well understood yet, and numerous theoretical and experimental works have revealed fascinating effects. The typical mobility of SWNT is  $1000\text{--}10000\text{ cm}^2/(\text{V}\cdot\text{s})$  for CVD-grown nanotubes, with occasional devices having mobility as high as  $20000\text{ cm}^2/(\text{V}\cdot\text{s})$ . This result is better than Si MOSFETs, indicating that SWNTs are a remarkably high-quality semiconducting material [60].

#### 2.2.4 Thermal Properties

Thermal conductivity in CNT is mainly due to phonons rather than electrons so the Wiedemann–Franz–Lorenz law is not applicable [61]. The thermal conductivity in CNT is dependent on temperature, length, diameter and chirality as in Figure 2-5 and Figure 2-6. Differences in chirality may lead to variations up to 20% between different tubes as in Figure 2-7. The different structure of CNT comes from different fabrication conditions and different simulation models always turn out different results [62].

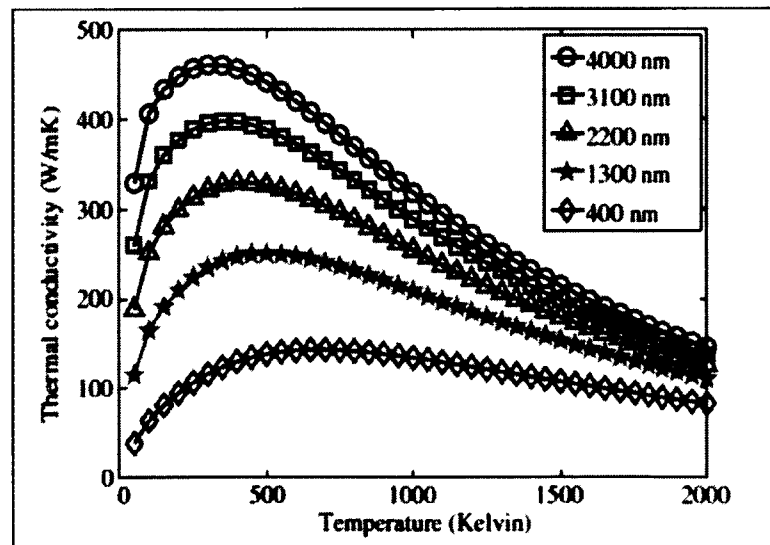


Figure 2-5 Thermal conductivity versus temperature for (10, 10) SWCNT [61].

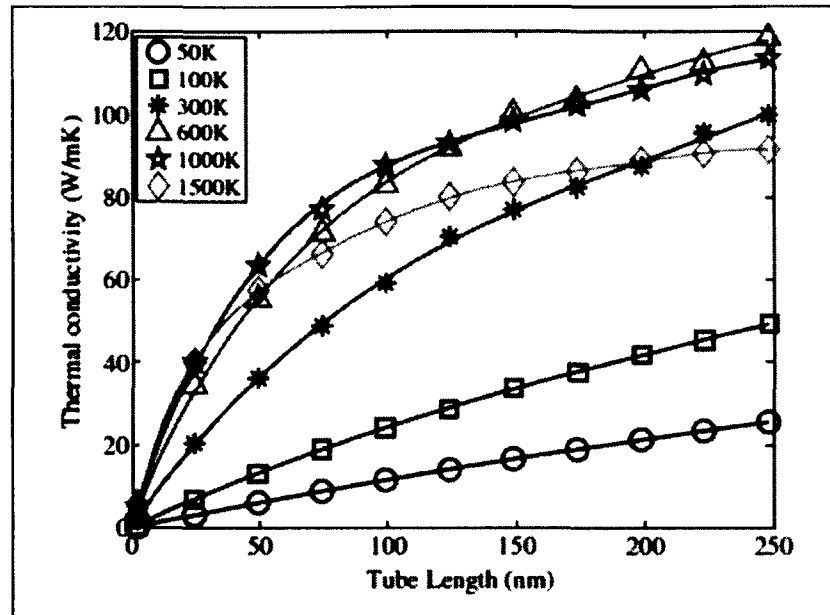


Figure 2-6 Thermal conductivity versus length of (10,10) SWCNT with different temperature [61].

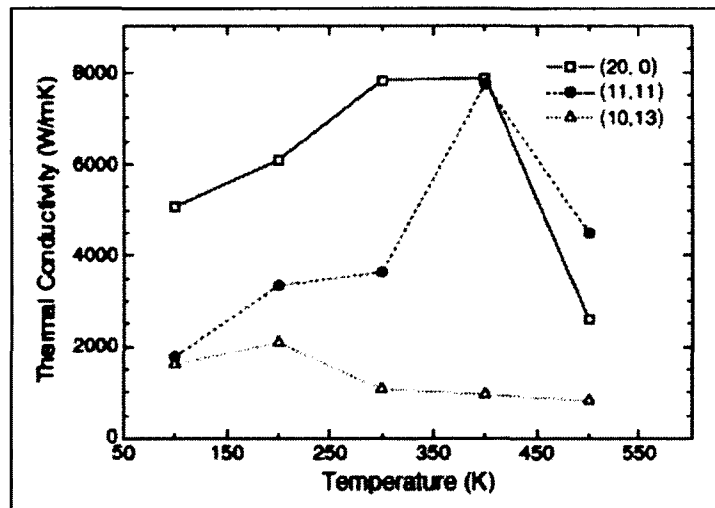


Figure 2-7 Thermal conductivity versus temperature for different chirality [62].

Some measurements show SWNTs typical room temperature thermal conductivity to be about 3500 W/(m·K), and over 3000 W/(m·K) for individual MWNTs. Copper is 390 W/(m·K) in comparison [61].

### 2.2.5 Optical Properties

Traditionally, the optical properties of carbon nanotubes refer specifically to the Raman spectroscopy, absorption, and photoluminescence of carbon nanotubes in material science [57, 64, 65].

The inset of Figure 2-8 shows the Raman spectra of CNT. Raman shift of CNT can be used to estimate the quality of CNT, like tube diameter, and whether the tube is metallic or semiconducting, etc. [67].

The absorption of an ideal black body should be 1.0, which is difficult to attain in practice, especially over a wide spectral range. Vertically aligned "forests" of single-wall carbon nanotubes can have absorbance of 0.98–0.99 from the far-ultraviolet (200 nm) to far-infrared (200  $\mu\text{m}$ ) wavelengths [66].

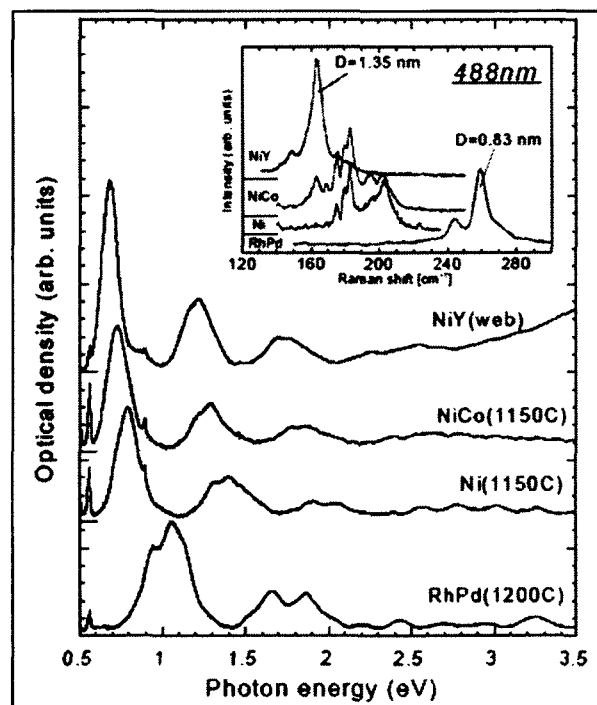


Figure 2-8 Photon energy versus absorbance of CNT with different diameter and inset shows the Raman spectra which provide an estimation of the diameter distribution [67].

For the photoluminescence, the SWCNT has narrow selectivity in the wavelength of emission and detection of light and the possibility of fine tuning through the structure (chirality). Figure 2-9 shows the photoluminescence map in near infrared range. SWCNT with different chirality has the specific excitation wavelength and related emission wavelength relative to their structure [64].

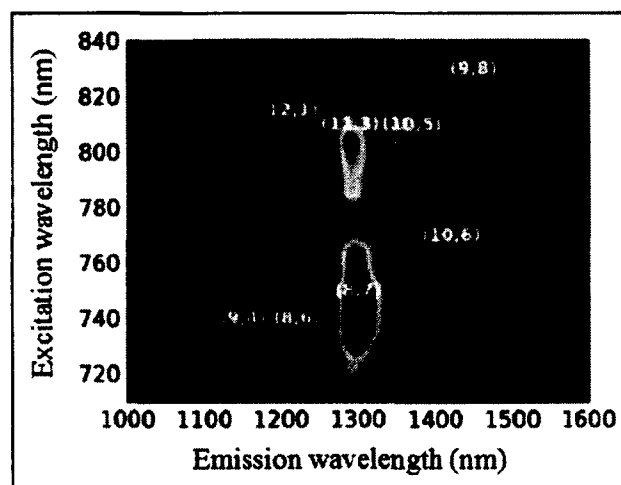


Figure 2-9 Photoluminescence map (emission wavelength versus excitation wavelength) in near infrared range of SWCNT for different chirality; from blue to red, intensity is increasing [64].

The individual semiconducting SWCNT also shows photovoltaic properties. The photons with energy greater than the bandgap generate excitons, which are pairs of electrons and holes linked by binding energy in the CNT, can decay into free electrons and holes by several ways, such as externally applied bias [68], at p-n junctions [69], at defects[70], or internal fields at Schottky barriers [71].

### 2.3 Synthesis of Carbon Nanotube Film

The CNF is synthesized using a vacuum filtration method [72]. CNT that we used for synthesis of CNF is AP-SWCNT purchased from *Carbon Solutions*. The thickness of the CNF can be precisely controlled in the nanoscale by the concentration and volume of the mixture solution. The following describes the general procedures. Around 30% of the weight is the metallic form and the remainder is supposed to be semiconducting. The carbonaceous purity is around 60-70% indicated from the manufacturer's product specifications.

CNT are immersed in Isopropyl alcohol (IPA) to obtain final concentrations in the range of 0.10 mg/ml - 0.40 mg/ml. The weight of CNT and volume of IPA should be calculated and determined beforehand. The mixture is then agitated in an ultrasonicator for about 12 hours to ensure uniform dispersion of the SWCNTs. The dispersed SWCNTs in the IPA are vacuum filtered through a Whatman ME-24 mixed cellulose ester (MCE) membrane. The MCE membrane is 48mm in diameter and pore size is around 200 nm. The whole filtration process is homogeneous. As the region of deposition become thicker because of the accumulation of CNF, the permeation rate is reduced and so is the deposition rate. More CNT-IPA solution will flow to the thinner deposition region so those areas are catching up in thickness. The obtained CNF is then rinsed with IPA and deionized water several times, and afterward it is dried for 5 hours on the vacuum filtration system. The MCE membrane is dissolved by several acetone baths and rinsed by IPA. Typical thicknesses of the resulting released CNF for the energy harvesting applications are in the range of 1-100  $\mu\text{m}$ . The setup and prepared CNF are shown in Figure 2-10.

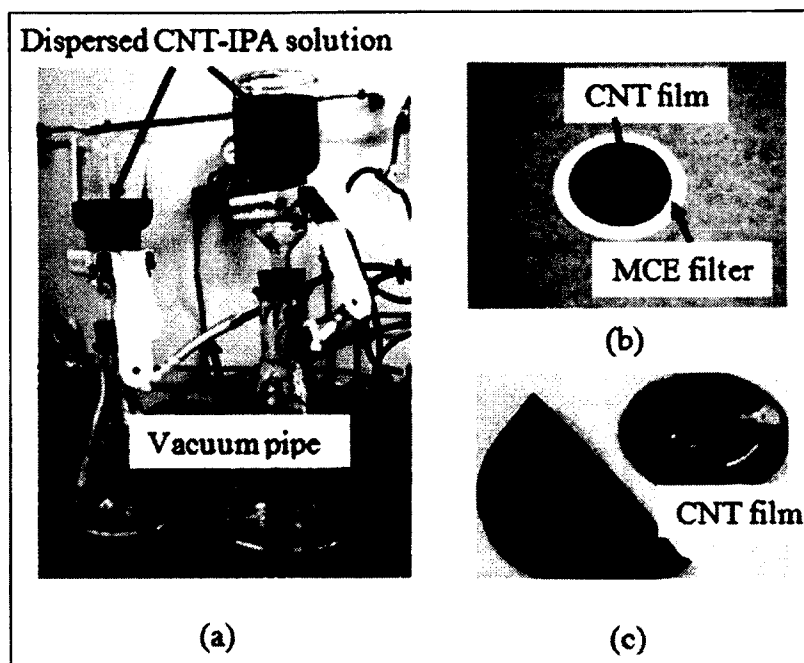


Figure 2-10 Synthesis CNF by vacuum filtration method (a) vacuum filtration system, (b) Synthesized CNF formed on MCE membrane, (c) released CNF size compared to a quarter.

The vacuum filtration system is showed in Figure 2-10 (a); a photo of CNF formed on the MCE membrane is presented in Figure 2-10 (b); a piece of a stand-alone CNF is pictured with a quarter US dollar in Figure 2-10 (c). It is clearly visible that SWCNTs are randomly distributed in the film in Figure 2-11.

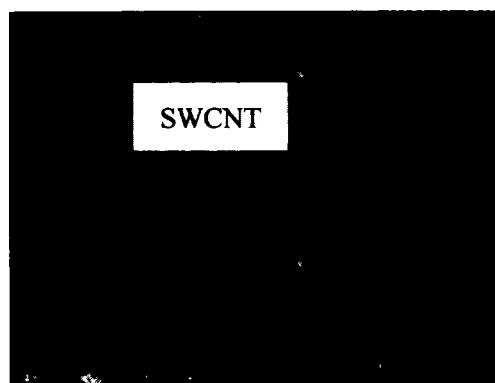


Figure 2-11 SEM image shows SWCNT randomly distributed in CNF.

## 2.4 Carbon Nanotube Film Characteristics

The previous Section 2.2 has shown that single CNT has many unique properties. There is still a lack of research and analysis of the CNF made from CNT. The optical properties and photovoltaic characteristic of CNF are studied in order to better understand the nature of CNF.

### 2.4.1 Optical Properties of Carbon Nanotube Film

It is well known that single CNT exhibits excellent absorption of photons and thermal radiation [73, 74]. The vertically aligned CNTs, showing nearly blackbody effect, have been used to enhance the absorption of light and thermal radiation [75]. This property can potentially be used for optical and thermal energy harvesting. However, synthesis of aligned CNTs is relatively complicated. In contrast, the preparation of carbon nanotube film (CNF) is much simpler. It has been demonstrated that CNF bends upon the illumination of light and has excellent absorption of the light and thermal radiation as well. However, the optical property of a CNF has not been experimentally evaluated [52, 76].

We have designed the experiment to test the absorption or reflectance of the CNF surface using an optical fiber and spectrometer system. When light illuminates perpendicularly on a 30  $\mu\text{m}$  thick CNF surface, the measured reflectance is about 9%, as shown in Figure 2-12 (a). The reflectance from the same CNF at different incident angles is about 3%, as shown in Figure 2-12 (b). Overall, the CNF shows excellent absorption (>91%) of photons.

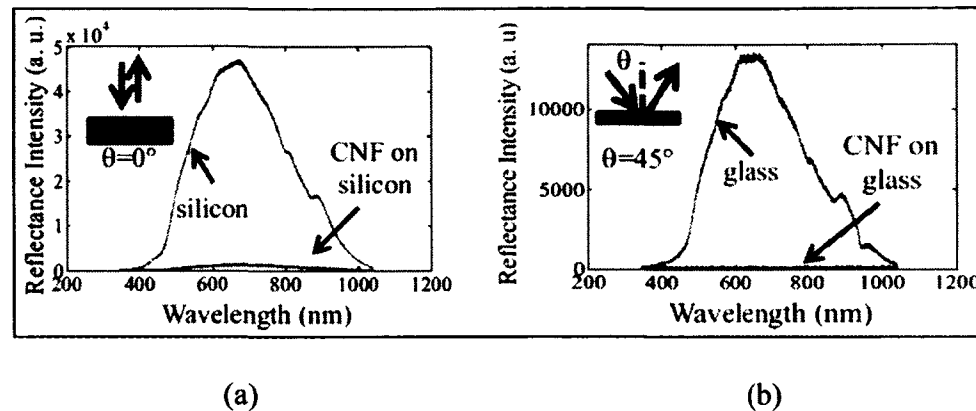


Figure 2-12 (a) Measured reflectance from a silicon wafer and CNF on silicon at an incident angle of  $90^\circ$ ; (b) Measured reflectance from glass and CNF on glass at an incident angle of  $45^\circ$ .

#### 2.4.2 Photovoltaic Properties of Carbon Nanotube Film

A semiconducting CNT was found to have photovoltaic properties. It can convert above-bandgap photons to excitons in CNT which will in turn decay into free electrons and holes such that the individual CNT can act as a nanoscale photodetector [68]. CNF also exhibits the photovoltaic effect but the mechanism is proposed to be thermal or bolometric in nature. The decay of the excitons is mainly non-radiative and it will convert the energy to heat and the change in temperature strongly affects the film resistivity because of the CNT-CNT junctions [53]. The current, voltage and resistance of the CNF, which is about  $10\ \mu\text{m}$  in thickness, have been tested systematically under light and thermal radiation. The CNF sample is released from the MCE membrane and stuck to a glass slide by double sided tape. The dimension of the CNF sample is  $20\ \text{mm}$  (L)  $\times$   $8\ \text{mm}$  (W)  $\times$   $10\ \mu\text{m}$  (T). The light and thermal radiation is provided by an Olympus TL-2 lamp and the intensity of light illumination is  $64\ \text{mW}/\text{cm}^2$  and thermal radiation ( $\Delta T$ ) is  $17.6\ ^\circ\text{C}$ . Figure 2-13 and 2-14 shows the typical open circuit voltage, short circuit current, and resistance generated by the CNF sample. As shown in Figure 2-13 and 2-14 (a), the open



circuit voltage and short circuit current in CNF increases sharply from zero when the light and thermal radiation are turned on. It then fluctuates as far as the light and thermal radiation is maintained on. It only decreases and eventually falls down to zero when the light and thermal radiation is turned off.

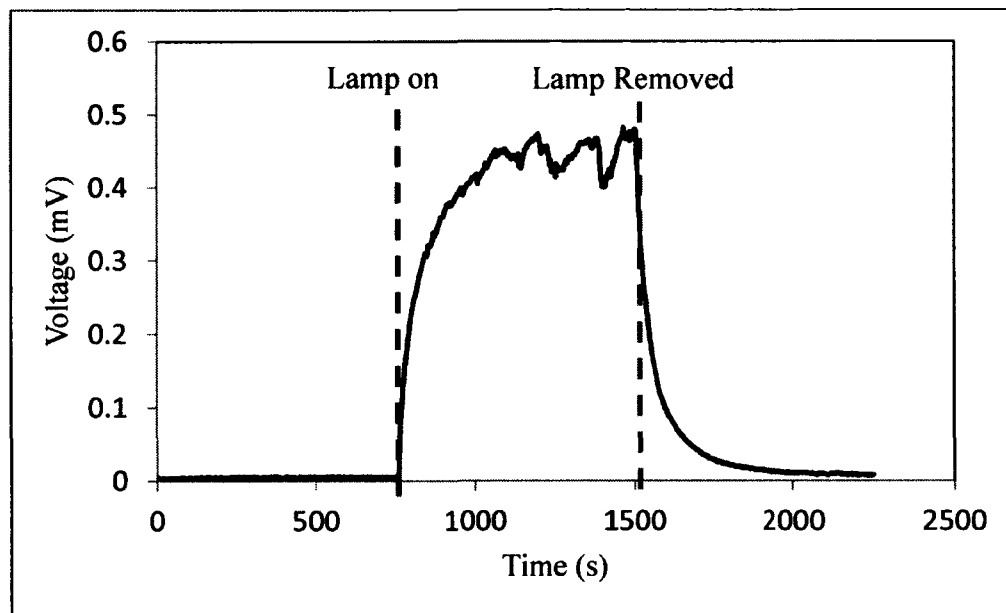


Figure 2-13 Representative measurement of voltage generated by a CNF before, during and after the lamp is on.

In Figure 2-14 (b), the measured resistance of CNF increases and eventually becomes saturated when the light and thermal radiation is on, and the resistance will decrease and finally be back to its original resistance about 0.5 to 1 hour later, which is not included in Figure 2-14 (b).

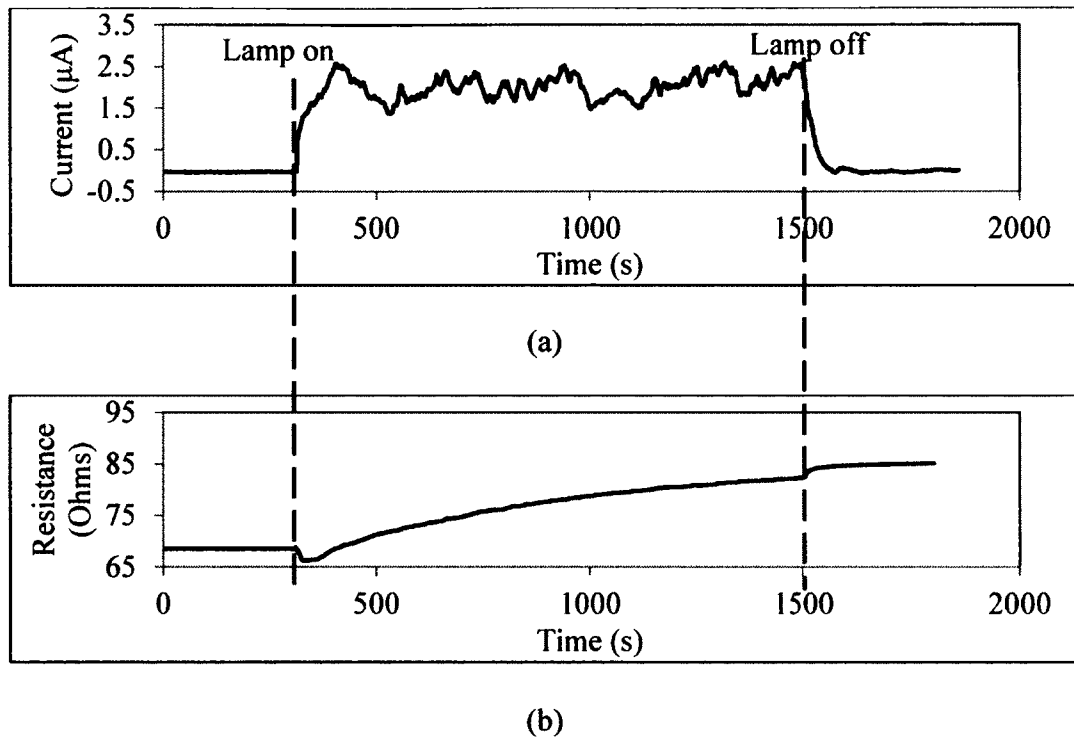


Figure 2-14 Representative measurement of (a) short circuit current and (b) resistance generated by a CNF before, during and after the lamp is on.

### 2.5 Summary

As novel nano materials, the properties and applications of the CNTs and CNF are interesting and attractive. This chapter has reviewed the properties of CNTs including structural, mechanical, electrical, thermal and optical and some applications. A general process for synthesis of CNF using a vacuum filtration method was described. The studies on its optical and photovoltaic properties have been carried out for energy harvesting applications. The large absorption rate of CNF for light shows blackbody effect which could be used to enhance the absorption of light and thermal radiation. The fluctuation of generated open circuit voltage and short circuit current is found upon the CNF exposed to light and thermal radiations. The fundamental studies of the CNF will be very important for exploring its potential applications.

## CHAPTER THREE

### SELF-RECIPROCATION PHENOMENON

#### 3.1 Overview

Given its structural simplicity and ease-of-fabrication, millimeter or micrometer scale cantilevers are probably one of the most frequently used and fundamental mechanical structures for a variety of applications. Specific examples of its applications include biosensing, optical scanning for optical display and biomedical imaging, scanning probe microscopy and spectroscopy, nanolithography, data storage and energy generation [77-82]. There are several ways to actuate the cantilevers. One widely used way is to integrate one electrode with the cantilever and the other underneath the cantilever. The cantilever is displaced by the electrostatic force when a driving voltage is applied between them [56]. Another common way is to integrate a piezoelectric material layer with the cantilever [5]. The cantilever is, therefore, deflected by the electrical-to-mechanical deformation. In other cases, no actuation mechanism is integrated with the cantilever. Instead the cantilever is usually connected to and moved by external actuators [5]. For instance, the micro scale cantilever in the atomic force microscope (AFM) is driven by a piezoelectric actuator so that it can scan across the surface of the sample to be imaged [56]. On the other hand, cantilever structures are developed for energy harvesting applications, such as PZT-based cantilever and other structures are widely used

for vibration energy harvesting [81]. As mentioned in Section 1.3, traditional approaches need mechanical energy, such as external environment vibration to operate. A recently developed actuation mechanism for achieving a self-reciprocating cantilever is presented by H. Li, et. al. [43]. In this case, underneath a cantilever, there is a layer of radioisotope material, serving as a source to emit charges to the cantilever. The cantilever collects the charged particles. As a result, the radioisotope layer has opposite charges left. An electrostatic force will be generated between the cantilever and the radioisotope layer. Due to this electrostatic force, the cantilever is bent. For a proper initial gap between the cantilever and the radioisotope layer, the cantilever tip makes contact with this radioisotope layer. Thus, the accumulated charges are neutralized and the electrostatic force becomes zero. The cantilever is released and starts to oscillate or self-reciprocate [43]. This radioisotope-based cantilever technology has been successfully utilized for this application [83]. Self-reciprocation of a cantilever is particularly attractive and offers a promising platform for continuous energy generation.

Piezoelectric material based energy harvesting needs cyclic bending or deformation of the piezoelectric materials. If we want to harvest solar energy and/or thermal radiation using a piezoelectric material cantilever, it is only really meaningful when a self-cyclic bending of the PZT cantilever can be achieved upon exposure to light and/or thermal radiation. Otherwise, additional energies will be required to turn on and off or modulate the light or thermal radiation in order to periodically bend or deform PZT. It has been reported that carbon nanotube bundles exhibit distinct macroscopic movements when exposed to visible light [76]. The experiments in the previous chapter, Section 2.2, show the CNF has excellent light and thermal absorption ability and the

unique optical and thermal properties of CNF have been used recently for optical actuation [52]. Specifically, it has been mainly exploited and developed for DC displacement. The displacement of a CNF-based cantilever is achieved upon exposure to visible light and will return to its original state when the light is removed. Furthermore, the fluctuation of the open circuit voltage and short circuit current generated by the CNF sample when it is exposed to light and thermal radiation are observed and presented in Section 2.4.2. Obviously, these kinds of features can be exploited to bend the piezoelectric materials, such as lead zirconate titanate (PZT), for energy harvesting. In order to explore and evaluate this potential opportunity, a CNF based multi-layer cantilever structure was designed to examine the self-reciprocating characteristic.

### 3.2 Observation of Self-Reciprocation Phenomenon

#### 3.2.1 Sample Configuration

Copper is chosen as the supporting layer and a variety of CNF-Cu cantilevers are designed. A sketch of a CNF-Cu cantilever chip is given in Figure 3-1 (a) and a photo of the device is shown in Figure 3-1 (b), which consists of a Cu layer and a CNF layer which stacks on the Cu by double-sided tape.

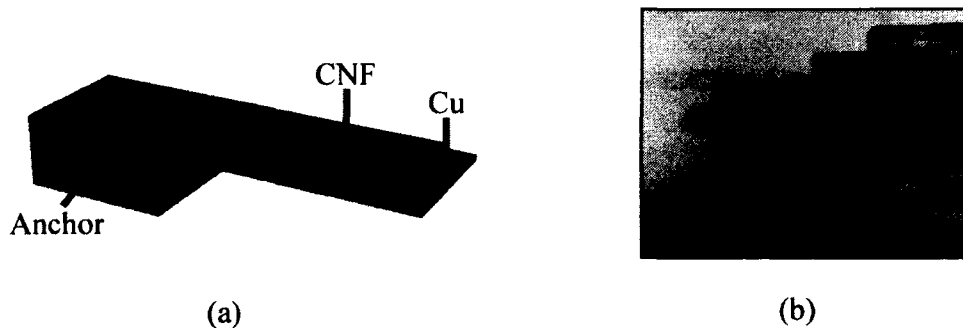


Figure 3-1 (a) sketch of the Cu-CNF cantilever; (b) a photo of CNF-Cu cantilever.

The CNF is synthesized using a vacuum filtration method described in Section 2.3. After the CNF has been synthesized, the CNF-Cu cantilever chip is fabricated by binding the CNF on to the Cu cantilever with double sided tape (cellulose acetate) and anchored on a support. The thicknesses of prepared CNF are 5  $\mu\text{m}$ , 10  $\mu\text{m}$ , 25  $\mu\text{m}$ , and 50  $\mu\text{m}$  for the experiments. Commercially available Cu sheets (Lyon Industries, Inc.) with nominal thickness of 50  $\mu\text{m}$  and 100  $\mu\text{m}$  are used to make Cu cantilevers. Its size measures 20 mm in length, 8 mm in width. The size of CNF measures 18 mm in length, 8 mm in width. Totally, 8 Cu-CNF cantilever samples are prepared for testing. Thickness information details for each sample are listed in the Table 3-1 below.

Table 3-1 Thickness information for each Cu-CNF cantilever

	Sample 1	Sample 2	Sample 3	Sample 4	Sample 5	Sample 6	Sample 7	Sample 8
CNF	50 $\mu\text{m}$	25 $\mu\text{m}$	10 $\mu\text{m}$	5 $\mu\text{m}$	50 $\mu\text{m}$	25 $\mu\text{m}$	10 $\mu\text{m}$	5 $\mu\text{m}$
Cellulose Acetate	76 $\mu\text{m}$	76 $\mu\text{m}$	76 $\mu\text{m}$	76 $\mu\text{m}$	76 $\mu\text{m}$	76 $\mu\text{m}$	76 $\mu\text{m}$	76 $\mu\text{m}$
Cu	50 $\mu\text{m}$	50 $\mu\text{m}$	50 $\mu\text{m}$	50 $\mu\text{m}$	100 $\mu\text{m}$	100 $\mu\text{m}$	100 $\mu\text{m}$	100 $\mu\text{m}$
Ratio (Cu : CNF)	1:1	2:1	5:1	10:1	2:1	4:1	10:1	20:1

In order to confirm that CNF plays an important role in the self-reciprocating characteristic of CNF-based cantilevers, a comparative experiment is planned on a CNF-Cu and a Cu cantilever. For both cantilevers, the width and length of the Cu layer are the same. The only difference is that the Cu cantilever does not have a layer of CNF.

### 3.2.2 Experiment Setup and Testing Conditions

A schematic of the testing setup is shown in Figure 3-2. The laser Doppler vibrometer (Polytec, Inc.) is positioned such that the laser probe is aligned vertically to

the tip of the cantilever, which is not covered with CNF, for the deflection measurement. The light and thermal radiation is provided by an Olympus TL-2 lamp (Olympus, Inc). The light intensity and thermal radiation can be varied either by tuning the lamp or by changing the distance between the lamp and the CNF-Cu cantilever. The light intensity on the CNF surface is measured by an optical power meter (Thorlabs, Inc.), while the thermal radiation (temperature change) is measured by a thermocouple probe (Omega, Inc.).

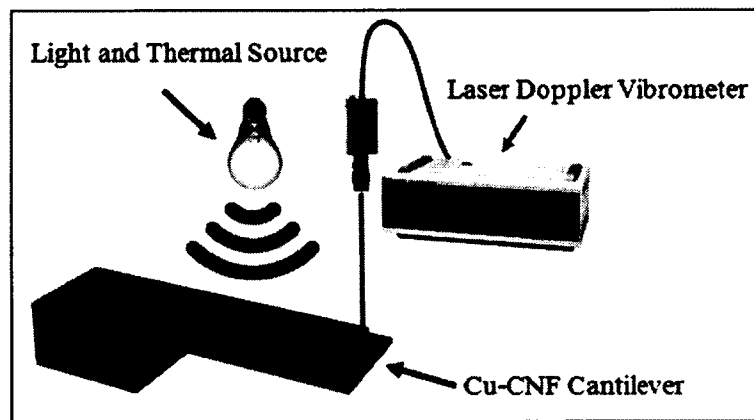


Figure 3-2 Experiment setup for tip displacement measurement using laser Doppler vibrometer.

For the purpose of analysis, the possibility of the self-reciprocation of the cantilever caused by the fluctuation of the light and thermal radiation from the lamp, experiments have been carried out for measuring the output characteristics of the light and thermal radiation. From the example shown in Figure 3-3, both the temperature and optical power will continuously increase for the first 2 minutes when the lamp is turned on. The fluctuation of measured light intensity at a wavelength of 780 nm is about 0.3 mW at 40 mW levels, while the temperature changes are approximately  $\pm 2$  °C at the

33 °C level 5 minutes after the lamp is turned on, that is when the lamp becomes relatively stable. Similar measurements have been performed at different distances from the lamp and give similar results 5 minutes after the lamp is turned on. All the following experiments, therefore, have been performed after 5 minutes has elapsed.

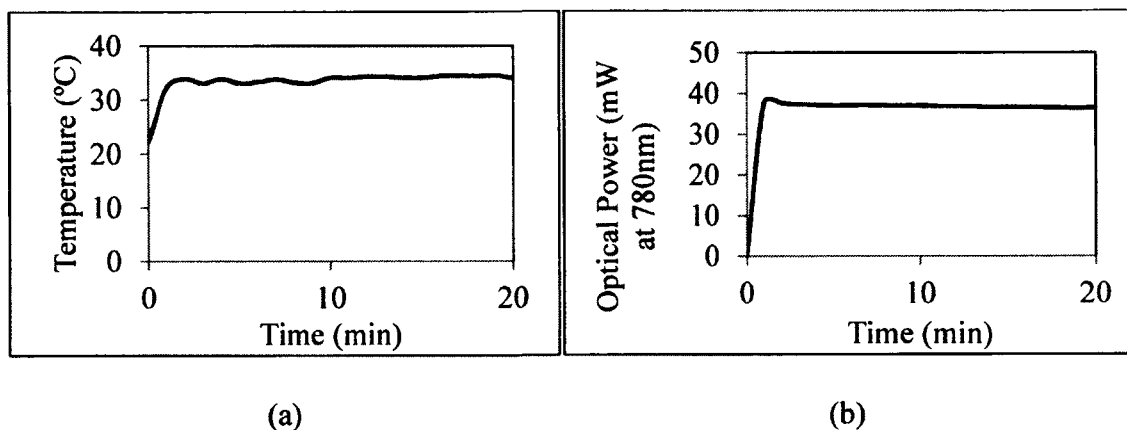


Figure 3-3 A representative measured (a) temperature; (b) light power for TL2 lamp (Olympus, Inc.). All the following experiments performed 5 minutes after the lamp is turned on.

### 3.2.3 Measurements Results

First, a control experiment is carried out between a Cu-CNF cantilever (length= 20 mm, width= 8 mm, thickness= 50  $\mu\text{m}$  and CNF thickness= 5  $\mu\text{m}$ ) and a Cu cantilever (length= 20 mm, width= 8 mm, thickness=50  $\mu\text{m}$ ) in order to confirm that CNF plays an important role in the self-reciprocating characteristic of CNF-based cantilevers. Figure 3-4 gives a measured real-time deflection of the tip of the CNF-Cu cantilever and a Cu cantilever. Measurements clearly show the self-reciprocating characteristic, suggesting a cyclic bending of the CNF-Cu cantilever as long as the light and/or thermal radiation is kept on. In contrast, under the same experimental condition, no self-reciprocating characteristic has been observed for a Cu cantilever. Systematic experiments have been



performed on CNF-Cu cantilever and Cu cantilevers with a variety of different dimensions. It has been confirmed that self-reciprocation of CNF-Cu cantilevers routinely occurs as far as the light and/or thermal radiation is present.

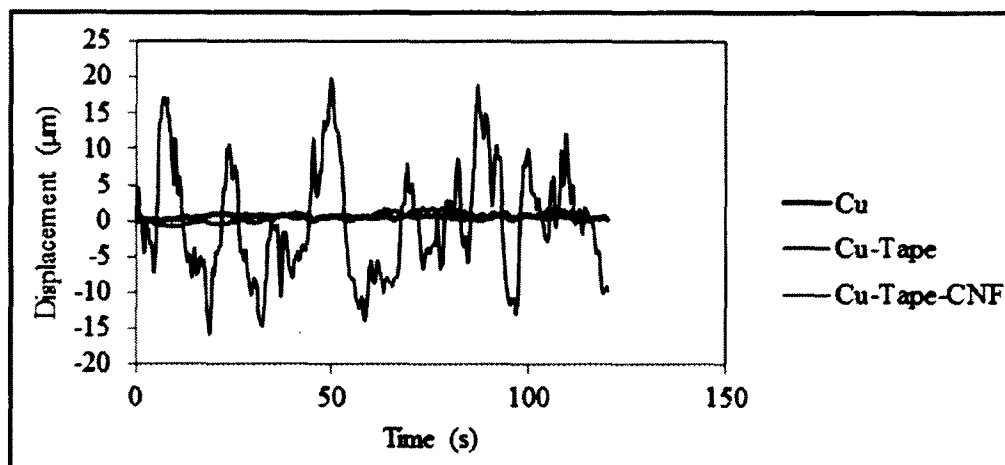


Figure 3-4 Representative measurements of the displacement of the tip of the Cu cantilever, Cu plus double-sided tape cantilever and CNF-Cu cantilever. The intensity of light illumination is  $64 \text{ mW/cm}^2$  and thermal radiation ( $\Delta T$ ) is  $17.6 \text{ }^\circ\text{C}$ .

To examine the CNF effect on the self-reciprocation, the following experiments have been designed and undertaken. Firstly, the effect of different thickness of CNF on the CNF-Cu cantilever (the thickness of Cu is fixed as  $50 \text{ }\mu\text{m}$ ) under the same light and thermal radiation (light intensity  $64 \text{ mW/cm}^2$ , temperature change  $\Delta T = 17.6 \text{ }^\circ\text{C}$ ) has been examined. It shows that the CNF-Cu cantilever with  $5 \text{ }\mu\text{m}$  and  $10 \text{ }\mu\text{m}$  CNF exhibits the largest amplitude of self-reciprocation among the cantilevers with CNF thicknesses of  $5 \text{ }\mu\text{m}$ ,  $10 \text{ }\mu\text{m}$ ,  $25 \text{ }\mu\text{m}$  and  $50 \text{ }\mu\text{m}$ , as shown in Figure 3-5. This observation suggests that there is an optimum thickness of CNF for achieving the largest amplitude. For instance, based on this set of experiments, the amplitude of the vibration of the CNF-Cu cantilever with CNF of  $5 \text{ }\mu\text{m}$  and  $10 \text{ }\mu\text{m}$  is about 2 to 4 times larger than those of the cantilevers

with a CNF of 25  $\mu\text{m}$  and 50  $\mu\text{m}$ , which indicates that if we want to use the CNF-based cantilever technology for light and thermal energy harvesting, the thickness of CNF and the cantilever should be carefully designed and optimized to achieve the best energy conversion efficiency.

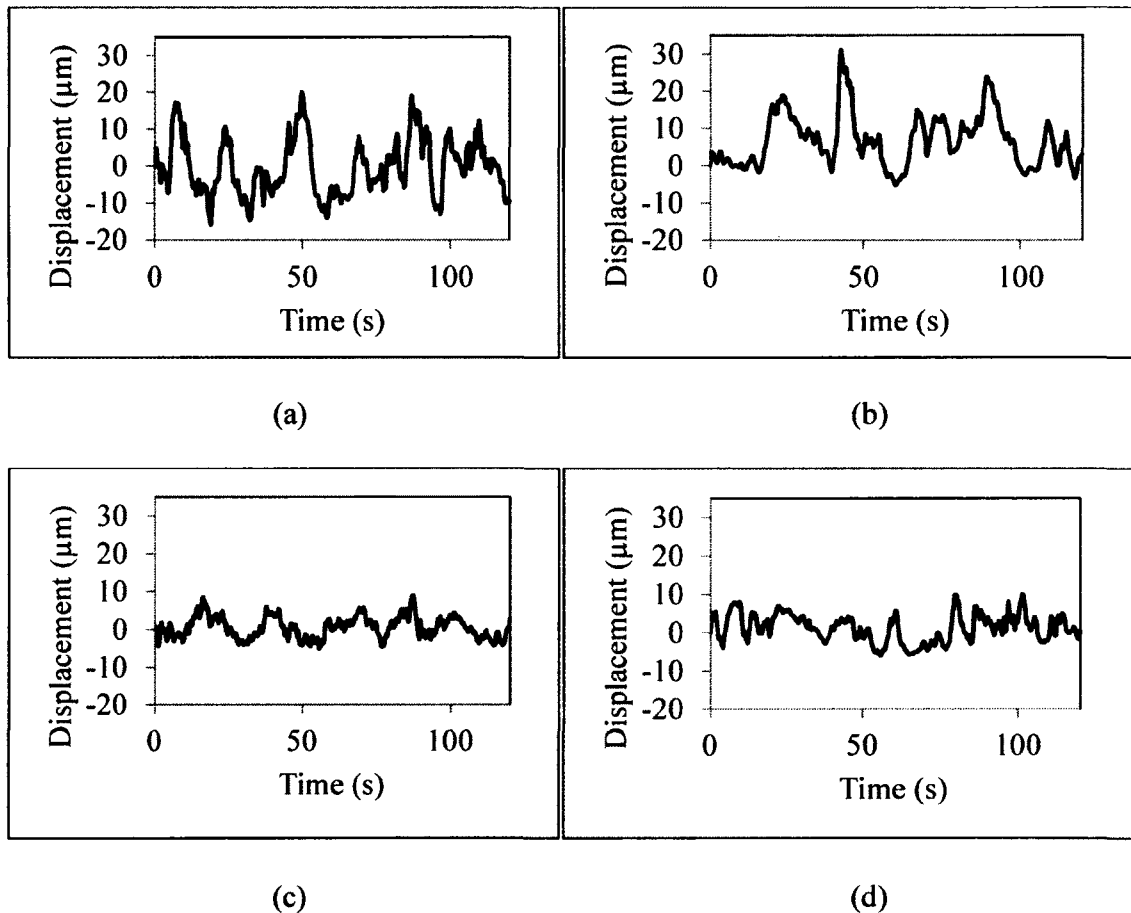


Figure 3-5 Measured self-reciprocating characteristics of CNF-Cu cantilevers with variable CNF thickness and fixed thickness (50  $\mu\text{m}$ ) Cu cantilever: (a) CNF thickness 5  $\mu\text{m}$ ; (b) CNF thickness 10  $\mu\text{m}$ ; (c) CNF thickness 25  $\mu\text{m}$ ; (d) CNF thickness 50  $\mu\text{m}$ .

Secondly, the effect of changes in light intensity and thermal radiation on the same CNF-Cu cantilever has been experimentally examined. As an example, the cantilever with 10  $\mu\text{m}$  thick CNF has been selected and experiments have been performed

under 4 different conditions. The experiments demonstrated that the amplitude of the reciprocation of CNF-Cu cantilevers increases when the light intensity and thermal radiation increases, as shown in Figure 3-6. For instance, the peak amplitude of the tip deflection of the cantilever increases from about 20  $\mu\text{m}$  to about 65  $\mu\text{m}$  when the light intensity is changed from 14  $\text{mW}/\text{cm}^2$  to 64  $\text{mW}/\text{cm}^2$  and the temperature changed from 3.9  $^{\circ}\text{C}$  to 17.6  $^{\circ}\text{C}$ . When more light and thermal radiation is available, the CNF can absorb more, thereby causing a larger deflection of the cantilever.

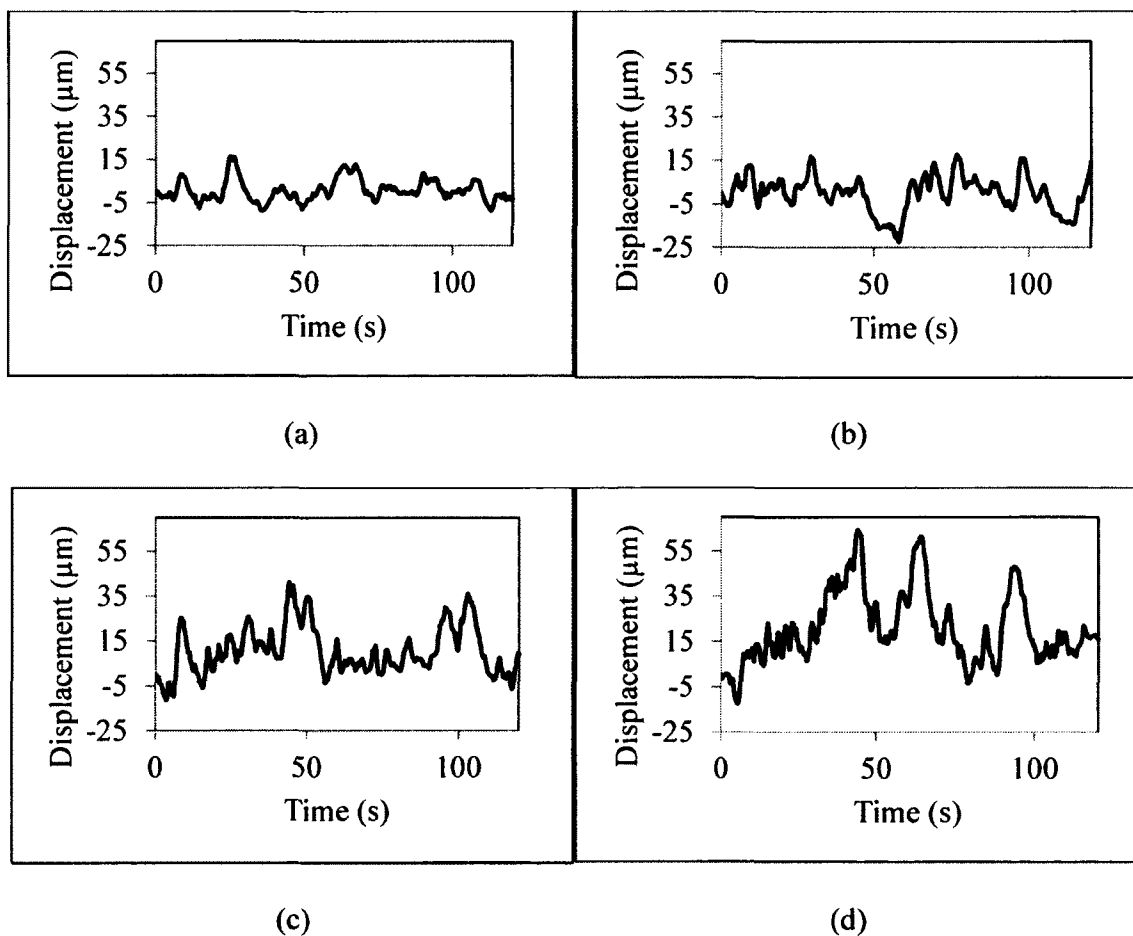


Figure 3-6 With the same CNF-Cu cantilever (Cu: 50  $\mu\text{m}$  thick, CNF: 10  $\mu\text{m}$  thick) at different light intensity and thermal radiation: (a) 14  $\text{mW}/\text{cm}^2$ , 3.9  $^{\circ}\text{C}$ , (b) 34  $\text{mW}/\text{cm}^2$ , 7.8  $^{\circ}\text{C}$ , (c) 40  $\text{mW}/\text{cm}^2$ , 16.4  $^{\circ}\text{C}$ , (d) 64  $\text{mW}/\text{cm}^2$ , 17.6  $^{\circ}\text{C}$ .

Thirdly, the effect of different thickness of the Cu layer (the thickness of Cu layer is changed from 50  $\mu\text{m}$  to 100  $\mu\text{m}$ ) on the CNF-Cu cantilever under the same light and thermal radiation, as that in Figure 3-5, has been examined. The measurement is shown in Figure 3-7. Compared to the measured results in Figure 3-5, the respective deflection amplitude for the cantilevers with the same thicknesses (5  $\mu\text{m}$ , 10  $\mu\text{m}$ , 25  $\mu\text{m}$ , 50  $\mu\text{m}$ ) of CNF is about 2-10 times lower as expected. The reason is the thickness of the Cu layer is doubled and thus, the CNF-Cu cantilever becomes less compliant mechanically.

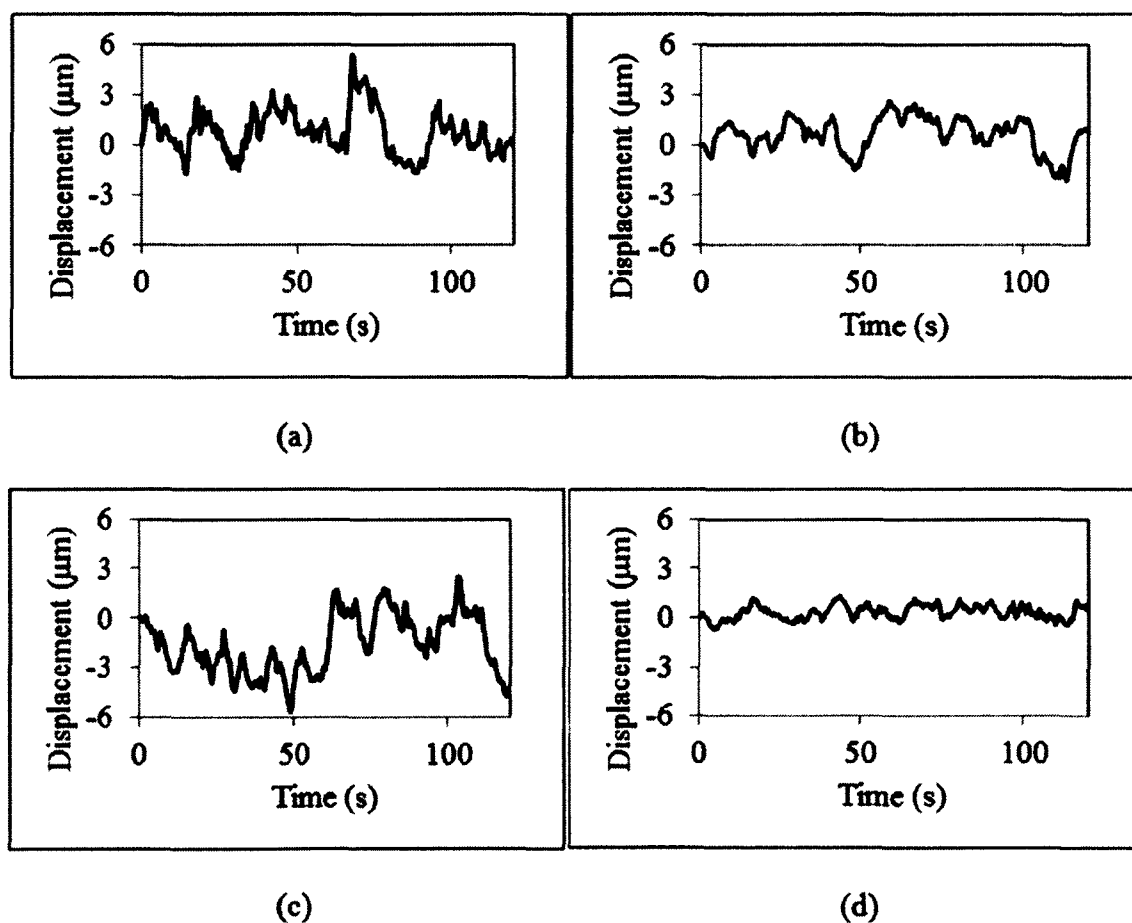


Figure 3-7 Measured displacement with the same 100  $\mu\text{m}$ -thick Cu but different CNF thicknesses including (a) 5  $\mu\text{m}$ , (b) 10  $\mu\text{m}$ , (c) 25  $\mu\text{m}$  and (d) 50  $\mu\text{m}$ . The intensity of light illumination is 64  $\text{mW}/\text{cm}^2$  and thermal radiation ( $\Delta T$ ) is 17.6  $^{\circ}\text{C}$ .

It confirms that the thickness of the Cu layer is another parameter for the optimum design. In addition, after a series of systematic experiments, it has been found that the pattern of self-reciprocation of the same cantilever is not identical but always varying when the cantilever is operated at a different time even though the displacement amplitude range is essentially in the same range.

### 3.3 Fourier Analysis

A signal can be expressed in the time domain or in the frequency domain. Previous data and analysis in this chapter showed the displacement characteristics along the time which were presented in the time domain. These time domain signals can be constructed by adding together sine waves of appropriate frequency, amplitude, and phase. The frequency domain describes a domain for analysis of signals with respect to frequency. Fourier analysis is a technique that is used to find out which sine waves a given signal is composed of. The process of Fourier analysis is to deconstruct the signal into its component sine waves. For this purpose, we need to first convert the signal in the time domain to the frequency domain using Fourier transformation.

#### 3.3.1 Discrete Fourier Transform and Fast Fourier Transform

In mathematics, the discrete Fourier transform (DFT) is a specific kind of discrete transform, used in Fourier analysis. The input function requirement for DFT is that the signal must be finite and discrete. Such inputs are often generated by sampling a continuous function. Since the input to the DFT is a finite sequence of numbers making the DFT ideal for processing information stored in computers and it has been widely used in signal processing and its related field.

By definition, the sequence of  $N$  complex or real numbers  $x_0, \dots, x_{N-1}$  is transformed into the sequence of  $N$  complex numbers  $X_0, \dots, X_{N-1}$  using DFT according to the formula below:

$$X_k = \sum_{n=0}^{N-1} x_n e^{-\frac{2\pi i}{N}kn} \quad k = 0, \dots, N-1, \quad (3-1)$$

where  $i$  stands for the imaginary unit and  $e^{-\frac{2\pi i}{N}}$  stands for primitive  $N$ 'th root of unity.

The standard numerical algorithm used for the DFT is called the Fast Fourier Transform (FFT) which largely increases the transformation efficiency and makes it a practical and important transformation on computers. The most commonly used FFT is called the Cooley-Tukey algorithm which is developed by J. W. Cooley and J. W. Tukey and they published a paper in 1965 [84]. Briefly, it re-expresses the DFT of an arbitrary composite size  $N = N_1 \times N_2$  into a lot of smaller DFTs of size  $N_1$  and  $N_2$  and largely reduce the calculations to the order of  $N \times \log_2(N)$  [85].

### 3.3.2 Results and Analysis

The self-reciprocating frequencies of the cantilevers have been analyzed by performing Fourier transform on the measured displacement spectra for all fabricated cantilevers. The results and analysis will help find out the frequency characteristics of the self-reciprocation of the CNF-Cu device. In order to conducting Fourier analysis in a computer, the continuous signal of displacement needs to be sampled and converted into a discrete time signal. The general procedure of signal processing in order to conduct Fourier analysis is presented in Figure 3-8.

The tip displacement information is measured by laser Doppler vibrometer (Polytec, Inc.) and recorded in a desktop computer. Displacement information is essentially an analog or continuous signal in the time domain. In order to recognize,

record and analyze by computer, the continuous signal must be digitized by sampling the continuous signal. This process is called analog-to-digital conversion (A/D conversion). The sampling process is automatically done by the laser Doppler vibrometer system and the sampling rate is set to be 256 Hz in the software. The sampling rate 256 Hz means the system can record 256 points in one second and therefore, 32,768 points will be recorded in 128 seconds.

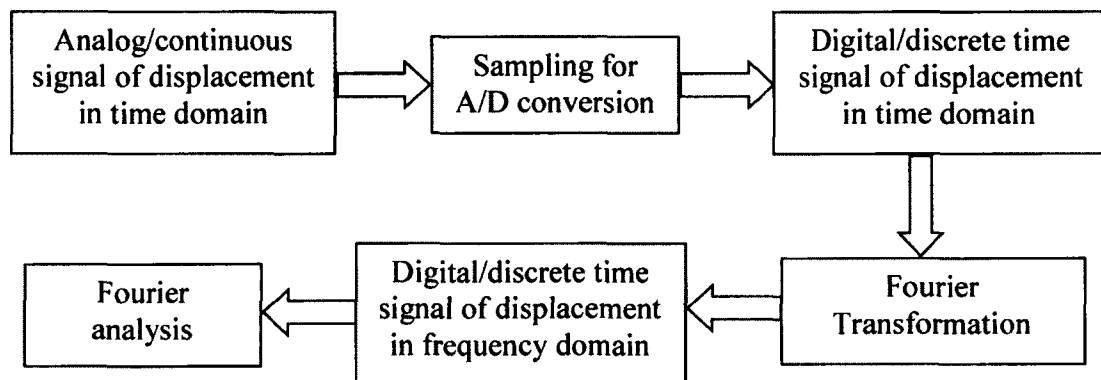
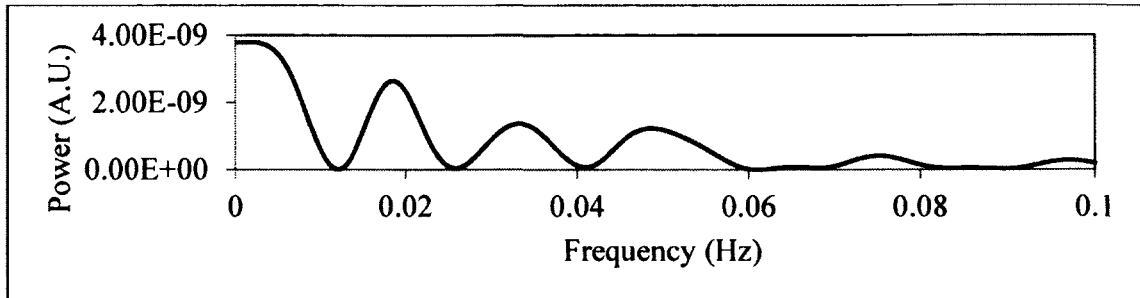


Figure 3-8 Procedure of signal processing for conducting Fourier analysis.

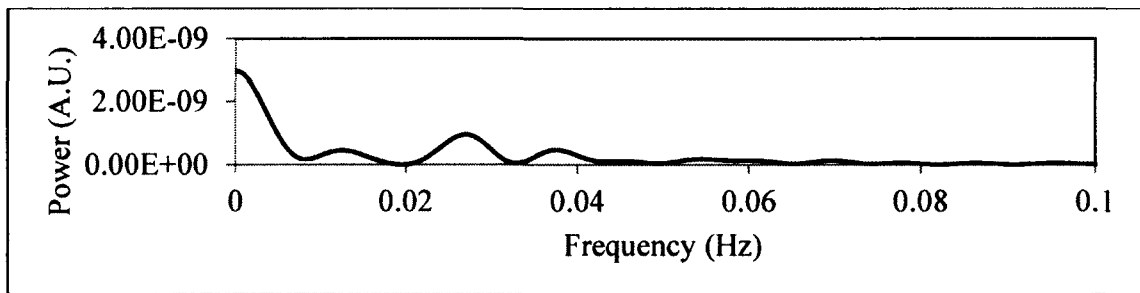
Figure 3-9 shows the representative frequencies for the CNF-Cu cantilever with 50  $\mu\text{m}$ -thick Cu and 4 different thickness of CNF under light and thermal radiation. Systematic results reveal that for all cantilevers, they all have about 3 main frequencies which are distributed below 0.1 Hz.

Table 3-2 Simulation results of natural resonating frequencies from ANSYS

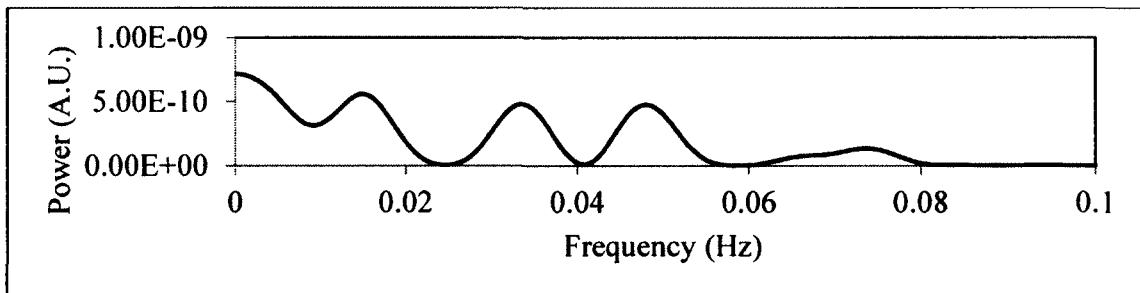
Nature Frequency Order	Frequency (Hz)			
	Sample 1	Sample 2	Sample 3	Sample 4
1 <sup>st</sup> Bending	227.1	163.97	119.75	102.58
2 <sup>nd</sup> Torsion	1165.6	849.84	620.16	528.02
3 <sup>rd</sup> Bending	1392.4	1010.4	739.8	633.91



(a)



(b)



(c)

Figure 3-9 Representative self-reciprocating frequencies of the CNF-Cu cantilevers (Cu: 50  $\mu\text{m}$  thick, CNF: from 10 to 50  $\mu\text{m}$  thick) by Fourier transform of measured displacement responses under light and thermal radiations: (a) CNF 10  $\mu\text{m}$ ; (b) CNF 25  $\mu\text{m}$ ; (c) CNF 50  $\mu\text{m}$ .

All the cantilevers are vibrating at low frequencies, typically in the range of 0.01 to 0.08 Hz. In contrast, typical natural mechanical resonating frequencies of these cantilevers, which have been calculated using finite element analysis in ANSYS, are in the range of 170 Hz to 220 Hz. The simulation results of the first to third order of natural



resonating frequencies for sample 1 to sample 7 are listed in the Table 3-2. The value at 0 Hz means static shift (DC shift) of the whole displacement waveform in the time domain. It may come from the systematic error of the vibrometer system and since it is not important to the Fourier analysis, it is considered to be negligible. In order to achieve the largest deflection amplitude, the natural mechanical resonating frequency of the cantilevers should be tailored and scaled to match the self-reciprocating frequencies of the cantilevers.

### 3.4 Proposed Mechanism of Self-Reciprocation

Some analysis and experiments have been undertaken to understand and explain the physical mechanism for the light and thermal radiation-induced self-reciprocation of the CNF-Cu cantilever. The bending of the CNF-Cu cantilever under light and thermal radiation is relatively easy to understand. Similar to the argument in the literature [76], the photon and thermal pressure effect can be excluded since its cyclic bending is bi-directional movement and not always the same as the radiation direction of the light and thermal source. Upon absorption of photons in the visible (light), near infrared and infrared (thermal radiation) spectrum, the CNF experiences the following changes: each single CNT in the CNF absorbs photon energy tremendously and converts it into thermal energy [52, 76, 86]. The rise in temperature of CNTs coupled with their high thermal conductance increases the temperature of the CNF rapidly. This results in the thermal expansion of the CNF and Cu layer. Since the CNF layer and Cu layer have different thermal expansion coefficient, bending of the CNF-Cu cantilever occurs. In addition, when light is incident on the CNTs, non-uniform charge distribution exists in CNF due to

the electron-hole pair (exciton) generation in the CNTs. As a result, an electrostatic field is produced, which also causes the CNF to expand, bend and repel [52, 86].

The physical mechanism behind the self-reciprocation has not been reported before and is more complicated. Studies of the photovoltaic properties showed the electrostatic interaction among randomly connected CNTs in CNF have been carried out and the results were shown in Section 2.4.2. The CNF sample, which is 25  $\mu\text{m}$  in thickness with both ends connected with electrodes, is fixed on a glass substrate. Hence, the possible current or resistance changes due to the bending or deformation of the CNF are eliminated during the measurement. As we can observe from the results in Figure 2-14 (a), all these features are similar to the mechanical behavior of the CNF-Cu cantilever, suggesting the self-reciprocating characteristic of the CNF-Cu cantilever shares the same origin as that of the light and thermal radiation-induced electricity inside CNF. Fourier transform of the current shows that its major fluctuation frequencies are typically in the range of 0.002-0.02 Hz, which are somewhat lower than those of the self-reciprocating frequencies of the CNF-Cu cantilever but in a similar low frequency range. The resistance characteristic of a CNF sample under light and thermal radiation is shown in Figure 2-14 (b) ( $R_{\text{CNF}}$ ). It increases and eventually becomes saturated when the light and thermal radiation is on, and the resistance will decrease and eventually return to its original resistance about half to one hour later, which is not included in Figure 2-14 (b). This observation of resistance change of CNF is consistent with previously reported results [53, 87]. Based on these measurements, a simple calculation shows that the Joule heating ( $I_{\text{CNF}}^2 \times R_{\text{CNF}}$ ) generated in CNF layer also exhibits fluctuation, resulting in the temperature fluctuation in the layer-structured CNF-Cu cantilever, which renders its self-

reciprocation. Therefore, we believe that the self-reciprocating characteristic of the CNF-Cu cantilever is mainly attributed to the electrostatic interaction (e.g., electricity) among CNTs inside the CNF. This is due to the fluctuation characteristic of the current/voltage inside CNF as a result of a photovoltaic and thermoelectric effect of CNTs [52, 76, 89]. It should be noted that when a CNF-cantilever is exposed to light and thermal radiation and starts to bend, the current and resistance changes of the CNF might be varied due to the repeated deformation of the CNF. In addition, the fluctuation of the temperature and light intensity of the lamp, even though quite small, as shown in Figure 3-3 after being stable, may also contribute somewhat to the heat fluctuation in the CNF-Cu cantilever. It should be noted that it is very challenging if not impossible to find a light and thermal source which has no temperature or intensity fluctuation. In terms of practical energy harvesting application, the fluctuation of light intensity and thermal radiation actually is a benefiting factor for the CNF-based cantilever devices. Finally, since the CNF-Cu cantilever is operated in an open air environment, the self-reciprocation of a CNF-based cantilever is also related to high electrical conduction and rapid thermal dissipation by the CNF to the environment, and continuous absorption of photons by the CNF from the illuminating light and thermal radiation source [86]. It is anticipated that the self-reciprocating characteristic might be dramatically degraded if the cantilever is operated in a vacuum environment since the heat dissipation from the cantilever is significantly reduced.

### 3.5 Summary

Following the hint of the oscillation of the current generated by CNF under thermal and light radiations in Section 2.4.2, self-reciprocating characteristic of the

carbon nanotube film (CNF)-Cu cantilevers upon exposure to light and thermal radiation is observed. Detailed experimental studies of this phenomenon are conducted. The low-frequency self-reciprocation, being sensitive to the thicknesses of CNF and Cu and the intensity of the light and thermal radiation, is mainly attributed to the electrostatic interaction among randomly connected carbon nanotubes (CNTs) in CNF. This is due to the fact that electrical currents in CNF induced by light and thermal radiation also exhibit an oscillating characteristic, similar to the self-reciprocating characteristic of the CNF-Cu cantilevers. The mechanism for this observed phenomenon is also discussed by relating the optical, thermal, electrical, elastic and mechanical properties of the CNF.

## CHAPTER FOUR

### DESIGN, FABRICATION, AND DEMONSTRATION OF MACRO- SCALE PROTOTYPES

#### 4.1 Introduction

Cantilever structures that are developed for energy harvesting applications, such as PZT-based cantilever and other structures, are widely used for vibration energy harvesting [5]. As previously stated, piezoelectric material based energy harvesting needs cyclic bending or deformation of the piezoelectric materials. If we want to harvest the solar energy or/and thermal radiation using the piezoelectric material cantilever, it is only meaningful when a self-cyclic bending of the PZT cantilever can be achieved upon exposure to light or/and thermal radiation. Otherwise, additional energies, such as ambient vibration or changing light or thermal radiation are needed in order to bend or deform the PZT periodically. The self-reciprocation phenomenon that has been observed, now has an opportunity to develop a new type of energy harvesting cantilever structure without any intentional external modulation of the light or thermal radiation or ambient mechanical energy. Based on this, a macro scale (mm scale) prototype device is designed, fabricated, and demonstrated.

#### 4.2 Prototype Design and Fabrication

The sketch of the prototype CNF-PZT cantilever energy harvesting device is shown in Figure 4-1(a). It consists of a CNF layer and a piezoelectric material (PZT) layer sandwiched between two nickel electrode layers. The CNF layer attached to the top serves as an efficient absorber of photons and thermal radiation and consequently introduces the self-reciprocation of the cantilever.

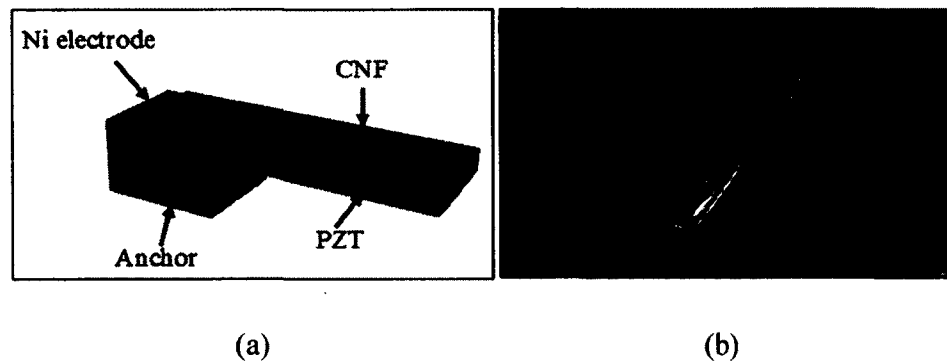


Figure 4-1 (a) Sketch of the prototype CNF-PZT cantilever; (b) a photo of the prototype CNF-PZT cantilever comparing with a dime dollar.

The CNF is synthesized using the vacuum filtration method which has been described in Section 2.3. Briefly, the SWCNTs (Carbon Solutions, Inc.) are immersed in Isopropyl alcohol (IPA) to obtain final concentrations in the range of 0.10 mg/ml - 0.40 mg/ml. The mixture is then ultrasonicated overnight to ensure uniform dispersion of the SWCNTs. The dispersed SWCNTs in the IPA are vacuum filtered through a Whatman ME-24 mixed cellulose ester (MCE) membrane. The obtained CNF and filter membrane is then rinsed with IPA and deionized water several times, and then it is dried for approximately 2 to 3 hours. Afterwards, the MCE filter is dissolved in several acetone baths and rinsed with IPA. Typical thicknesses of the resulting composite nanomaterial

thin-film are in the range of 10-100  $\mu\text{m}$ . The rectangular PZT cantilever is diced from a 6 inch PZT wafer (CTS Inc.). It consists of piezoelectric material PZT-5A with nickel electrodes coated on both sides. The thickness of PZT and Ni is 300  $\mu\text{m}$  and 2  $\mu\text{m}$  respectively. The synthesized CNF is attached to the top of the PZT cantilever by a layer of double-sided tape (Scotch tape) which is 76  $\mu\text{m}$  in thickness and made of cellulose acetate. The cantilever has the length of 20mm and width of 8mm. Two electrical conductive wires are attached to top and bottom electrodes individually. The whole cantilever structure is supported on a plastic anchor. A photo of the prototype device is shown in Figure 4-1 (b).

### 4.3 Experiments Setup and Measurements

Firstly, in order to confirm the self-reciprocation phenomenon on the prototype device, a similar experiment is conducted for detecting the displacement of the tip. In the meantime, an oscilloscope is connected to the top and bottom electrodes to record the open circuit voltage (OCV) generated. Then, the device is placed under a sun simulator which provides both light and thermal radiations to examine if it can operate as an energy harvester.

#### 4.3.1 Displacement versus Open Circuit Voltage

The setup for measuring the tip displacement and open circuit voltage (OCV) of the CNF-PZT cantilever is given in Figure 4-2. A piece of aluminum foil is attached to the tip of the cantilever for reflection. A laser Doppler vibrometer (Polytec, Inc) is positioned so that the laser probe is perpendicular to the cantilever and aligned to its tip region. For measuring the OCV, an oscilloscope is used to monitor the dynamic change of the OCVs in real time when the CNF-PZT cantilever is harvesting energies. The

Olympus TL-2 lamp (Olympus, Inc) is put in proximity to the cantilever and provides the light and thermal radiations. The intensity of the lamp is tunable, while the amount of thermal radiation from the lamp is achieved by changing the gap between the cantilever and the lamp. The light intensity is measured with a digital optical power meter (Thorlabs, Inc) and the thermal radiation is quantified by measuring the temperature changes using a thermocouple probe (Omega, Inc). In all these experiments, the light intensity is determined by the measured optical power at a wavelength of 635 nm.

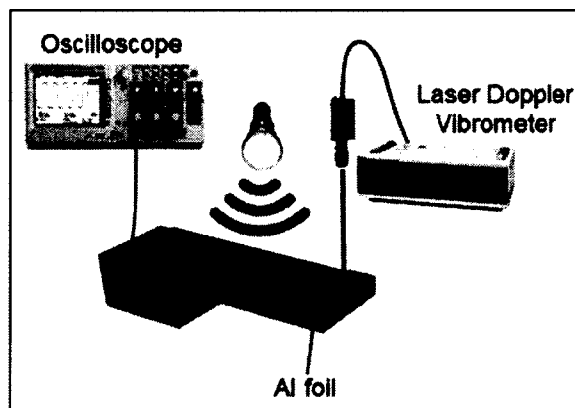


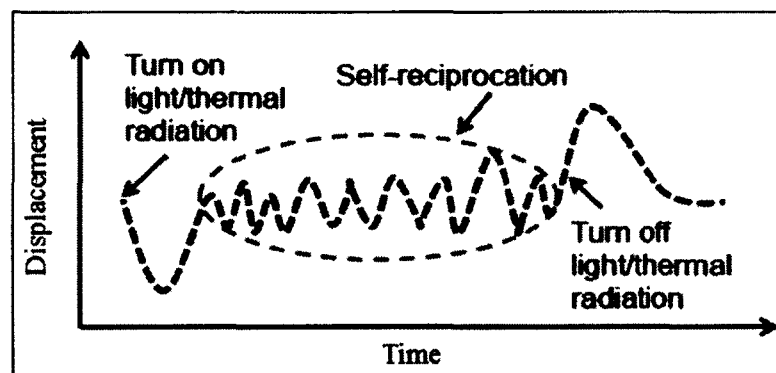
Figure 4-2 Setup for measuring the real-time tip displacement and open circuit voltage of the CNF-PZT cantilever using a laser Doppler vibrometer and an oscilloscope when the cantilever is exposed to light and thermal radiation.

After repeated experiments, the results show that the cantilever has a relatively big displacement immediately after exposure to a light or a thermal source or immediately after the light or the thermal source is removed. Self-reciprocation of a CNF-PZT cantilever occurs only between the light or thermal source on and off, specifically sometime later after its exposure to light and thermal radiation. The illustrative displacement is schematically shown in Figure 4-3 (a). Figure 4-3 (b) shows

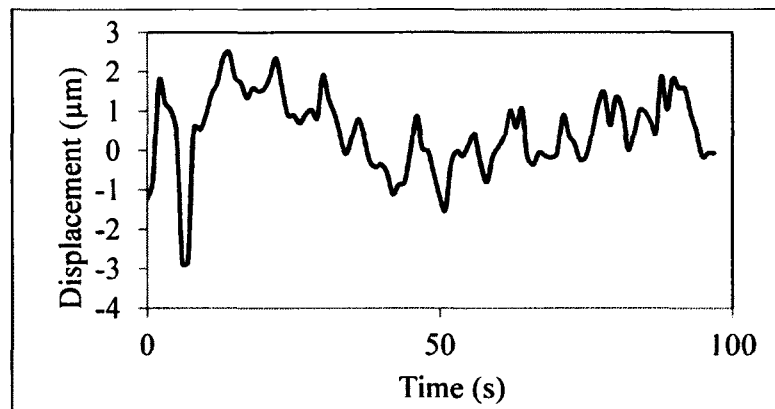


an example of the displacement after a period of time when a CNF-PZT cantilever is exposed to light and thermal radiation.

In the meantime, an oscilloscope recorded the OCV generated by the cantilever. Representative measured OCVs are shown in Figure 4-4 (a). The device has a big OCV after the lamp is turned on. Thereafter, OCV drops and then fluctuates due to the cyclic bending of the cantilever.



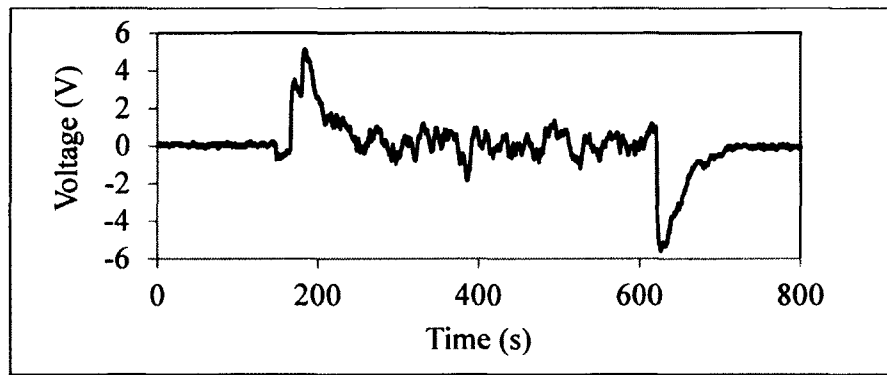
(a)



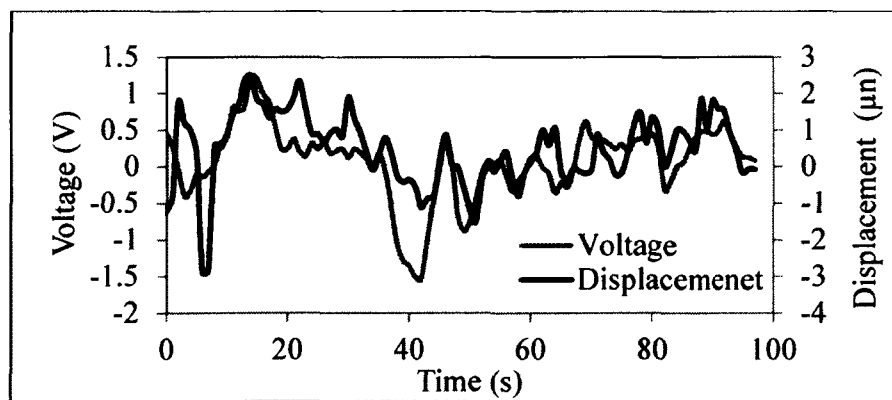
(b)

Figure 4-3 (a) Sketch of real-time displacement of a CNF-PZT cantilever upon exposure to light and thermal radiation (not to scale); (b) measured displacement in the self-reciprocation region.

The device has a big OCV after the lamp is turned off and eventually OCV becomes zero. Figure 4-4(b) shows the fluctuation region of OCV and compared to the corresponding displacement oscillation which indicates the continuous power generations as far as light and/or thermal radiation is/are present. Notice that the OCV and displacement are not exactly overlapped or synchronized due to the discharging characteristic of the capacitive PZT.



(a)



(b)

Figure 4-4 (a) measured OCVs with light intensity of  $0.042 \text{ W/cm}^2$  and thermal radiation (temperature change) of  $13.5 \text{ }^\circ\text{C}$ . The light intensity is measured at wavelength of  $780 \text{ nm}$ ; (b) real-time displacement and corresponding OCV of self-reciprocation region.

#### 4.3.2 Solar Energy Harvesting and Power Output

After confirming the self-reciprocation phenomenon and generation of OCV of the CNF-PZT cantilever by exposing to an Olympus TL-2 incandescent lamp which generates light and thermal energy, the CNF-PZT cantilever is tested for harvesting solar energy. A sun simulator (Sun System SS-2MH 400) is used to provide the radiation energy. Optical power is measured from 400 nm to 1100 nm. A typical spectrum of the sun simulator is plotted in Figure 4-5. As we can see, most of the energy is concentrated at the short wavelength from the sun simulator. The temperature difference is around 13 °C to 16 °C from the light source and room temperature. Representative measured OCVs generated from the energy of the sun simulator are shown in Figure 4-6. It shows a similar trend to the previous testing with the Olympus TL-2 incandescent lamp. The clear voltage oscillation and two peaks are consistent.

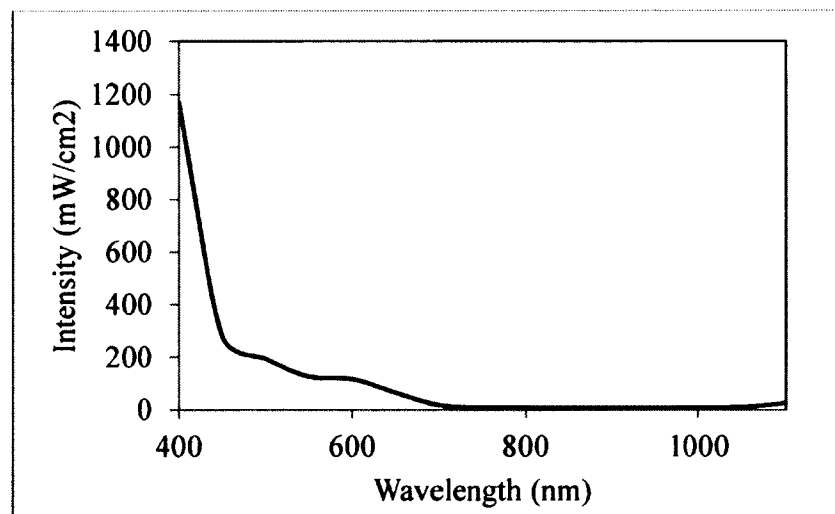


Figure 4-5 Optical spectrum of the Sun System SS-2MH 400 Sun Simulator (measured wavelength from 400 nm to 1100 nm).

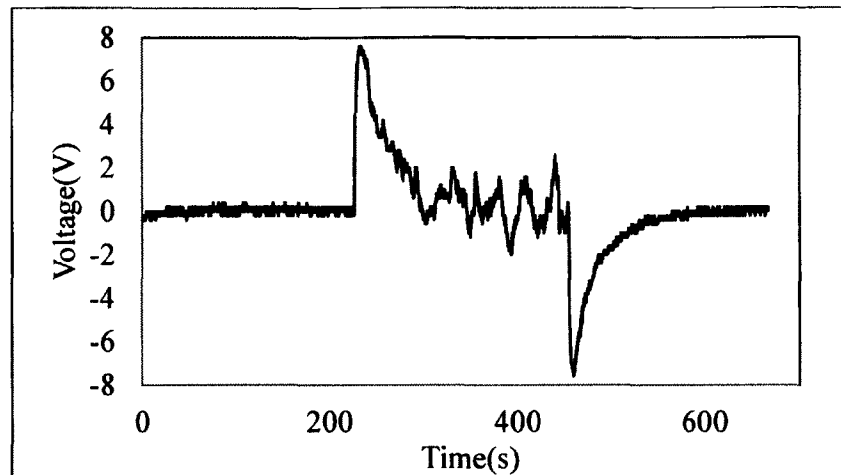


Figure 4-6 Representative OCVs from solar energy harvesting using a sun simulator.

In terms of energy harvesting, how much power an energy harvesting device can generate is a more practical performance indicator. In order to find the maximum power output of the macro scale prototype CNF-PZT cantilever, a simple circuit is designed and is shown in Figure 4-7. It was determined that the amount of energy generated by piezoelectric materials was not sufficient to power most electronic devices [90]. Thus, for making energy harvesting technology into practical use, an energy storage component is needed for driving electronic devices. A super capacitor or battery is commonly used as the storage media for energy harvesting devices. For both cases, a DC potential is needed for charging. Therefore, it is more meaningful to know the DC power output.

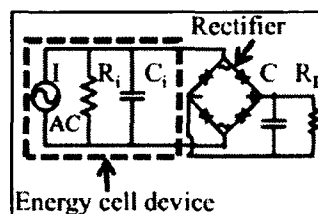


Figure 4-7 Equivalent circuit of an energy harvester and the circuit with a load resistor  $R_L$  for the power measurement.

Due to the AC characteristics of the harvested energies, a circuit with a rectifier is required to convert the AC signal to DC output before measuring the power generation. The power generation measurements on load resistors  $R_L$  from  $500\Omega$  to  $120\text{ M}\Omega$  have been carried out. First, the rectified maximum and average voltage  $V_L$  on the  $R_L$  is measured, and then the maximum and average power  $P_L$  on  $R_L$  is calculated by using the equation below:

$$P_L = \frac{V_L^2}{R_L}, \quad (4-1)$$

and as an example, the measured power on  $R_L$  is shown in Figure 4-8. The power increases when the resistance of  $R_L$  increases, which will reach a maximum value before it decreases. The measured maximum average power is  $0.17\ \mu\text{W}$  and the  $R_L$  is  $80\text{ M}\Omega$ , which means the internal resistance is about  $80\text{ M}\Omega$ . The maximum power output on this macro scale CNF-PZT cantilever is  $2.1\ \mu\text{W}$ . The sample cantilever has a CNF  $30\ \mu\text{m}$  in thickness and the light intensity of  $0.13\ \text{W}/\text{cm}^2$  and the thermal radiation (temperature change) of  $22\ ^\circ\text{C}$  is from the Olympus lamp. The data is shown in Figure 4-9.

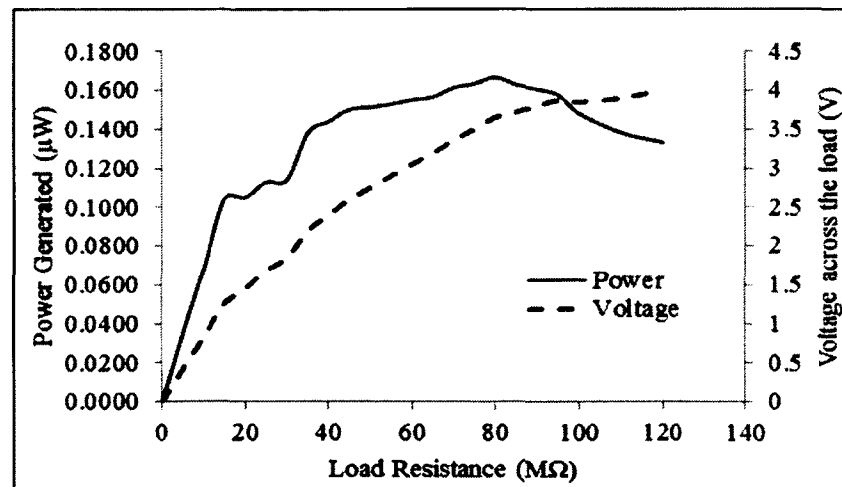


Figure 4-8 Measured average voltage and corresponding power generated over load resistances with light intensity  $0.025\ \text{W}/\text{cm}^2$  and thermal radiation of  $15\ ^\circ\text{C}$ .

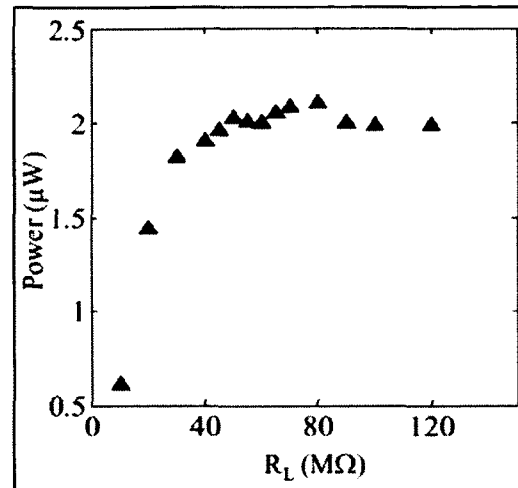


Figure 4-9 Optimal and maximum power output from the macro scale CNF-PZT cantilever which has  $30 \mu\text{m}$  CNF with the light intensity of  $0.13 \text{ W/cm}^2$  and thermal radiation (temperature change) of  $22 \text{ }^\circ\text{C}$ .

#### 4.4 Disadvantage of Prototypes

From the power output measurement, the maximum power output is achieved when the value of load resistance matches the internal resistance of the cantilever.

Thus, the internal resistance is about  $80 \text{ M}\Omega$  which essentially comes from the PZT material. It should be noted that for the current prototype device, the power generation capability is essentially limited by the huge internal resistance of the device, since the large resistance will restrict the current flow. Experiments have found that the short circuit current generated by the prototype device is less than  $0.1 \mu\text{A}$ . The small current output will make it lose the ability to charge a battery [90]. Based on the equivalent circuit in Figure 4-7, it is anticipated that the output power can be improved by optimizing the thickness of each layer of the cantilever structure, decreasing the internal resistance ( $R_i$ ) of the device or by operation using arrayed devices.

#### 4.5 Summary

In summary, a prototype energy harvesting device based on a CNF-PZT cantilever is designed, fabricated, demonstrated, and its power generation capability has been evaluated. The unique self-reciprocating property, which was observed on a CNF-Cu cantilever, has also been confirmed on a CNF-PZT cantilever which is very attractive and profoundly useful for the harvesting of light and thermal energies. Without this property, in order to achieve the cyclic bending of the CNF-PZT cantilever, and thus generating electrical power, the light and thermal sources have to be modulated or simply turned on and off periodically. For a typical device of 20 mm in length, 8 mm in width, 300  $\mu\text{m}$  in thickness, the open circuit voltage can be up to 8V. The cantilever has also been successfully used to harvest solar energy from a sun simulator. With a CNF of 30  $\mu\text{m}$  in thickness, the maximum generated power is in the range of 2  $\mu\text{W}$  when the load resistance is about 80  $\text{M}\Omega$ . Analysis indicates that the output power can be enhanced significantly by optimizing the thickness of each layer, reducing the internal resistance of the device, or by operating arrayed devices.

## CHAPTER FIVE

### DESIGN AND FABRICATION OF FIRST GENERATION MICRO- SCALE ENERGY HARVESTING DEVICE

#### 5.1 Introduction

In the previous section, a self-reciprocating characteristic of CNF-based cantilever, CNF-Cu cantilever, has been observed and analyzed upon exposure to light and thermal radiation. As long as the CNF-based cantilever is exposed to light and/or thermal radiation, it will bend repeatedly. This unique property has been used to design a macro scale CNF-lead zirconate titanate (PZT) cantilever. Self-reciprocation and harvesting both solar and thermal energy with the prototype device has been demonstrated. However, since the internal resistance of the prototype macro scale cantilever device is very large (up to 80 M $\Omega$ ) and thus most of the power is been consumed by the device itself, the output power is only in the range of several micro watts per device. In order to address this issue, the internal resistance should be significantly reduced. Further, in order to scale up the output voltage and the output power, arrayed devices would be used. This can be achieved by scaling the macro scale cantilevers down to micro scale cantilevers. In this chapter, the details of the design and fabrication for the first generation micro energy harvesting device will be addressed.



## 5.2 Device Configuration and Layout Design

The sketch of the microcantilever is given in Figure 5-1(a) and the cross sectional view of the microcantilever is shown in Figure 5-1(b). The microcantilever consists of one PZT layer sandwiched between two Pt-electrode layers, one CNF layer and one SU-8 layer. The typical thickness for each layer is listed in Table 5-1 below. A number of microcantilevers with different dimensions have been designed. The width of the microcantilever ranges from 10  $\mu\text{m}$  to 30  $\mu\text{m}$  and the length is from 100  $\mu\text{m}$  to 350  $\mu\text{m}$ .

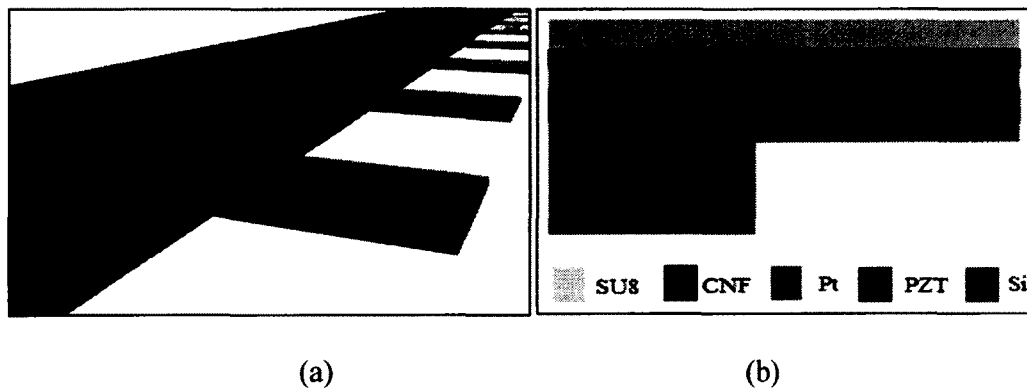


Figure 5-1 (a) 3D Sketch of microcantilever array; (b) cross section view of a microcantilever. (Not to scale)

Table 5-1 Designed thickness for each layer of the microcantilever

Material	Thickness ( $\mu\text{m}$ )
SU-8	3
CNT	2
Pt	0.2
PZT	0.3

The top view of the whole energy harvesting microdevice is shown in Figure 5-2. It consists of a pair of top and bottom electrodes for wire bonding, a supporting anchor and the cantilever for energy generation. The layout of the microcantilever is designed using Tanner L-Edit software. A screen shot of the layout is shown in Figure 5-3. Seven masks are needed for the fabrication processes, such as defining the electrodes, and patterning different layers of the cantilever. The detailed fabrication process flow is described in the next Section 5.3.

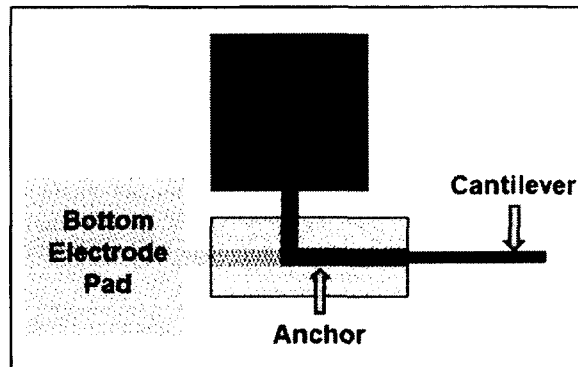


Figure 5-2 Top view of the energy harvesting microdevice. It consists of electrodes, anchor and cantilever.

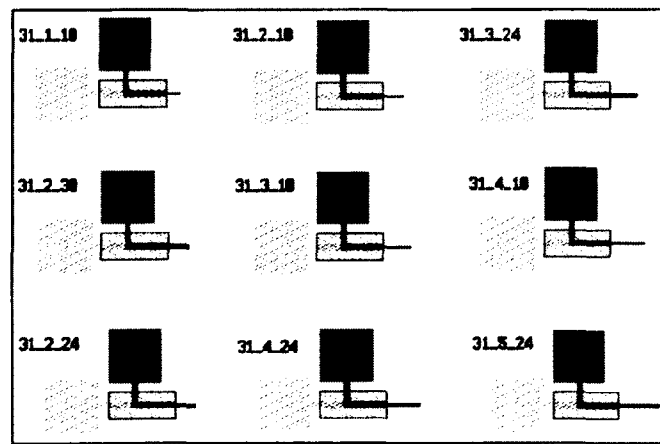


Figure 5-3 Layout design of different dimensions of energy harvesting microdevices in Tanner L-Edit.

### 5.3 Micro Fabrication Processes, Results and Discussion

The detailed fabrication process flow is illustrated in Figure 5-4.

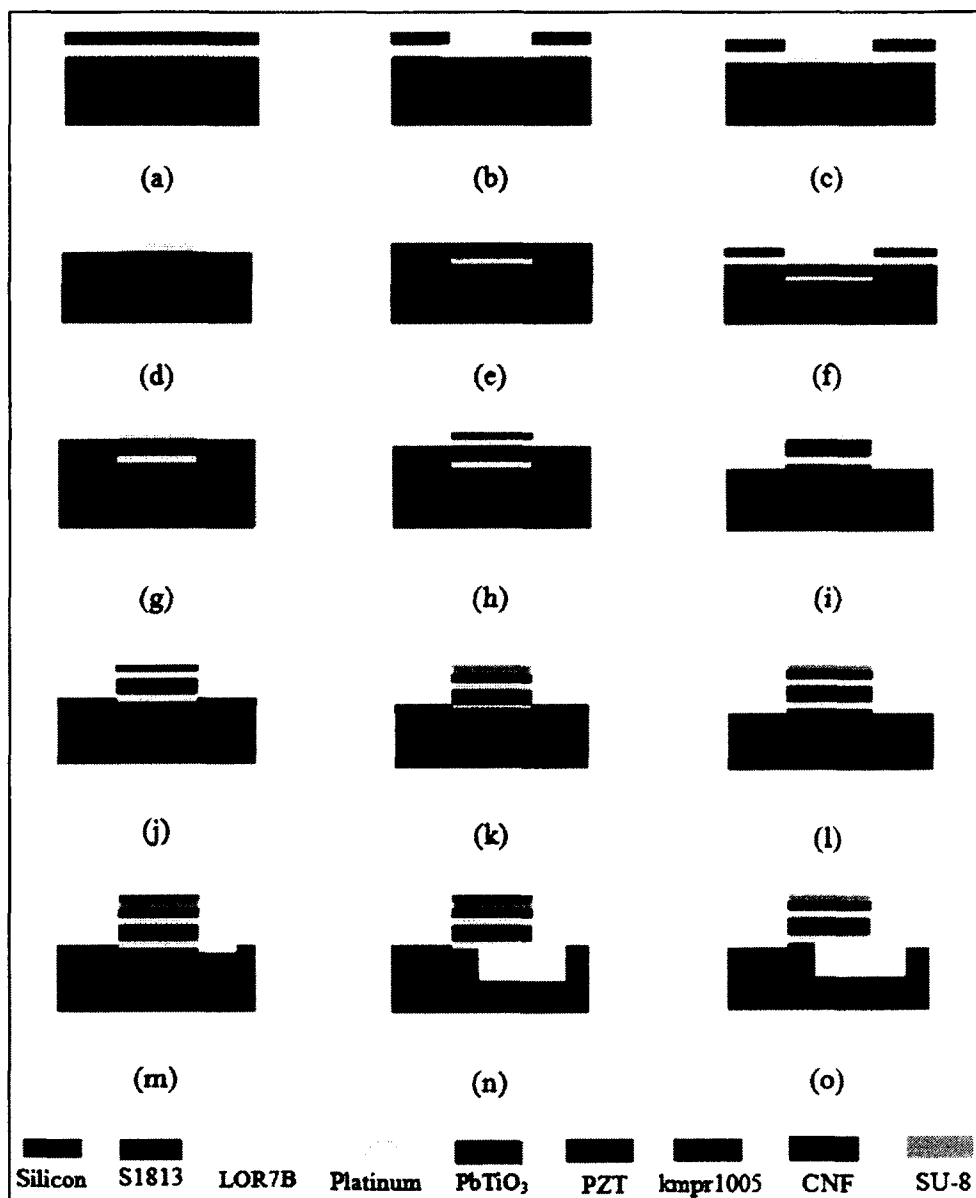


Figure 5-4 Microfabrication processes flow for energy harvesting microcantilever: (a) to (d) patterning bottom electrodes using bi-layer lift-off process; (e) thin-film PZT growth; (f) to (g) patterning top electrodes using bi-layer lift-off process; (h) to (i) etching PZT thin-film; (j) transfer CNF; (k) pattern SU-8; (l) etching CNF; (m) patterning cantilever releasing window; (n) release cantilever; (o) remove S1813.

It involves two main steps: the preparation of CNF using the vacuum filtration method followed by the transfer of CNF to a silicon substrate for further microfabrication and integration.

The fabrication is started with a blank 4-inch p-type (100) silicon wafer. Acetone and IPA bath is used to clean the Si wafer and rinse with DI water. The wafer is dehydrated on a hotplate at 250 °C for twenty minutes. The first step is to pattern the bottom electrode of the microcantilever [Figure (a-d)]. A bi-layer lift-off process using LOR 7B (MicroChem, Inc.) and S1813 photoresist (Shipley, Inc.) is utilized in order to get high yields and better resolution. The developing rate for LOR 7B is slightly faster than S1813 in developer MF-319 can be controlled by the soft bake process. An undercut will be formed in this situation to help the lift-off process as in Figure 5-4 (b). Platinum is deposited on the substrate by sputtering. Prior to platinum, titanium is coated first for adhesion improvement. The designed thickness of the platinum electrode is 200 nm with 20 nm thick Ti underneath. The bottom electrode patterns are formed from lift-off in an EBR-PG (MicroChem, Inc.) bath. The strip efficiency is accelerated by using an ultrasonicator. The micro photo of the patterned bottom electrode is shown in Figure 5-5.

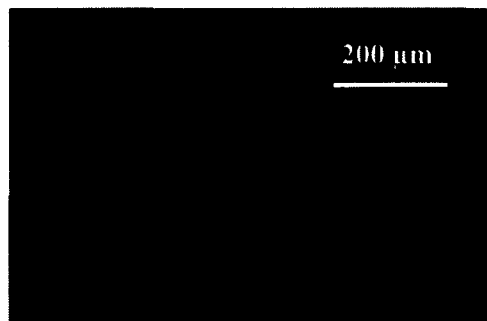


Figure 5-5 Bottom electrode is patterned on the substrate by bi-layer lift-off process.

Piezoelectric material is coated afterwards on the whole wafer. A sol-gel process with proper annealing procedure is utilized for minimal cracking and delamination [91]. In order to prevent or minimize the cracks in the PZT layer, a seed layer of  $\text{PbTiO}_3$  (PT) is used, which can provide nucleation sites and therefore stabilize the crystal orientation of the PZT. One PT layer plus three PZT layers are supposed to result in about 500 nm to 1  $\mu\text{m}$  thickness. More specifically, a seed layer of PT sol-gel (1 wt% - 125/100, MMC Sanda plant) layer is spin-coated with the final speed 1500 rpm. The wafer is then placed on a hot plate for 10-15 minutes at 110°C. The soft baked wafer is then placed in the oven at 550 °C for 6 hours. The wafer is left to cool down in the oven overnight. Thereafter the first layer of PZT sol-gel (15 wt% - 125/52/48, MMC Sanda plant) is spin-coated on the wafer. The wafer is heated on the hot plate for 10-15 minutes at 110°C and transferred to the oven at 550°C for 6 hours. Similarly, the wafer is left to cool down overnight. The processes for the second and the third layer of PZT are identically repeated as the first layer of PZT. The entire wafer with PT plus PZT is finally annealed at 650°C for 6 hours and then cools down to room temperature in the oven [Figure 5-4 (e)]. Cracks are still found after the final annealing process on silicon of the substrate from the residual stress introduced due to the thermal expansion mismatch between the PZT film and the layer underneath [92] but not observed above the bottom electrode region with platinum coating. Therefore, they have no bad effect on the power generation.

A 200 nm thick top platinum electrode plus a 20 nm titanium underneath as an adhesion layer are patterned on the PZT layer using the same bi-layer lift-off method as that for the bottom electrode [Figure 5-4 (f-g)]. The micrograph of the device in Figure 5-6 shows the bottom and top electrodes with  $\text{PbTiO}_3$  and PZT sandwiched in between.

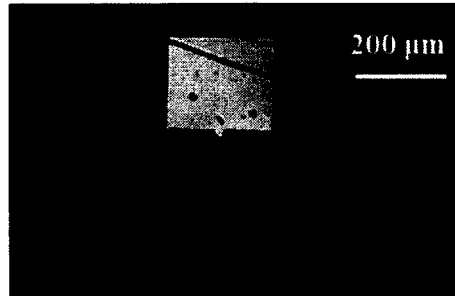


Figure 5-6 Micrograph of the whole device with bottom and top electrode and the  $\text{PbTiO}_3$  plus PZT layer in between the micro-cantilever.

In order to pattern the PZT as a part of the micro-cantilever, a reactive ion etching (RIE) process (Tegal 6500 CCP etch system) is used. Since these gases ( $\text{Cl}_2$ , Ar,  $\text{CF}_4$ ) in the RIE process can slightly damage the platinum electrode, a layer of photoresist (MicroChem KMPR 1005 negative resist) is therefore patterned above the top electrode as a protection mask during the etching process of the PZT film [Figure 5-4 (h)]. Another mask is used to protect both the top and bottom electrodes once the PZT above the bottom electrodes is etched away and the bottom electrodes are exposed. Furthermore, the photoresist pattern size is slightly larger than that of the electrode in order to provide protection to the electrode sidewall. In order to ensure that the exposed PZT layer will be totally removed, which is critical for the step to release the cantilever, the PZT layer is intentionally over etched. The Si underneath the PZT layer is removed by the RIE etching to ensure the substrate will be exposed. After the etching of the PZT layer, the protective photoresist layer is removed [Figure 5-4 (i)]. The PZT etching parameters used in the Tegal 6500 CCP system, is given in Table 5-2.

In the following, CNF needs to be prepared and transferred to the devices. Since the device is in the micro scale, the CNF thickness should be reduced as compared to a macro scale prototype device in order to improve the flexibility. The thickness of CNF is

designed to be 2  $\mu\text{m}$ , as shown in Table 5-1. Depending on the thickness and size of the CNF to be prepared, a certain amount of the AP-SWCNTs (Carbon Solutions, Inc) is purified by nitric acid reflux, cycles of washing and cross-flow filtration. Thereafter, CNTs will be dispersed in an appropriate volume of isopropyl alcohol (IPA) and agitated using a strong ultrasonicator for their uniform dispersion in the solution. As shown in Table 5-3, different weights of CNTs and volume of IPA have been tried for a variable thickness of CNF. It is found that 1 mg of CNTs and 15 ml of IPA result in 2  $\mu\text{m}$  CNF as desired.

Table 5-2 Recipe for PZT etching in Tegal 6500 CCP system

Gas Flow Rate (sccm)			Pressure	Power (W)		ESC Clamping	Substrate Cooling
Cl <sub>2</sub>	Ar	CF <sub>4</sub>		High Frequency	Low Frequency		
7	45	28	5 mTorr	500	125	500 V	He Pressure

Table 5-3 CNF thickness test from different amount of CNTs and IPA

SWCNT weight (mg)	IPA volume (ml)	CNF thickness ( $\mu\text{m}$ )
1	15	2
0.6	10	1
0.3	10	0.5

The CNTs suspension is vacuum-filtered through a mixed cellulose ester (MCE) filter (Whatman) which is 47 mm in diameter and has a 0.2  $\mu\text{m}$  pore size. The resulting CNF on the filter is rinsed twice with IPA and deionized water and then dried in a vacuum system for 4 hours. Then the dried CNF is cut into small rectangular shape and

placed on the wafer where the devices are located. All the CNFs are wetted by water using a cotton swab. The wetted CNFs intimately contact with the substrate due to the surface tension. Being different from the macro prototype device, the resulting CNF is very easy to rip since it is thinner compared to the one used in the macro device. A compression loading method has been applied. The setup and resulted CNF on the substrate are shown in Figure 5-7 and Figure 5-8.

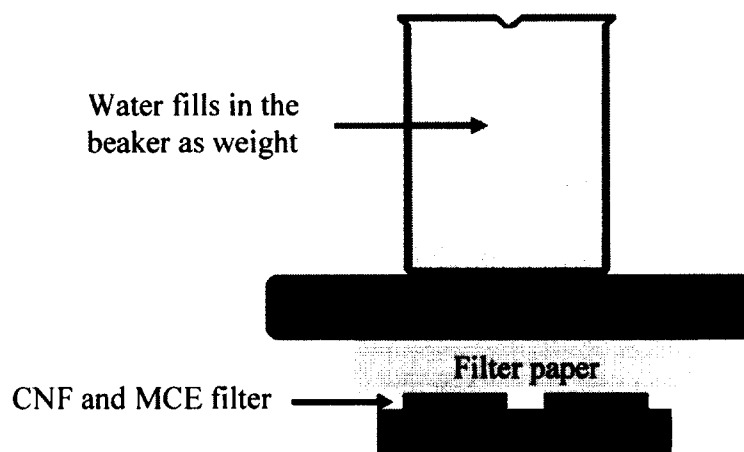


Figure 5-7 Setup of compress loading for transferring CNF tightly onto the substrate.

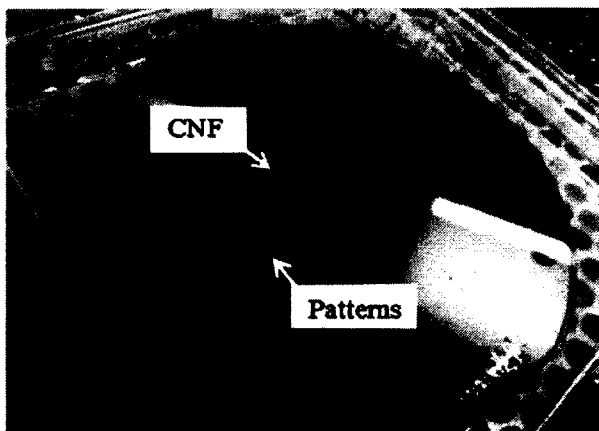


Figure 5-8 A photo shows CNF transferred to a patterned 4-inch silicon wafer.



In order to go through further processes, it should be stuck strong enough to the substrate to endure the following process steps. A compression loading method is utilized to satisfy this requirement. Figure 5-7 shows the setup for this method. 3.5L of water in a beaker acts as a weight when placed on a glass plate plus a few filter papers for compression loading of the CNFs tightly onto the substrate. Ten hours at 35°C in the oven is needed to completely dry the wetted CNFs. Before taking out the substrate, the oven should be turned off and cool down to room temperature. Since the surface tension gives sufficient adhesion of the CNFs to the substrate, the whole wafer can be transferred into acetone bath to remove the MCE membrane [Figure 5-4 (j)]. Five fresh acetone baths are used during the removal process followed by two IPA rinse baths. Then the wafer is placed on a hotplate to dry at 50 °C for a few minutes.

Thereafter, SU-8-10 (MicroChem) is patterned above the CNF, as shown in Figure 5-11 (a), which serves as the mask to protect the CNF underneath and a solid part of the microcantilever [Figure 5-4 (k)]. Another reason for choosing SU-8 is because it has very high optical transparency above 360 nm which will allow the light and thermal radiation to travel through to reach the CNF underneath. The CNF pattern is defined by oxygen plasma in an ICP system (Alcatel A601E). Previous research by other groups has shown a fast etching rate for CNF. S. Lu, et.al. reported ~4 nm/s in their system (ICP power of 200W, bias power of 100W, and O<sub>2</sub> flow rate of 50 SCCM) [2]. A. Behnam, et.al. did a complete research for CNF etching and selectivity. They found that the typical etching rate for CNF is 2.37 nm/s in their ICP-RIE system (ICP power of 300 W, bias power of 100 W, O<sub>2</sub> flow rate of 20SCCM, chamber pressure of 45 mTorr) [93]. In the Alcatel A601E system, different parameters for CNF etching rate have been tested. The

optimal recipe for etching CNF using the ICP system is listed in Table 5-4. Fifteen minutes etching time is conducted to test the etching rate for CNF. The etching profile was measured by KLA-Tencor Alpha-step profilometer and the results are showed in Figure 5-9. The etching rate resulting from this recipe is around 1.2 nm per second. The etching profile of Su-8 is shown in Figure 5-10.

Table 5-4 Recipe for etching CNF by ICP oxygen plasma system

O <sub>2</sub> Flow Rate	Pressure	Main Power	Bias
100 SCCM	80% Valve open	800 W	100 V

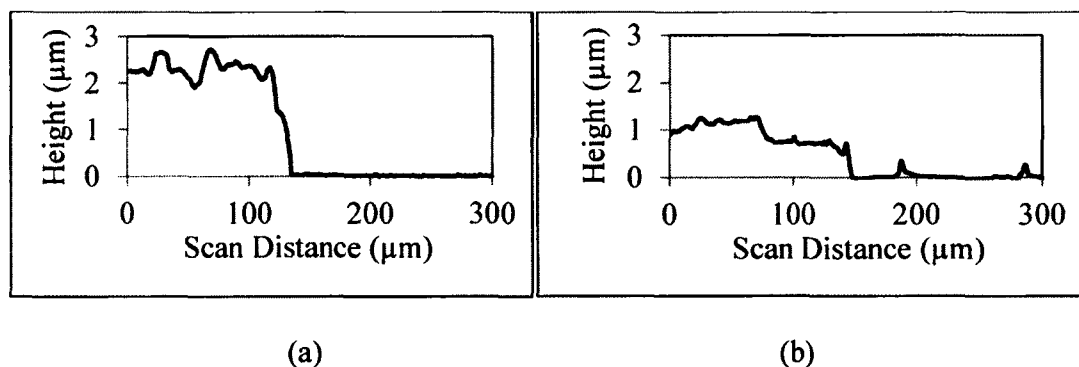


Figure 5-9 Etching profile of CNF (a) before etching; (b) after 15 minutes etching.

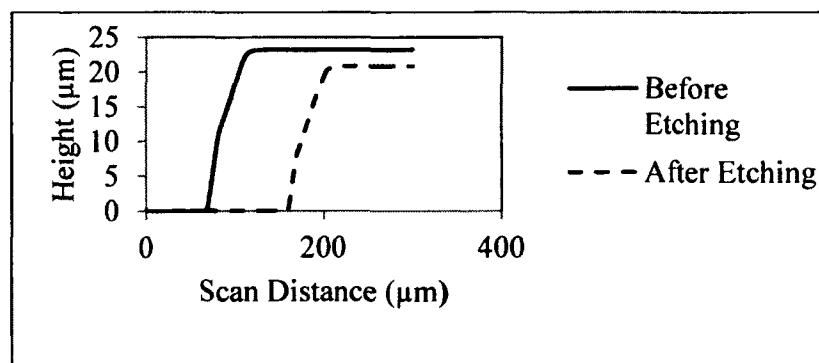


Figure 5-10 Etching profile of SU-8 before and after 5 minutes etching.

It is found that SU-8 is also etched under O<sub>2</sub> plasma. In order to get the desired thickness of the SU-8, the etching rate for SU-8 is needed. Therefore, dry etching testing is conducted for SU-8 and the profiles in Figure 5-10 show the result for 5 minutes of etching. It is found that the etching rate for SU-8 is around 0.4 μm per minute.

For a CNF with a initial thickness of 2 μm, about 100 nm thick transparent CNF remains after 35 minutes ICP etching [Figure 5-4 (l)]. Based upon our experiments, this thin layer of CNF cannot be totally etched away. However, based on the observation, the gas molecules can go through thus, it does not affect the following cantilever release step. From the previous result, SU-8 of 17 μm in thickness is coated. After ICP etching, the remaining SU-8 layer is about 2.5 μm on the microcantilever. Figure 5-11 shows the photos of SU-8 patterned on the CNF and the ICP O<sub>2</sub> plasma etching result.

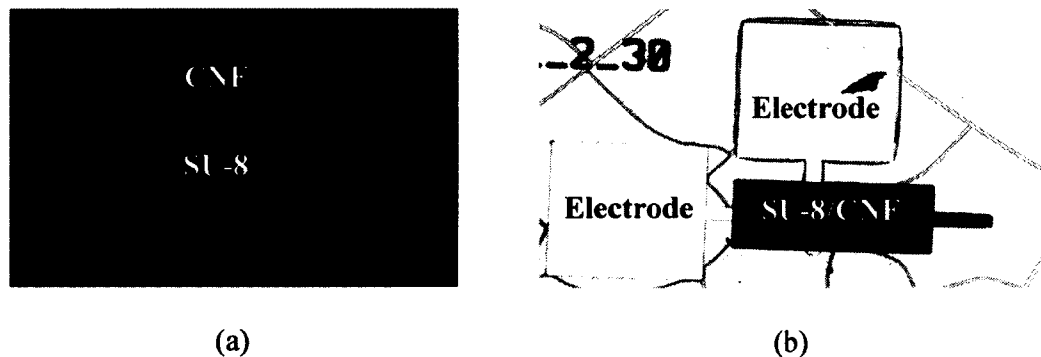


Figure 5-11 O<sub>2</sub> plasma ICP etching result: (a) before ICP etching; (b) after ICP etching.

In order to avoid stiction problem from wet etching, the microcantilever is released from the silicon substrate by a XeF<sub>2</sub> gas based isotropic etching process (Xactix XeF<sub>2</sub> dry etching system). With the intention to get faster etching rate, etching windows are defined by S1813 photoresist which is located at the micro-cantilever region [Figure 5-4(m)]. Figure 5-12 shows the photo of the etching window for one device. During the

etching process, the  $\text{XeF}_2$  gas reacts only with the limited exposed substrate defined by the etching window.

With 3.5 Torr  $\text{XeF}_2$  gas pressure, 2 minutes per cycle, 25 cycles are enough for completely releasing the microcantilever with dimensions of 350  $\mu\text{m}$  long and 30  $\mu\text{m}$  wide, and ensuring that the cavity underneath the cantilever is deep enough for the cantilever to vibrate [Figure 5-4 (n)].

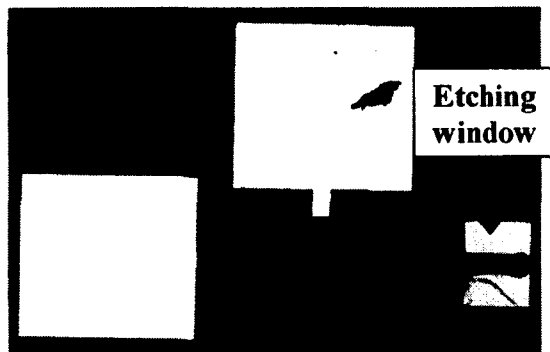


Figure 5-12 Micrograph of device with etching window.

It should be noted that before releasing the cantilever, the wafer should be rinsed in BOE solution for a few seconds to briefly remove any possible native oxide layer which could block the access of the  $\text{XeF}_2$  gas to the silicon even if it is only 1 nm. Since PZT could be damaged by hydrogen fluoride (HF), time should be very carefully controlled. Furthermore, the  $\text{XeF}_2$  system needs a very low humidity environment because HF can be produced from the reaction of water and  $\text{XeF}_2$  gas and damage the PZT [41]. In addition, it could also form a thin film on the device, which would significantly slow down the etching rate of Si. To this end, the water on the wafer is dried by a spin dryer and then put on a hotplate at 100 °C for 1 minute to remove any moisture. Moreover, during the etching process, the chamber is set to keep the temperature at 40°C.

Figure 5-13 below shows the micrograph of a released micro-cantilever. Notice that the tip region is out of the focus plane and appears blurred since it is bent up to some extent due to the creep introduced by residual stress during the heating and cooling process. There are also a number of cantilevers that are bending down for the same reason. Hence, during the releasing step, care should be taken to make the cavity underneath the cantilever deep enough to avoid its touching the bottom of the cavity.



Figure 5-13 Micrograph of a released cantilever.

The photoresist S1813 is finally stripped in an acetone bath. An SEM image of a entire fabricated CNF-PZT microcantilever energy harvesting device is shown in Figure 5-14 (a). The close-up of the cantilever region is shown in Figure 5-14 (b). The total thickness of the cantilever is about  $4.5 \mu\text{m}$ . In order to directly measure the cavity depth underneath and the profile of the released microcantilever, a 3-D optical image close up of the cantilever as shown in Figure 5-15, has been obtained by a confocal laser scanning microscope (Olympus, Inc). The cantilever bends downward, which is due to the residual stress in the microcantilever. The depth of the cavity is about  $103 \mu\text{m}$ . Since the vision of the laser scanning microscope cannot penetrate the solid material, it cannot distinguish solid material and its shadow underneath. The yield from releasing the cantilever is very high ( $>80\%$ ). However, a lot of devices suffered from cracking or missing electrodes

which reduces the number of testable devices. An improved method will be introduced in the optimized design in the following chapter.

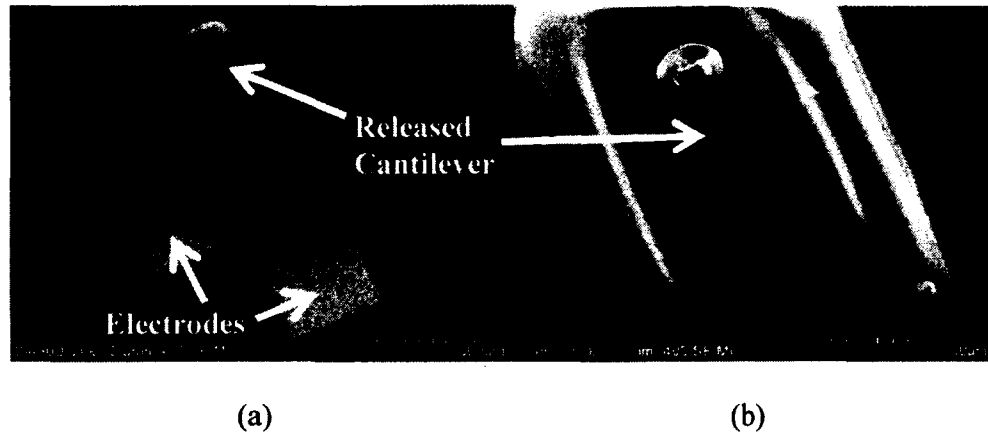


Figure 5-14 SEM images of (a) one of fabricated devices showing the released cantilever and the electrodes; (b) close-up showing the released cantilever.

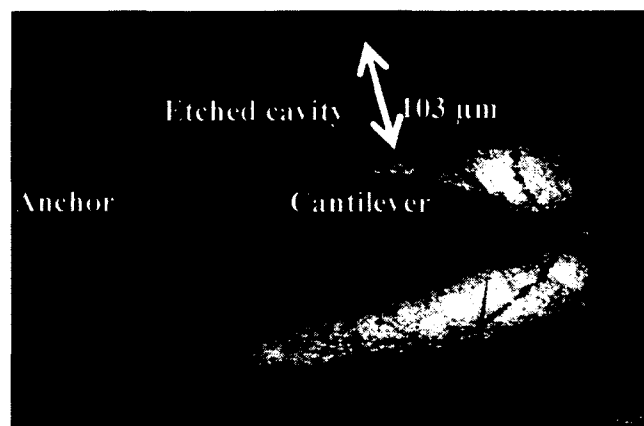


Figure 5-15 A 3-D image showing the released microcantilever and the cavity underneath by a confocal laser scanning microscope.

#### 5.4 Summary

In this chapter, scaling down from the macro scale prototype device is proposed to solve the previous mentioned problems, such as high internal resistivity, low output current.

The first generation of the micro scale device is designed. Micro fabrication processes are described in detail. The fabrication of CNF-PZT microcantilevers using CNF-transfer and advanced lithography has been successfully demonstrated. This process consists of a CNF synthesis and transfer process, and a silicon bulk micromachining process, offering a simple approach to fabricate CNF-PZT based microcantilevers.

Since hundreds and thousands of the microcantilevers can be potentially fabricated simultaneously on a single chip, this process can pave the way towards fabricating this type of energy harvesting device in a cost-effective manner. In addition, this fabrication process is also compatible with the standard MEMS fabrication, VLSI fabrication and interconnect technologies, thus, it is suitable for the integration of a variety of MEMS sensors, actuators, integrated circuits for drive and control electronics on a single chip, thereby forming self-contained and self-operated microsystems.

## CHAPTER SIX

### INITIAL TESTING AND ANALYSIS FOR THE FIRST GENERATION MICRO-SCALE ENERGY HARVESTING DEVICE

#### 6.1 Introduction

In the ambient environment, energy exists everywhere, such as light (solar) energy, thermal energy, electromagnetic (E-M) energy, wind energy, mechanical energy, etc. However, usually the energy from these sources is found in such tiny quantities that it cannot supply adequate and sufficient power for operating electronic devices, sensors and circuits. Due to the steady advancement of energy harvesting technologies for the past decades, this scenario is set to change. Energy harvesting simply is a process of capturing minute amounts of energy from one or a multiple of these naturally-occurring energy sources, accumulating them and storing them for real-time or later use. The efficiency of the energy harvesting devices in capturing trace amounts of energy from the environment and transforming it into electrical energy has been steadily improved, indicating their great potential for practicable applications.

Due to its significance in many aspects, energy harvesting for self-powering has been a very vigorous research area. Nowadays, extensive research efforts have been underway for harvesting a variety of different forms of energy from the environment using different materials and technologies, which have been addressed in Chapter One.



Among the energy sources available in the environment, solar energy and thermal radiation energy are particularly attractive due to their environmental by friendly characteristic, unlimited availability and suitability for different applications including harsh environment applications (e.g., outer space). Solar cells can potentially provide a long lifetime operation at an acceptable power density of  $10 \text{ mW/cm}^2$  under direct sunlight but need light for operation. However, sunlight cannot be available at all times, thus a device that can harvest from multiple energy sources is an ideal solution. In this dissertation, a CNF-PZT cantilever based device is designed to harvest both solar and thermal energies. Furthermore, the cantilever structure is traditionally and routinely used for harvesting ambient mechanical vibrational energy. Therefore, this system is a solution to achieve hybrid energy harvesting.

## 6.2 Poling and Device Validation

The fabricated micro devices need to be polarized and DC actuated before testing. The poling process is aimed to increase the polarization characteristics so that the piezoelectric coefficient, which in turn, gives better performance for the mechanical to electrical energy conversion efficiency (Figure 6-1). The polarization process is suggested to be done using a strong electric field about  $2000 \text{ V/mm}^{-1}$  at an elevated temperature, but below the Curie temperature [94]. The typical Curie temperature of a PZT thin-film prepared by sol-gel method is above  $300 \text{ }^\circ\text{C}$  [95]. The final PZT thin-film thickness for the micro device with one layer of PT and three layers of PZT is around 250 nm. One volt DC voltage and  $80 \text{ }^\circ\text{C}$  is chosen for application during the poling process and kept for 30 minutes. The electrical connection of the first generation micro-device with the outside world is completed through a probe station system. The tungsten probes

are manipulated to attach to the top and bottom electrodes of the device to form the Ohmic contact (Figure 6-2). DC voltage is applied through the probes to the electrodes. In the meanwhile, the device is heated up to 80 °C by the hotplate underneath. After applying the DC voltage at raised temperature for 30 minutes, the hotplate is turned off. During the cooling down process, the whole wafer is kept on the hotplate, and the DC voltage remains at one volt until the devices return to room temperature.

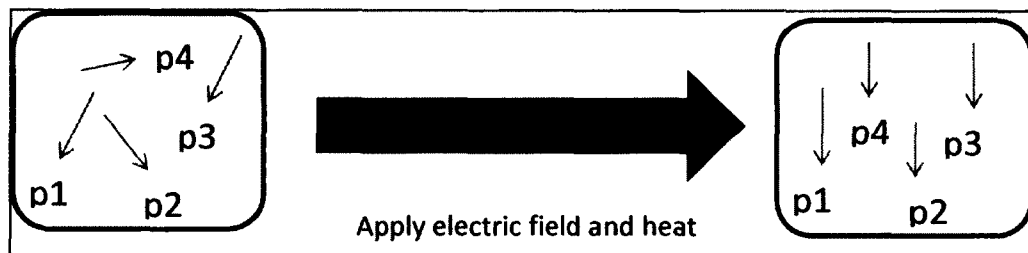


Figure 6-1 Poling effect for piezoelectric material. Direction of the arrows stands for the polarization direction of each unit grain in PZT crystal.

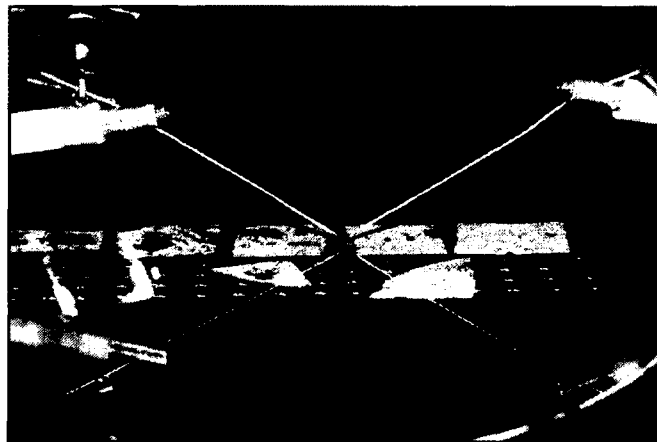


Figure 6-2 A micro energy harvesting device is electrically accessed by a probe station.

Before starting to test the device, a validation experiment is needed in order to verify if the device has been successfully fabricated and functioned properly.

Piezoelectric material is used as a transducer for converting mechanical energy to electrical energy or vice versa. Therefore a piezoelectric device can be either used as an energy harvesting device or an actuator. From this point, a DC voltage is applied to actuate the cantilever. If the device can be successfully actuated, an upward or downward bending action of the cantilever will be observed under the microscope as a response from the DC actuation. The DC voltage is swept from 0 and gradually increased. The observed phenomena for the DC actuation are listed below:

1. Most devices are detected to be bent when the applied voltage is between one to four volts in the designed dimension range;
2. Generally, a device with a larger dimension needs higher DC voltage to actuate;
3. Some of the devices presenting severe bending curvature over other devices after releasing due to higher localized thermal residual stress are found to have tip movement at higher voltage;
4. A few numbers of the devices are not responsive to a DC voltage which indicates a malfunction; these devices are recorded by number and will not be subject to further testing.

### 6.3 Experiments Details

After verifying the functionality of devices, a series of experiments were conducted to evaluate the performance of the device under light and thermal radiation for light and thermal energy harvesting. A photo of the whole setup is shown in Figure 6-3.

The Olympus TL-2 incandescent lamp is used as the white light source which radiates both light and thermal energy. The light power is recorded using a CCD optical power meter (Thorlabs PM100). The light intensity is then calculated by the recorded

light power divided by the CCD sensor area. The lamp will also provide radiation in the infrared range as heat. The temperature characteristic of the lamp output is measured using a data logger thermometer with a thermal couple (Omega HH306).

The open circuit voltage (OCV) and short circuit current (SCC) response of the device to a white light source was studied. The aforementioned probe station system (Micromanipulator) was used to create the electrical connection with the device using a pair of tungsten probes. The OCV and SCC characteristics were recorded by a digital multimeter (Agilent 1252B) with the provided GUI data logger in a terminal PC. In order to confirm the self-reciprocation effect of the cantilever, a control experiment was conducted for recording the OCV of a device without releasing the cantilever.

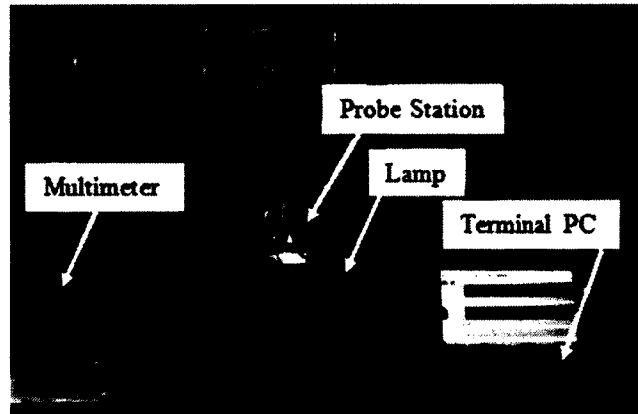


Figure 6-3 Experimental setup for evaluating light and thermal energy harvesting from a single micro-energy harvesting device.

The OCV of the device response to a heat source was studied to demonstrate the thermal energy harvesting. A hotplate was used to provide the thermal energy. The devices were located on the top of the hotplate. The OCV is recorded at different temperature levels which can be adjusted by the hotplate.

Harvesting both light and thermal energy is also exhibited by exposing the device to the lamp and hotplate simultaneously.

#### 6.4 Results and Discussion

The spectrum of the white light source Olympus TL-2 incandescent lamp is plotted in Figure 6-4. It covers all the visible light spectrum range and extends a tail into the ultraviolet region. The highest intensity is located at the wavelength 610 nm. It also generates heat as an incandescent lamp. The temperature and optical intensity output characteristics are described previously in 3.2.2 Figure 3-3.

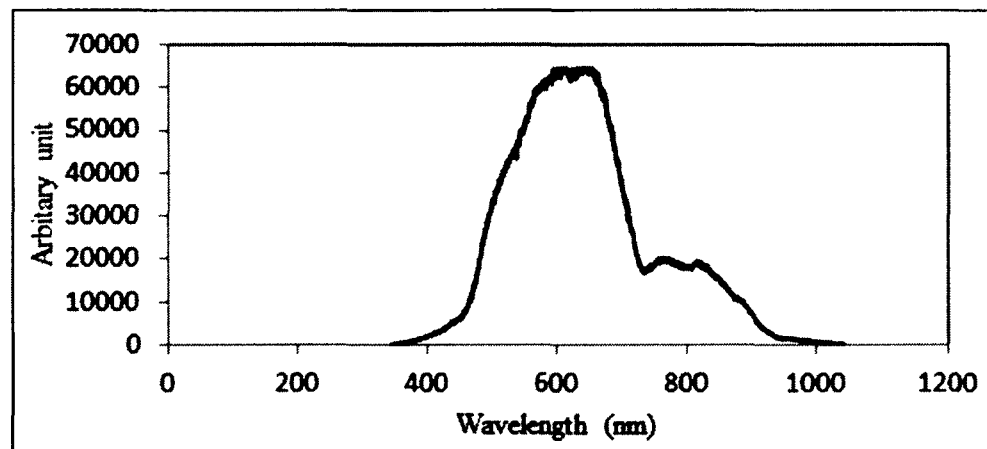


Figure 6-4 Optical spectrum of Olympus TL-2 incandescent lamp.

Figure 6-5 shows a typical open circuit voltage (OCV) output response to the radiation from the Olympus TL-2 lamp of a single micro energy harvesting device. The output optical intensity was  $0.21 \text{ W/cm}^2$  at a wavelength of 600 nm and  $0.014 \text{ W/cm}^2$  at a wavelength of 780 nm. The room temperature was  $20 \text{ }^\circ\text{C}$  and the temperature at the device is around  $30 \text{ }^\circ\text{C}$  which represents a  $10 \text{ }^\circ\text{C}$  difference. The data of the solid line represents a device with the cantilever dimension of  $200 \text{ }\mu\text{m}$  in length and  $25 \text{ }\mu\text{m}$  in

width, which has been successfully fabricated and passed the validation step. The thickness of each layer of different materials is listed in Table 5-1. In order to confirm that the oscillation of OCV comes from the self-reciprocation phenomenon of a released cantilever, a control experiment was conducted on a device in which the cantilever has not yet been released. The dashed line data represents the result from the control experiment with the unreleased cantilever. Before turning on the lamp, the OCV output for the devices without exposing to a radiation source were recorded for 300 seconds as a reference which also indicates the noise level.

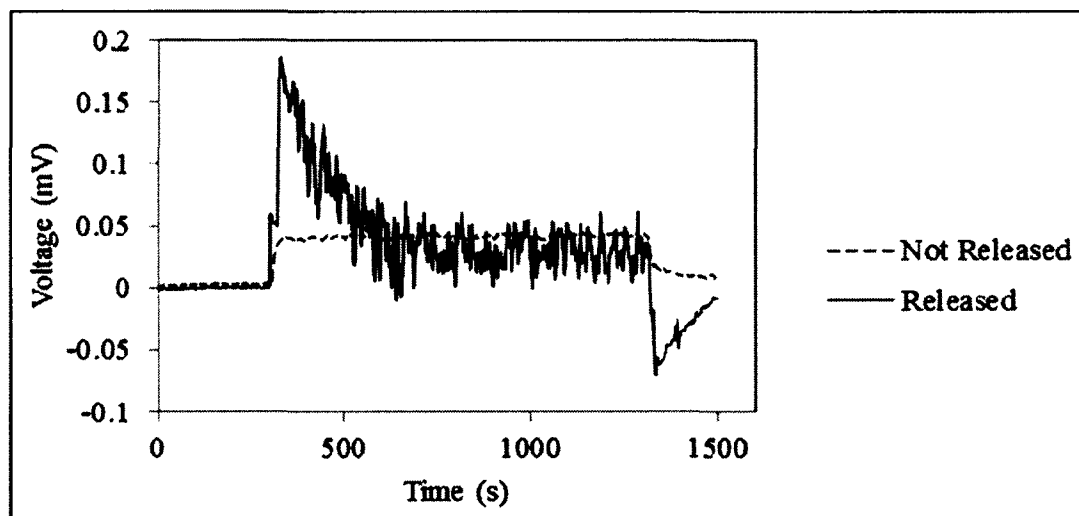


Figure 6-5 Open circuit voltage (OCV) output characteristics response to the Olympus TL-2 white light source ( $0.21 \text{ W/cm}^2$  at wavelength of 600 nm) of a single micro energy harvesting device with a released cantilever (solid line) and another device without releasing the cantilever (dashed line).

After turning on the lamp, the OCV output shows a big jump for the released cantilever, similar to the prototype macro scale device due to a sudden generation of radiation. Thereafter, the OCV is gradually reducing and continuously vibrating as long as the radiation is on. When the lamp was turning off, the OCV reversed in the opposite

direction and finally came back to zero. The whole process is very comparable with the prototype macro scale device. Taking a close up look of the data in Figure 6-6, the maximum amplitude of the peak to peak voltage is about 0.08 mV and 0.05 mV on average. On the other hand, the device without releasing the cantilever did not show peak OCVs when the lamp was turned on and off. In addition, no oscillation of the OCV was observed when the radiation was presented. Notably, a DC shift of the OCV by about 0.04 mV for both cases is displayed in the plot. This is not a casual case only for this group of tests but is observed for the following experiments as well such as in Figure 6-7.

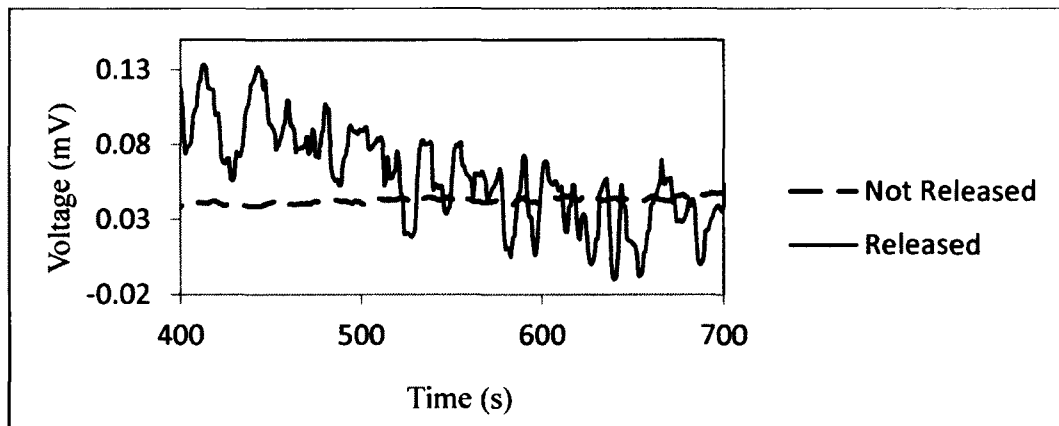


Figure 6-6 OCV output for the micro energy harvesting devices.

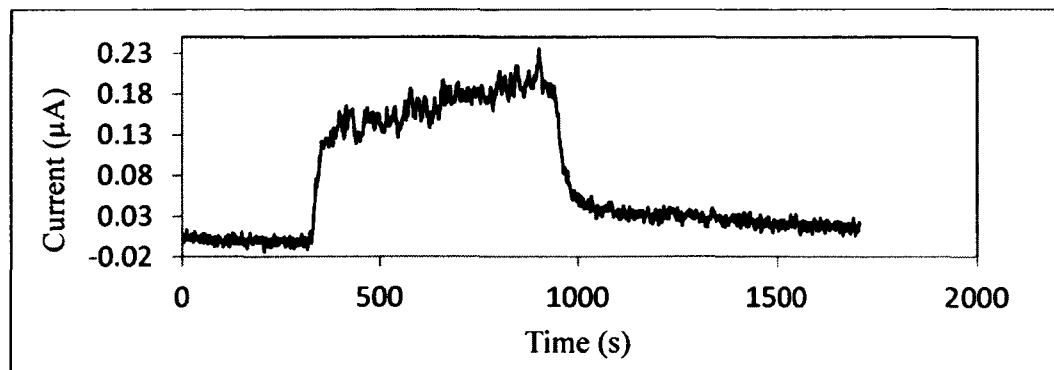


Figure 6-7 Short circuit current (SCC) output for a single device exposed to lamp.

The mechanism for the generation of DC voltage is basically from the thermoelectric effect, and details will be addressed in the following chapter.

The short circuit current (SCC) was measured with the same condition as for the OCV testing. Figure 6-7 illustrates the result of the short circuit current measurement. A DC shift around  $0.18 \mu\text{A}$  of the SCC is observed. The oscillation of the current from the PZT in the cantilever vibration is about  $0.05 \mu\text{A}$ . However,  $0.01 \mu\text{A}$  oscillation of SCC is detected from the reference recording for the first 300 seconds as noise. It concludes that the output current is fairly small from a single micro device since the PZT material is essentially electrically capacitive in nature.

Figure 6-8 shows the OCV output of the micro device when it is subjected to heat flow from a hotplate for thermal energy harvesting. Three different temperature levels at  $35^\circ\text{C}$ ,  $40^\circ\text{C}$  and  $50^\circ\text{C}$ , respectively, were set by the hotplate. The reference OCV output was taken at room temperature for the first 300 seconds. Once the hotplate was turned on, the temperature was quickly climbing up to the pre-set level and remaining stable at the set temperature. With the temperature increased from room temperature, a clear DC shift was again observed as in previous experiments.

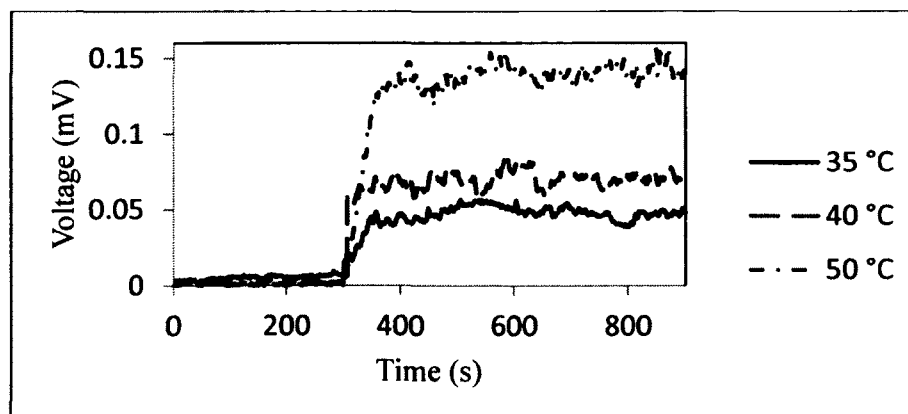


Figure 6-8 OCV of a micro device for thermal energy harvesting.



The higher temperature brought the DC shift higher and the DC shift is almost increasing linearly with the temperature difference between the hotplate and room temperature. There was no clear OCV jump at the turning on point compare to the device response to the Olympus lamp. The OCV outputs started to oscillate obviously once the temperature rose up to the pre-set level. The maximum peak-to-peak AC OCV for 35 °C, 40 °C and 50 °C are about 0.008 mV, 0.02 mV, and 0.025 mV, respectively. The DC shift and maximum peak-to-peak of OCV for each case are shown in Table 6-1.

Table 6-1 DC shift and maximum peak-to-peak OCV for thermal energy harvesting

	35 °C	40 °C	50 °C
DC Shift	0.05 mV	0.07 mV	0.135 mV
Max Peak-to-Peak OCV	0.008 mV	0.02 mV	0.025 mV

By applying light radiation from the Olympus lamp above and the heat from hotplate underneath the device, the device was demonstrated to harvest both light and thermal energy simultaneously. The recorded OCV is illustrated in Figure 6-9. However, the combined effect of light and thermal energy is not simply reflecting to the improvement of the OCV output. When the lamp and hotplate were turned on, the OCV quickly went up but there was no “peak” observed. This is because the temperature went up promptly from the heat of the hotplate and increased the DC shift to a higher level instead of falling down. The overall DC shift was finally stabilized around 0.11 mV, which is higher than the result of the lamp only experiment at 0.04mV but slightly lower than the result from the 50 °C hotplate only experiment at 0.135 mV. The average amplitude of OCV oscillation is about 0.035 mV, close to the value in Figure 6-5

(average 0.05 mV) but slightly higher than the result from the thermal energy harvesting in Figure 6-8 (average 0.012 mV). This result indicates that even though both light energy and thermal energy can cause self-reciprocation of the micro cantilever which, in turn, results in the OCV oscillation; however, the oscillation is randomly distributed and not coupled or synchronized to produce an additive effect. The mechanism for the DC shift was not very clear at this stage and will be addressed in the following chapter.

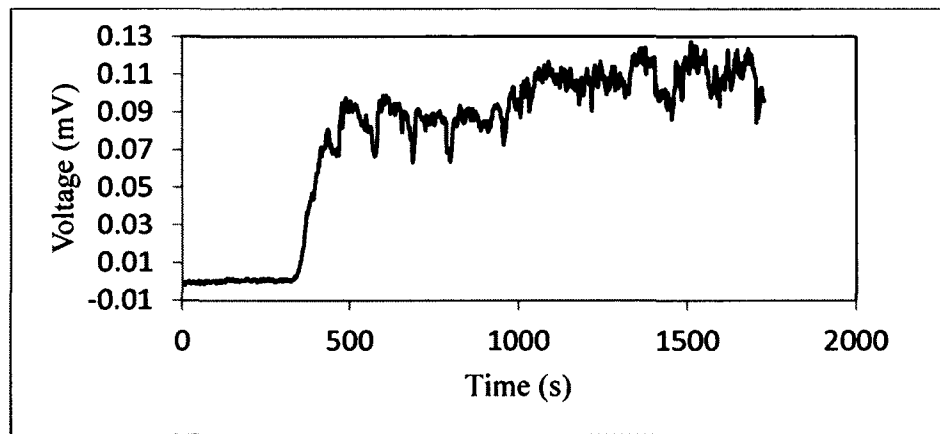


Figure 6-9 OCV output for harvesting light and thermal energy from Olympus lamp (0.21 W/cm<sup>2</sup> at wavelength of 600 nm, 30 °C) and hotplate at 50 °C.

In order to show the advantage of the micro-scale energy harvesting device, the theoretical maximum power output and power density  $\mu$  (power per unit area) using the Olympus lamp as the radiation source for the prototype macro scale device (25 mm $\times$ 5 mm) and the micro device (200  $\mu$ m  $\times$  25  $\mu$ m) are calculated from the equations below:

$$P = \frac{V^2}{4 \times R}, \quad (6-1)$$

$$\mu = \frac{P}{A}, \quad (6-2)$$

where  $P$  is the power,  $\mu$  is the power density,  $V$  is the average peak-to-peak OCV of the oscillation,  $R$  is the internal resistance, and  $A$  is the surface area of a single device. The

maximum power is calculated from the maximum power transfer theorem which indicates that the maximum external power from a source with finite internal resistance is obtained when the load resistance equals to the resistance of the source, as viewed from outside [96].

The results listed in Table 6-2 show that the internal resistance of the micro device is only 50 ohms compared to the 80 mega ohms for the macro-scale prototype device. The power density generated by the micro-scale device is 4445 times that of the macro scale device. This value was taken from the same test conditions: light intensity is  $0.014 \text{ W/cm}^2$  at 780 nm and the temperature difference is  $10 \text{ }^\circ\text{C}$ . The major reason for the improvement is from the largely reduced internal resistance of the device.

Table 6-2 Comparison of the macro-scale device and the micro-scale device

	R ( $\Omega$ )	A ( $\text{m}^2$ )	V (V)	P (nW)	$\mu$ ( $\mu\text{W/cm}^2$ )	Ratio of $\mu$
Macro	$8 \times 10^7$	$1.25 \times 10^{-4}$	0.15	0.07	$5.625 \times 10^{-5}$	1
Micro	50	$5 \times 10^{-9}$	$5 \times 10^{-5}$	0.013	0.25	4445

### 6.5 Summary

In this chapter, the methods for poling and validation of a device were described. The validation step found that about 30 percent of the devices work properly. The failure for the other devices are caused by complex reasons, such as cracks in the electrodes, breakage of the cantilever, delamination of SU-8 from CNF, over etching, localized high residual stress, failing to release, etc. The working devices were evaluated for energy harvesting performance for light and thermal energy harvesting. The open circuit voltage (OCV) output response to the Olympus TL-2 lamp is very similar to the macro scale

device which indicates that the self-reciprocation phenomenon is also valid for the micro-scale device. The device was also demonstrated to harvest thermal energy from a hotplate. Experiments show that both light and thermal energy can be harvested by the micro-scale devices. An obvious DC shift of the OCV, besides oscillation, was observed for each experiment. The mechanism for the generation of DC voltage is not clear at this stage. Further study will be conducted in the following chapter. The estimation of the average power density generation for the micro-scale device is 4445 times higher than the prototype macro-scale device. This significant improvement is mainly the result of the largely reduced internal resistance of the device.

## CHAPTER SEVEN

### FURTHER ANALYSIS AND CONSIDERATION OF MICRO-SCALE ENERGY HARVESTING DEVICE

#### 7.1 Analysis of DC Shift

In the previous chapter, the testing result of open circuit voltage (OCV) and short circuit current (SCC) represent oscillation patterns similar to the one from the prototype macro-scale device which is caused by the self-reciprocation of the cantilever upon receiving radiation energy. However, other than the oscillation, a clear DC shift from the balance was also observed which is different from the macro scale device. The schematic diagram of the overall pattern is illustrated in Figure 7-1.

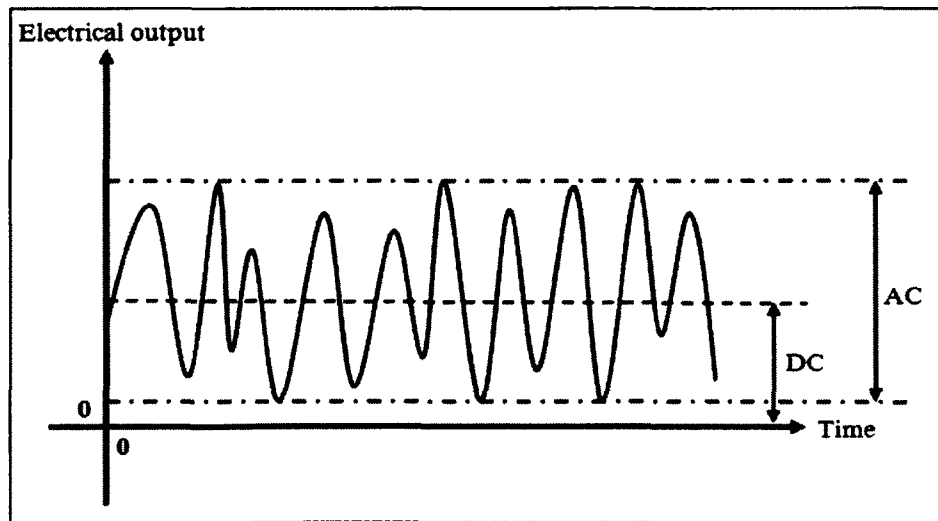


Figure 7-1 Schematic diagram of the electrical output pattern from the micro-scale device.

The mechanisms for energy harvesting were discussed in Chapter One, such as electromagnetic induction, the thermoelectric effect, the photovoltaic effect, and the piezoelectric effect. As discussed in previous chapters, the oscillation of the output is the result of the self-reciprocation of the PZT cantilever from the piezoelectric effect. The DC shift was expected to be generated as a consequence of either the thermoelectric effect or the photovoltaic effect or both of them. In order to study the DC shift effect, a sketch of the equivalent structure of the device is plotted in Figure 7-2.

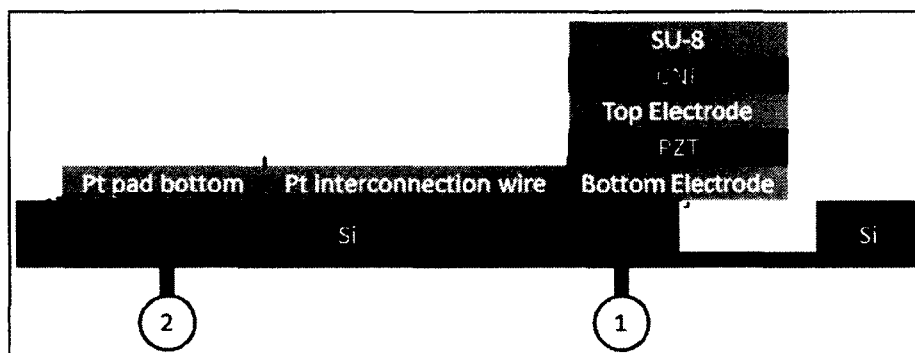


Figure 7-2 Cross-section structure sketch of the micro-energy harvesting device.

Firstly, the energy generation from the photovoltaic effect is considered. Based on Figure 7-2, a metal-semiconductor junction, which possibly forms the Schottky junction solar cell, could generate photovoltaic energy. The metal-semiconductor junction in the diagram can be Pt-Si or Pt-CNF interface. The Si substrate used to fabricate the device is highly doped p-type, which has the doping level from  $3 \times 10^{18}$  to  $2 \times 10^{19}$  boron atoms  $\text{cm}^{-3}$ . The energy band diagram in Figure 7-3 shows the formation of the Schottky junction between a metal and p-type semiconductor. It indicates that the work function of the metal  $\phi_m$  should be smaller than the work function of the p-type semiconductor  $\phi_s$  [13]. The work functions are 5.65 eV and 4.1 eV for Pt and intrinsic silicon, respectively.

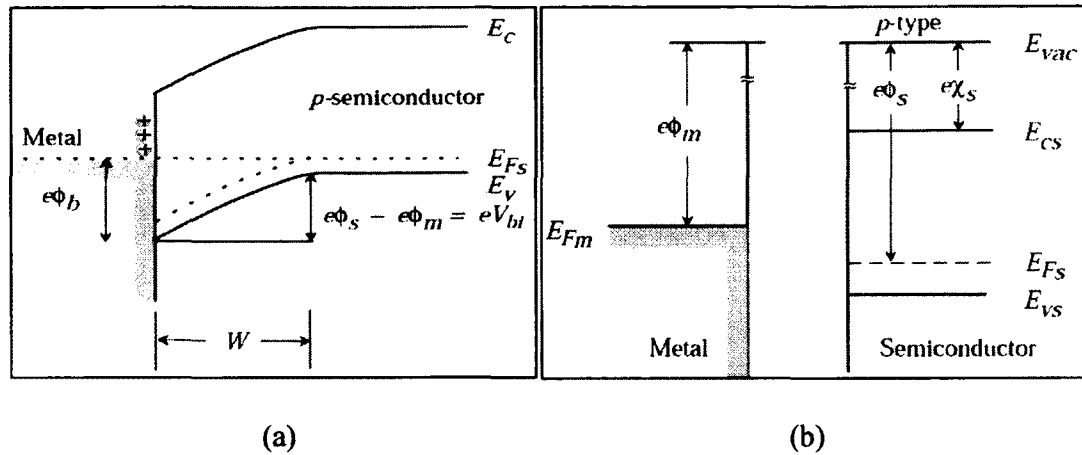


Figure 7-3 (a) energy band diagram of metal and p-type semiconductor before contact; (b) energy band diagram of metal and p-type semiconductor after forming the Schottky junction when  $\phi_m < \phi_s$ .

After doping of boron, intrinsic Si turns into a p-type semiconductor. The Fermi level is shifted; therefore, the work function for p-type silicon needs to be re-calculated. The following equation calculates the Fermi level shift after p-type doping:

$$E_{Fp} - E_{Fi} = -k \times T \times \ln \frac{p}{n_i}, \quad (7-1)$$

where  $E_{Fp}$  stands for the Fermi level after p-type doping,  $E_{Fi}$  for the Fermi level of intrinsic silicon,  $k$  for the Boltzmann constant  $1.38 \times 10^{-23}$ ,  $T$  for the temperature which is assumed to be 300K,  $p$  for the concentration of holes after doping, which is equal to the boron concentration  $3 \times 10^{18}$  to  $2 \times 10^{19} \text{ cm}^{-3}$ , and  $n_i$  for the intrinsic concentration of silicon  $1 \times 10^{10}$  [97]. The calculation shows  $E_{Fp} - E_{Fi} = -0.506$  for  $p = 3 \times 10^{18} \text{ cm}^{-3}$  and  $E_{Fp} - E_{Fi} = -0.555$  for  $p = 2 \times 10^{19} \text{ cm}^{-3}$ . Therefore, the work function for p-type Si  $\phi_s$  is in the range from 4.656 eV to 4.705 eV, which are both not larger than the work function  $\phi_m$  for Pt. Since  $\phi_m < \phi_s$  is not satisfied, the metal-semiconductor junction forms an Ohmic contact and does not contribute to the photovoltaic effect. The CNF is a mixture of 30% metallic and 70% semiconducting single wall carbon nanotubes

(SWCNTs). The 70% semiconducting SWCNTs are not doped, hence the CNF is essentially intrinsic. The intrinsic semiconductor has a low level concentration of free carriers consequently ignored to be formed as the Schottky junction solar cell. It concludes that the DC shift effect is not stemmed from the photovoltaic effect. Thermoelectric effect needs to be checked as in Figure 7-4.

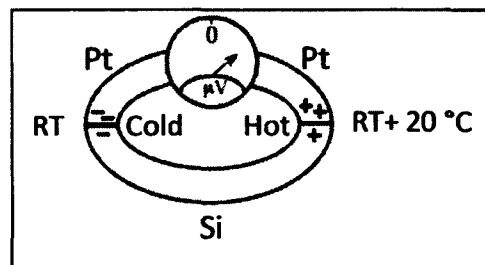


Figure 7-4 Voltage generation between hot and cold ends of the Si-Pt circuit from the thermoelectric effect. (RT = Room Temperature)

Secondly, the thermoelectric effect is evaluated. Thermoelectricity is generated when a temperature gradient is presented to a two dissimilar material system, as in Figure 7-4. From Figure 7-2, a junction can be formed between Si and Pt. The interface between the Si and Pt is located from the bottom electrode at the anchor region to the electrode pad bottom (Figure 7-2). A temperature gradient might be generated between region “1” and “2” in Figure 7-2 during testing. In order to better examine the thermoelectric effect and further study the device, a new layout is designed, as shown in Figure 7-5 below. Compared to the previous design, the dimension of both electrode pads are increased in size in order to easily complete the wire bonding and avoid using the probe station, which has very limited space to manipulate and control the radiation conditions. In terms of fabrication, the new design has optimized the protection mask during PZT and CNF plasma etching and optimized the dimension of the etching window during cantilever



release, which will not only save fabrication time and chemical consumption, but also turn out a higher yield for the new batch of devices.

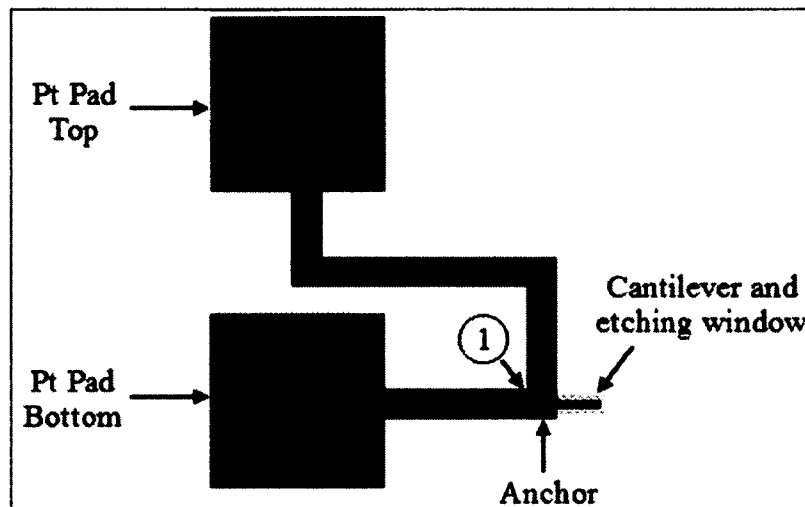
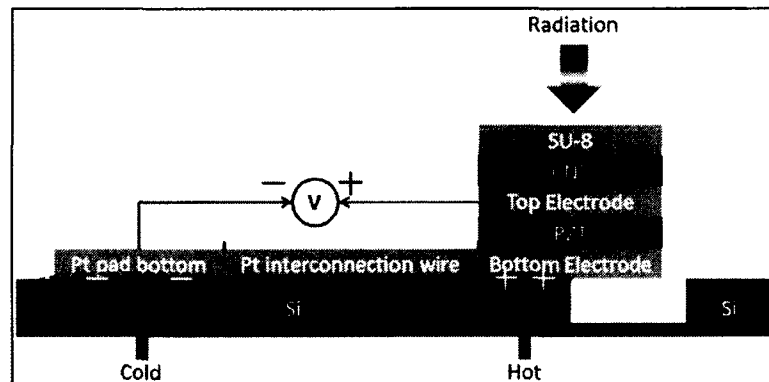


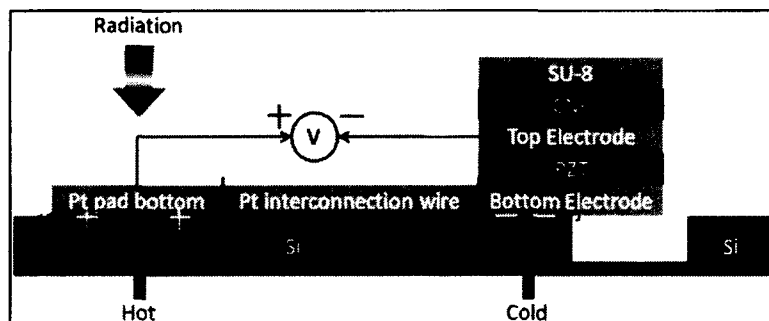
Figure 7-5 New layout design of the micro-energy harvesting device.

In order to verify the thermoelectric effect, the radiation energy was intentionally applied to the anchor (region “1”) and Pt pad bottom (region “2”), respectively, as indicated in Figure 7-2 and Figure 7-5. In the first case, the radiation was mainly focused on “1” by a condenser lens so “1” was the hot end and “2” was the cold end. As the temperature gradient was formed between “1” and “2”, a potential difference was supposed to be generated between the top electrode (grounded) and the Pt pad bottom (negative potential) from the thermoelectric effect, as illustrated in Figure 7-6 (a). The top electrode was at zero potential (grounded) so the open circuit voltage (OCV) reading from the digital multimeter showed positive, as plotted in Figure 7-7 (a). Secondly, the radiation energy was deliberately illuminated on the Pt pad bottom (“2”) by a condenser lens, which results in where “2” was the hot end and “1” was the cold end. The reversed temperature gradient also generated a negative potential difference between the top

electrode (grounded) and the Pt pad bottom (positive potential), as indicated in Figure 7-6 (b). The recorded OCV is plotted in Figure 7-7 (b). Notably, the oscillation is observed in Figure 7-7(a), which is generated from the cantilever vibration, whereas only a DC shift exists in Figure 7-7(b). Since the radiation energy was focused by the condenser lens at each of the ends, the DC shift had increased significantly because of a higher temperature difference, compared to the previous result in Figure 6-5, and is overwhelming the AC part of the OCV. The highest DC shift recorded so far is about one mV when the lamp was brought closer to the device to generate a higher temperature difference.



(a)



(b)

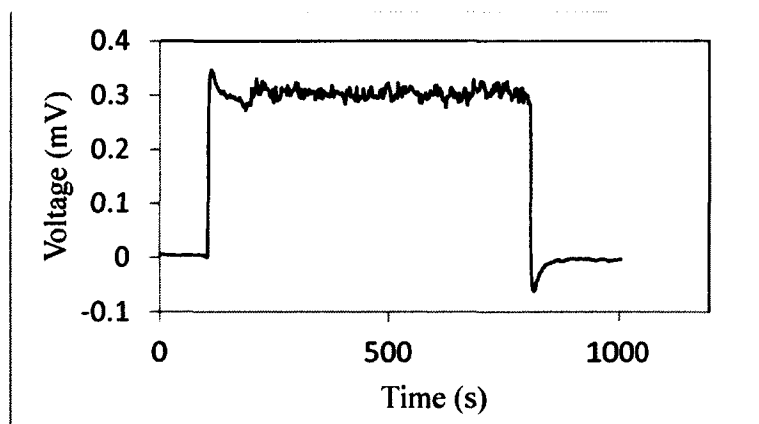
Figure 7-6 Voltage generation from thermoelectric effect (a) irradiation on the anchor region; (b) irradiation on the bottom electrode pad region.

The thermoelectric potential is essentially generated from the Seebeck effect as discussed in Chapter One.

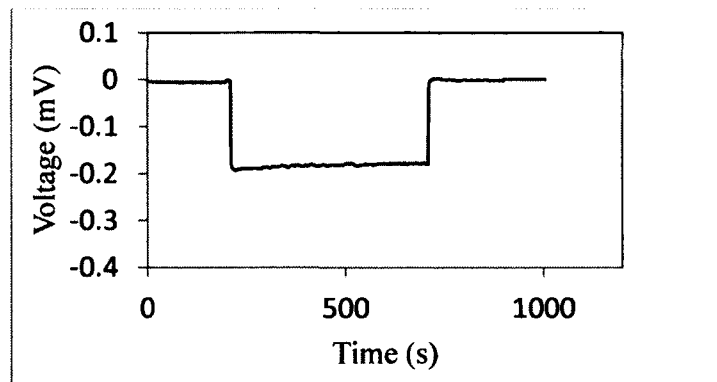
The voltage generated can be estimated from the equation below:

$$\Delta V_{AB} = \Delta V_A - \Delta V_B = (S_A - S_B)(T_{hot} - T_{cold}) = \Delta S_{AB} \times \Delta T, \quad (7-2)$$

where,  $V$  stands for the voltage,  $S$  for the Seebeck coefficient,  $T$  for the temperature, and  $\Delta$  for the difference. The Seebeck coefficient for Pt is  $S_{Pt} = 5.28 \mu\text{V/K}$  [13]. For silicon, the Seebeck coefficient varies with the doping level. For the p-type Si doped with boron at a concentration in the range of  $3 \times 10^{18}$  to  $2 \times 10^{19} \text{ cm}^{-3}$ ,  $S_{Si}$  is estimated to be  $300 \mu\text{V/K}$  which is significantly larger than  $S_{Pt}$  [98]. The temperature difference  $\Delta T$  is about 20K between room temperature and the spot of the focused lamp. From equation 7-2, it turns out that the voltage generation is about 5.9 mV. However, the practical amplitude of the voltage is about 0.3 mV, as shown in Figure 7-7. The reason is, in reality, that the temperature difference is not as high as 20 K since region “1” and region “2” are close to each other. Si and Pt can conduct heat between the two ends very quickly which reduces the temperature difference. In addition, a control experiment is done as in Figure 7-8.



(a)



(b)

Figure 7-7 OCV output when the irradiation is on (a) anchor region; (b) bottom electrode pad region.

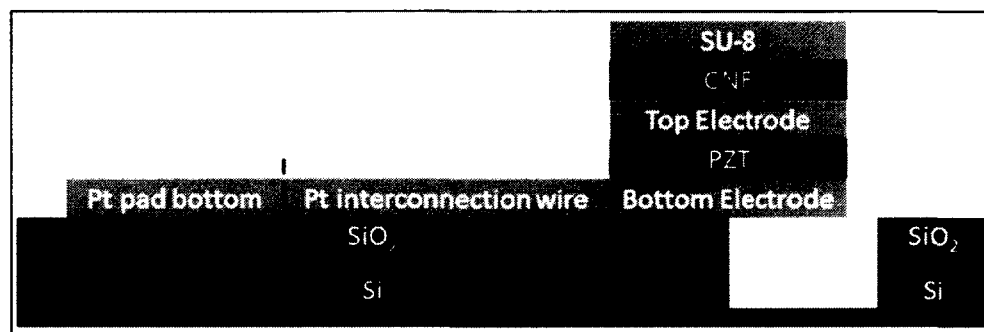


Figure 7-8 Equivalent structure sketch of the micro-energy harvesting device fabricated on an oxidized Si wafer.

In order to confirm the DC shift effect is a result of the thermoelectric effect, a control experiment was conducted with a device fabricated on an oxidized Si wafer. This design introduces a layer of 100 nm thick silicon dioxide, grown by dry oxidation, in between the Pt and Si and eliminates the formation of the heat junction. The equivalent structure sketch for the control experiment design is illustrated in Figure 7-8. The testing result for irradiating light and thermal energy to the anchor region is illustrated in Figure

7-9 with the same experimental conditions, as in Figure 7-7. As expected, there was no observed DC shift of the OCV. A micrograph of the device is shown in Figure 7-10.

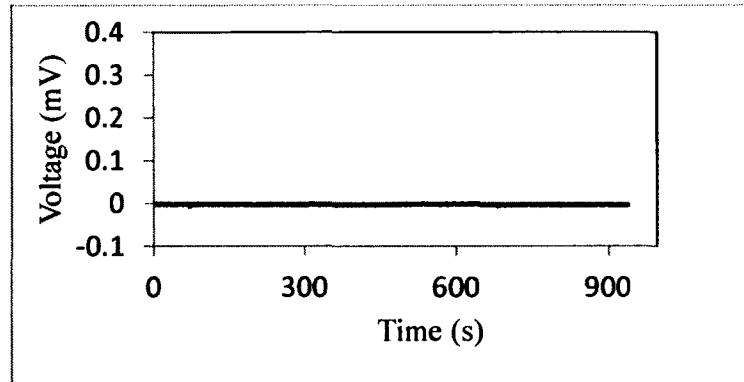


Figure 7-9 OCV output when the irradiation is on the anchor region with the device fabricated on oxidized wafer.

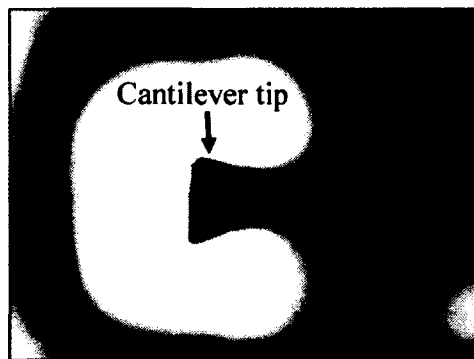


Figure 7-10 Cantilever curled up after release with thermal  $\text{SiO}_2$  as the bottom layer.

However, the oscillation part also disappears. From the micrograph of the device in Figure 7-10, an extremely large deformation of the released cantilever appears which comes from the non-uniform residual stress as discussed before. Compare to the image in Figure 5-11, the huge residual stress curls the cantilever almost 90 degrees up. It is caused by the compressive stress in the thermally grown  $\text{SiO}_2$  layer at the bottom and

tensile stress in PZT layer at the top [42]. The AC part is eliminated since the large residual stress presented in the cantilever impedes the oscillation from self-reciprocation.

## 7.2 Further Study of Micro-scale Energy Harvesting Device

### 7.2.1 Energy Generation under Different Radiation Conditions

Experiments were conducted to study the performance of the micro-energy harvesting device with different light and thermal energy from the Olympus TL-2 lamp. During the testing, the Olympus TL-2 lamp was tuned to four different conditions which are listed in Table 7-1. For each condition, the output of open circuit voltage (OCV) and short circuit current (SCC) were recorded. The electrical characteristics, such as average amplitude of oscillation (AC component) and shift (DC component), were extracted and analyzed independently. The device has a  $100\mu\text{m} \times 50\mu\text{m}$  cantilever and the anchor dimension is  $500\mu\text{m} \times 500\mu\text{m}$ . The results are summarized in Table 7-2.

Table 7-1 Four conditions for micro-device testing

Condition	Light Intensity ( $\text{W}/\text{cm}^2$ at 780 nm)	Temperature Difference (K)
1	$0.018 \pm 0.002$	$13.5 \pm 1$
2	$0.038 \pm 0.002$	$20.2 \pm 1$
3	$0.063 \pm 0.002$	$26.0 \pm 1$
4	$0.084 \pm 0.002$	$34.3 \pm 1$

For the DC component, the relationship between electrical output (OCV or SCC) and radiation input (light intensity or temperature difference) is almost linear, as

illustrated in Figure 7-11 (a) (c) and Figure 7-12 (a) (c). However, for the AC component, the relationship between electrical output and radiation input is presented close to a parabolic relationship, as plotted in Figure 7-11 (b) (d) and Figure 7-12 (b) (d). As an example, the mathematical model for the data in Figure 7-11 (a) and (b) was analyzed in statistics software SAS JMP by the least square regression method and plotted in Figure 7-13.

In Figure 7-13 (a), a linear fit model is used, whereas in Figure 7-13 (b), a two degree polynomial fit model is selected. The linear fit line in figure 7-13 (a) is expressed as:

$$V = 0.0593152 + 8.6784901 \times I, \quad (7-3)$$

The parabolic relationship in Figure 7-13 (b) is fitted as:

$$V = -0.0138 + 0.5765 \times I + 13.145 \times (I - 0.0508)^2, \quad (7-4)$$

where  $V$  stands for voltage in mV and  $I$  stands for light intensity in  $\text{W}/\text{cm}^2$  at 780 nm.

Table 7-2 Electrical characteristics for different light and thermal conditions

Condition	OCV		SCC	
	DC (mV)	AC(mV)	DC ( $\mu\text{A}$ )	AC ( $\mu\text{A}$ )
1	0.22	0.01	1.32	0.05
2	0.38	0.012	2.95	0.05
3	0.61	0.023	4.75	0.1
4	0.79	0.05	5.6	0.15

The first order polynomial surface fitting by MATLAB in a line and curve fitting tool for the DC component of OCV is also demonstrated in Figure 7-14.

The fitting equation is:

$$OCVDC(I, T) = 0.0899 + 9.917 \times I - 0.004 \times T, \quad (7-5)$$

Where, OCVDC is the DC component of OCV,  $I$  is the light intensity in  $W/cm^2$  at 780 nm, and  $T$  is the temperature difference. The R-square value for this fitting is 0.9996.

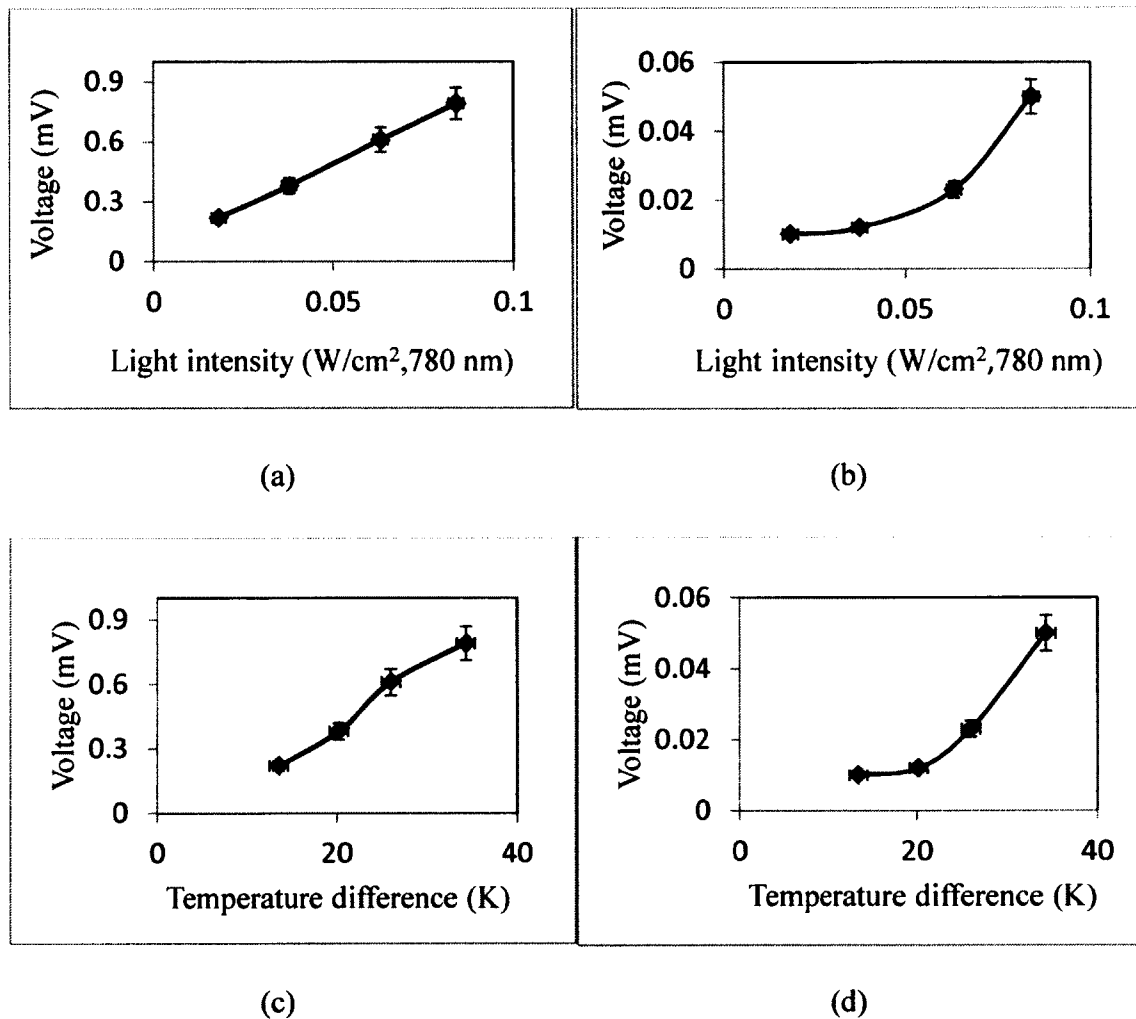


Figure 7-11 Relationship between (a) light intensity and the DC component of OCV; (b) light intensity and the AC component of OCV; (c) temperature difference and the DC component of OCV; (d) temperature difference and the AC component of OCV.



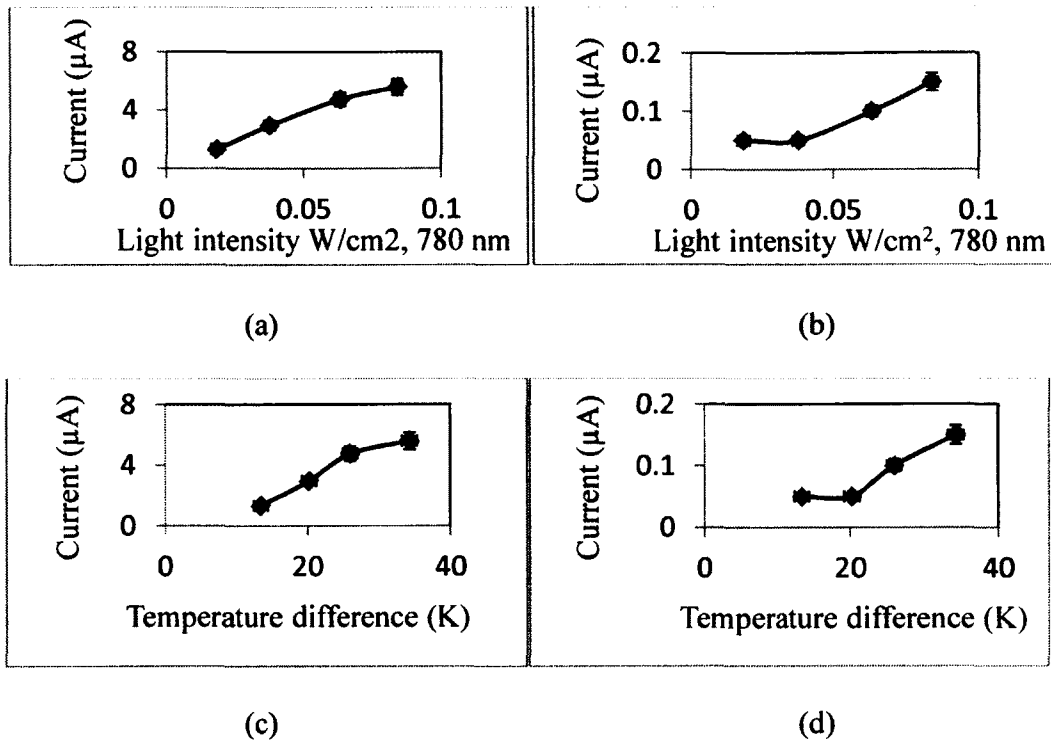


Figure 7-12 Relationship between (a) light intensity and the DC component of SCC; (b) light intensity and the AC component of SCC; (c) temperature difference and the DC component of SCC; (d) temperature difference and the AC component of SCC.

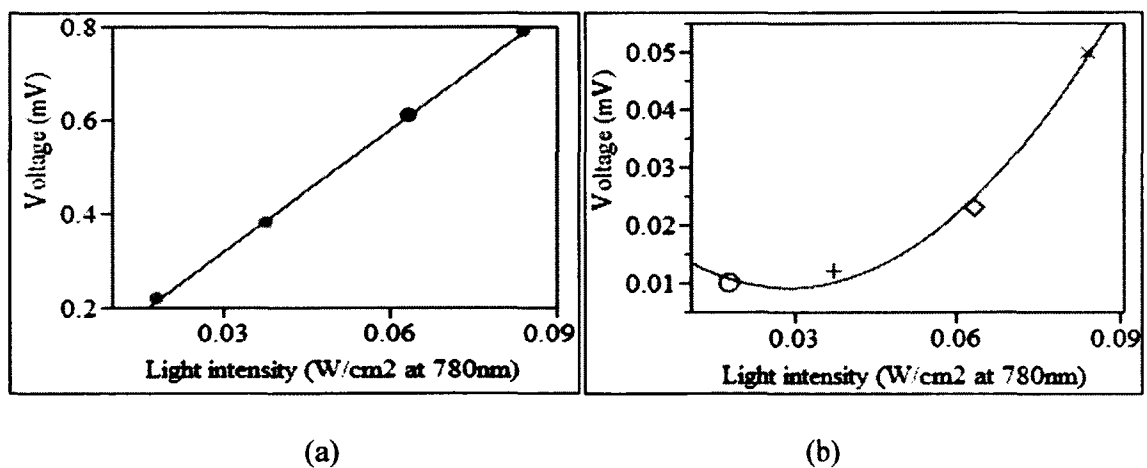


Figure 7-13 Least square fitting model: (a) linear fit of light intensity and DC component of OCV; (b) 2 degree polynomial fit of light intensity and AC component of OCV.

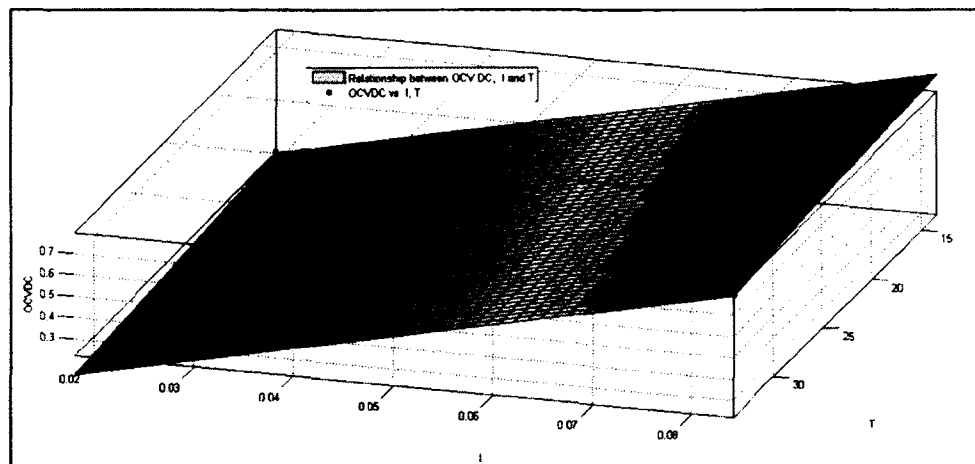


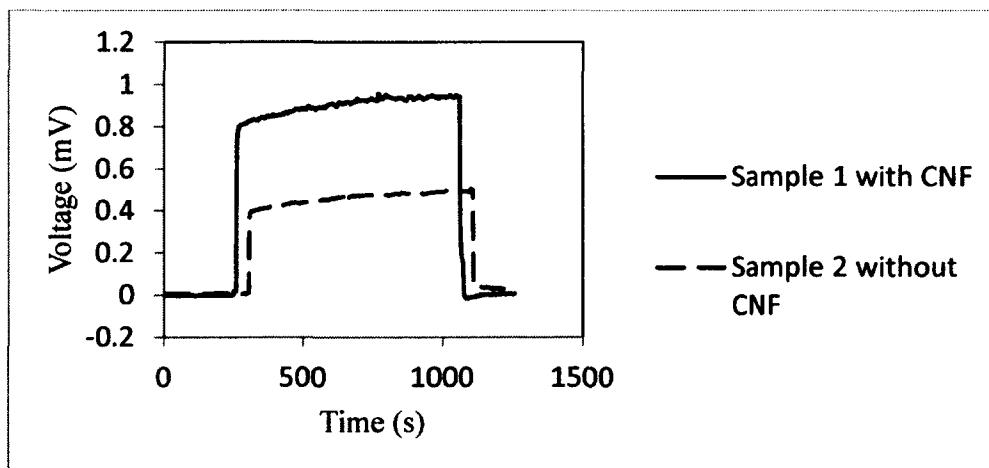
Figure 7-14 Example of surface fitting of DC component of OCV with light intensity and temperature difference using first order polynomial method.

### 7.2.2 Contribution of CNF and PZT

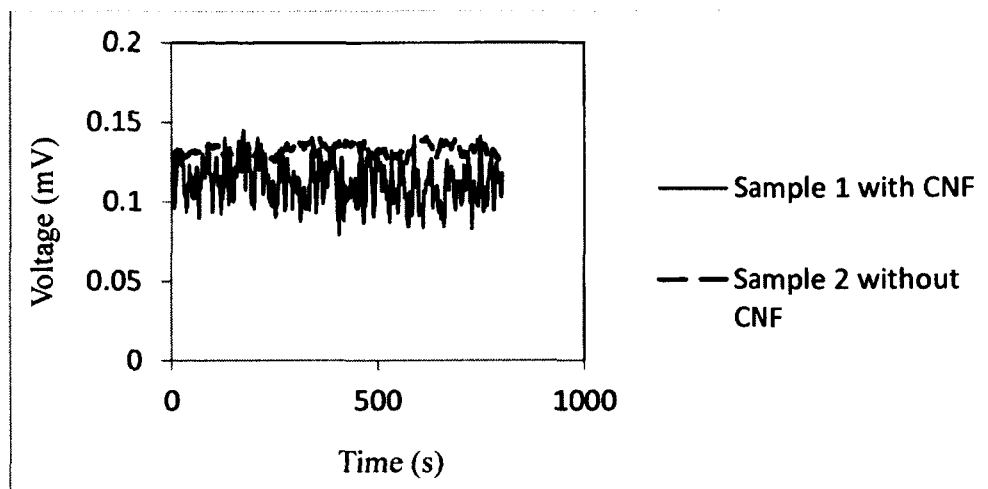
As stated in the previous chapter, the optical property of CNF shows the black body effect, which means it is able to absorb light and thermal radiation in an efficient way. In order to examine the contribution of CNF to light and thermal energy harvesting in the micro energy harvesting device, a set of control experiments was designed and performed. Two samples, with identical dimensions (100  $\mu\text{m}$  by 50  $\mu\text{m}$ ), of the cantilever were tested under the same light and thermal conditions. Sample one has integrated CNF on the device while sample two did not have CNF attached. The first experiment was done when the devices were in close contact with the light and thermal source. In this case, due to the help of excellent radiation absorption efficiency of CNF, the DC voltage generated is higher from sample one.

The recorded open circuit voltage (OCV) is plotted in Figure 7-15 (a). Another experiment was done when the DC voltage was balanced by two lamps which were focused on the anchor region and the bottom electrode region separately. As was shown in Figure 7-7, DC voltage would generate in reversed polarity for the two lamps focused

at different locations. Since the two parts of the DC voltages cancel out each other, the combined effect is the DC shift largely reduced while the oscillation of OCV (AC component) remains. As illustrated in Figure 7-15 (b) the AC component is only dominated from sample 1 with CNF. This control experiment once again indicates the importance of the CNF to the self-reciprocation phenomenon and the power generation. In addition, the PZT layer in the composite cantilever proposes to contribute to the oscillation of the electrical output (AC component) by converting the mechanical vibration from the self-reciprocation to electricity. On the other hand, the DC shift is mainly from the heat junction between Pt and Si but not from PZT. In order to confirm this mechanism, another set of control experiments were conducted. A batch of devices (Sample 3) was fabricated with a layer of PECVD silicon nitride instead of sol-gel PZT.



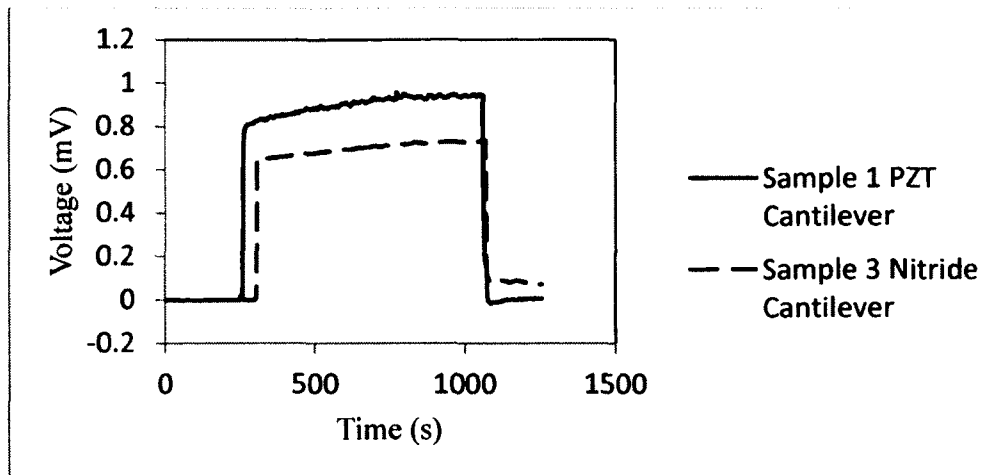
(a)



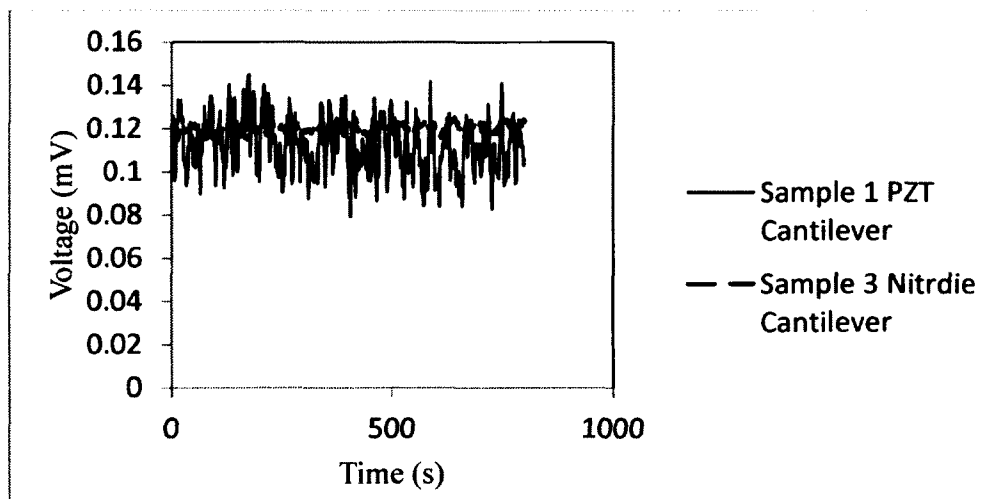
(b)

Figure 7-15 Control experiments to examine the contribution of CNF (a) Maximum DC shift; (b) AC oscillation.

All the other configurations are the same. The PECVD  $\text{Si}_3\text{N}_4$  was etched in an RIE system ( $\text{CF}_4$  40 SCCM,  $\text{O}_2$  10 SCCM, Pressure 375 mTorr, RF Power 300 W). The etching rate for  $\text{Si}_3\text{N}_4$  is about 40 nm per minute. Other fabrication steps are identical to the PZT based device. The OCV of sample 3 was recorded. The same experiments for comparing sample 1 and sample 2 were conducted for sample 1 and sample 3. The results are illustrated in Figure 7-16. Sample 3, with a nitride cantilever, also generated a DC shift of the same range as sample 1 with the PZT cantilever. However, the oscillation voltage (AC component) is only clearly visible from sample 1. It concludes that the PZT layer only contributes to the voltage oscillation (AC component). The Pt-Si junction is the key component contributing to the DC shift.



(a)



(b)

Figure 7-16 Control experiments to examine the contribution of PZT (a) Maximum DC shift; (b) AC oscillation.

### 7.2.3 Performance in the Real Environment

Up to now, all the experiments which have been done were conducted in the laboratory environment under controlled light and thermal conditions. In order to learn the performance of the micro-device more practically, testing was done outside of the lab in the real environment in the afternoon. During the experiment, the sky was clear. The

ambient temperature was about 87 °F, and 108 °F under direct sun light. The solar intensity recorded by the optical power meter is 0.03 W/cm<sup>2</sup> at 780 nm and 0.33 W/cm<sup>2</sup> at 635 nm. The result is illustrated in Figure 7-14 as the solid line. In order to exclude the damping effect, the experiment was recorded for an hour. During the testing, the OCV output shows continuous oscillation about 0.1 mV (AC) and a 0.15 mV DC shift as well. The power density from the AC component alone is about 1 μW/cm<sup>2</sup>. If we consider both AC and DC output, the power density is 4 μW/cm<sup>2</sup>. No clear damping was observed during the one hour testing. The OCV was found to increase when there was a wind flowing through the device. Obviously, not only the solar energy (light and thermal radiation) gives rise to the energy generation, but also the natural air flow and air disturbance contribute. As described previously, the asymmetric design of the device layout with a smaller anchor region and a bigger bottom electrode pad area is the main reason for generating the stable DC shift. As a reference, the OCV output of the device was also taken inside the lab without any radiation or intentional air disturbance. As shown in Figure 7-17 with a dashed line, the indoor reading is relatively flat. Neither oscillation (AC) nor DC shift is observed.

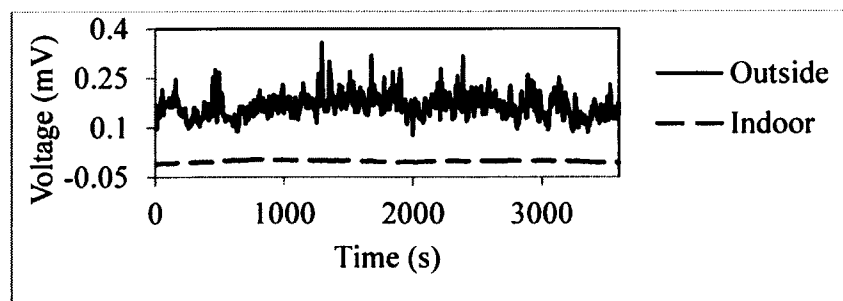


Figure 7-17 Open circuit voltage (OCV) recorded in outside environment (clear sky, temperature 87 °F, wind speed 5 mph, solar intensity 0.03 W/cm<sup>2</sup> at 780 nm and 0.33 W/cm<sup>2</sup> at 635 nm) presented in solid line; indoor environment testing without radiation energy presented in dashed line.

### 7.3 Summary

In this chapter, the electrical output characteristics of the micro-scale energy harvesting device were analyzed. The output is presented as a randomly distributed continuous oscillation (AC component) plus a shift (DC component). The AC component, which is similar to the macro-scale prototype device, was explained as being the effect from the unique self-reciprocation phenomenon described in Chapters Three and Four. The DC shift of the output was analyzed based on the equivalent structure illustrated in Figure 7-2. The photovoltaic effect was ruled out. The thermoelectric effect was found to contribute to the DC shift. A control experiment was completed with a device fabricated on an oxidized silicon wafer to confirm the role of the thermoelectric effect and no voltage generation was observed. The output performance of the micro device was further studied with different light intensities and thermal energies. The DC component was found to increase linearly with higher light intensity or thermal energy (temperature difference). On the other hand, the relationship between the AC component and light intensity or thermal energy is represented as a parabola. The mathematical models were established using the least square regression method in JMP and found that the R-square value (fitting accuracy) is greater than 99%. A surface fitting for the light intensity, temperature difference and DC component of OCV was also demonstrated using first degree of polynomial in MATLAB. The device was moved to the outside environment from the laboratory environment. The one hour open circuit voltage recording shows that the device can successfully generate power (oscillation and shift) from solar energy and wind energy continuously.

## CHAPTER EIGHT

### CONCLUSIONS AND FUTURE WORK

#### 8.1 Conclusions

In this dissertation, an innovative hybrid energy harvesting system based on a composite cantilever is designed, fabricated and analyzed. Other than the traditional methods for harvesting vibration energy from external sources [81], the device is capable of generating power from light and thermal energy as well.

First, renewable energy harvesting was introduced. Four major energy harvesting mechanisms including electromagnetic induction, thermoelectric effect, photovoltaic, and piezoelectric effect were examined. A detailed literature review was conducted to review the history of various energy harvesting mechanisms, related devices, and the current state of technology in those fields. Hybrid energy harvesting technology, using multiple energy harvesting mechanisms, were discussed as well. The problems of existing energy harvesting technology were pointed out.

As a novel type of nano material with known excellent properties and great potential, carbon nanotubes (CNTs) have caught attention and a large amount of effort has been put into research and development of the science and technology related to it. The basic properties of CNTs, such as crystal structure, mechanical, electrical, thermal and optical properties have been reviewed. The network of CNTs form a unique nano



material which is named carbon nanotube film (CNF). The synthesis of CNF using the vacuum filtration method has been described. By studying the optical and photovoltaic properties of a CNF, it turns out that CNF has excellent light absorption capability, which is close to a black body. Furthermore, the open circuit voltage (OCV) and the short circuit current (SCC) output of the CNF were observed to fluctuate when it received radiation energy (light and heat). Traditionally, a piezoelectric based cantilever for energy harvesting needs cyclic bending from an external vibration source or mechanical energy to operate. The idea was created from the fluctuation of the OCV or SCC of the CNF output which combines CNF with a cantilever to generate power from self-reciprocation upon receiving light and thermal radiation.

This idea was first tested with a composite cantilever, which has a copper shim base bonded with a layer of CNF above using double-sided tape. As expected, displacement of the cantilever tip was detected when exposed to light and thermal energy. In contrast, a single copper cantilever or a copper cantilever with double-sided tape attached did not show any significant oscillation upon exposure to the same radiation source. Eight sets of samples with different combinations of copper and CNF thickness were tested for the self-reciprocation phenomenon. By analyzing the results, a few conclusions can be drawn. First, with a fixed thickness of copper, oscillation amplitude for different samples with different thickness of CNF does not follow the traditional mechanical trend. There is an optimum thickness of CNF for achieving the biggest amplitude. Second, with a fixed thickness of CNF, a thicker copper base results in lower amplitude of oscillation. Third, stronger radiation (higher light intensity or larger temperature difference) will give higher amplitude of oscillation. The data was also

studied by Fourier analysis. The oscillation frequency of self-reciprocation is mainly below 0.1 Hz which is a low frequency oscillation. The natural resonant frequencies of those samples were found to be around 200 Hz in ANSYS which excludes that the self-reciprocation stems from natural resonance. The proposed mechanism of self-reciprocation may result from several reasons, such as different thermal expansion coefficient induced thermal actuation; non-uniform electrostatic field distribution; and others related to optical, thermal, electrical, elastic and mechanical properties of the CNF and the cantilever structure. The detailed analysis was presented in Section 3.4.

After the self-reciprocation phenomenon of a CNF based cantilever has been confirmed, a PZT cantilever (20 mm in length, 8 mm in width and 300  $\mu\text{m}$  in thickness) with top and bottom electrodes was attached to a strip of CNF to form a prototype macro-scale CNF-PZT based energy harvesting device. The oscillation of the cantilever from self-reciprocation was again observed. The open circuit voltage (OCV) and power generation capability has been evaluated. The OCV generated from the device, when exposed to an incandescent lamp and sun simulator, also shows significant oscillation as continuous deflection of the PZT layer from self-reciprocation. The maximum power output of a single prototype device from an optimal case is 2.1  $\mu\text{W}$ . However, the prototype macro-scale device has the disadvantage because of the thick PZT layer (300  $\mu\text{m}$ ). The extremely high internal resistance (80  $\text{M}\Omega$ ) is attributed to the thickness of the PZT layer which results in a low short circuit current output (smaller than 0.1  $\mu\text{A}$ ) and, therefore, a lower efficiency. This disadvantage largely limits its applications, such as charging the battery which is essential for the energy harvesting system.

In order to reduce the internal resistance and improve the efficiency, a micro-scale composite cantilever device was proposed based on a thinner layer of PZT. The dimension of the micro-scale cantilevers was designed in the range of 10  $\mu\text{m}$  to 30  $\mu\text{m}$  in width and 100  $\mu\text{m}$  to 350  $\mu\text{m}$  in length. The thickness of the PZT was designed to be 300nm. The layout of the device was designed in Tanner L-Edit. Seven masks were designed to pattern the multiple layers of the device. The fabrication development of the micro devices then followed the design using conventional surface and bulk micro-fabrication techniques. The detailed fabrication process flow is illustrated in Figure 5-4. The bottom and top electrodes were deposited by sputtering Pt and patterned by a bi-layer lift-off process which leads to a high yield. The PZT layers were deposited by a sol-gel method and annealed at high temperature to form the perovskite crystal structure. A reactive ion etching (RIE) process was developed to pattern the PZT. The carbon nanotube film (CNF) was synthesized using the vacuum filtration method and was transferred to the device by the compression loading approach. A layer of SU-8 negative photoresist was defined above the CNF as a protection mask for etching CNF in the ICP RIE system using oxygen plasma. Part of the transparent SU-8 was left as a part of the composite cantilever to enhance the robustness of the cantilever. The cantilever was finally released in an  $\text{XeF}_2$  chemical dry etching system through the etching window.

The fabricated devices were polarized in a strong electrical field, and the temperature was raised in order to improve the piezoelectric coefficient. The validation of the device has been done through a DC actuation method. A DC voltage was applied to a single device. The response of the cantilever tip displacement validated a working device. The initial testing was performed on a probe station with micro manipulators connected

to both electrodes. Light and thermal energy harvesting was demonstrated by exposing the device to an Olympus TL-2 lamp and/or hotplate. The open circuit voltage (OCV) output pattern matches the OCV output from the macro-scale prototype device which showed significant vibration. The short circuit current (SCC) recorded was also observed with the oscillation. Besides the oscillation (AC) output, a unique phenomenon was found in which all of the electrical output from the micro scale device had a DC shift added to the oscillation. Calculated from the maximum power transfer theorem, in terms of the oscillation power output, the power density  $\mu$  (power generated per unit area) of a micro-scale device is 4445 times greater when compared to a macro-scale device.

The DC shift of the electrical output from the micro-scale device was analyzed in details from a newly designed device. An equivalent structure sketch of the micro-energy harvesting device was designed to study the influence from several energy harvesting mechanisms. Based on the material properties and photovoltaic theory, the Schottky junction solar cell on the device structure was excluded. The thermoelectric effect (Seebeck effect) was testified to have significant influence on the DC shift generation. A different polarity of the OCV output was observed when the radiation was focused on the two opposite heat junctions. A control experiment was completed with the device fabricated on an oxidized silicon substrate which eliminates the heat junction. No DC shift was observed from the testing, which further confirmed that the reason for the DC generation is from the thermoelectric effect.

The micro-device performance under different light and thermal radiation was tested. Generally, both the amplitude of the oscillation (AC) and the shift (DC) for open circuit voltage (OCV) and short circuit current (SCC) rise with the increasing light

intensity and temperature. A least square regression method was used to fit OCV output (AC and DC) by radiation input (light intensity and temperature difference). It was found that the DC output increased almost linearly with radiation input, while AC output increased parabolically with radiation input.

The micro energy harvesting device was taken outdoors to conduct a testing for harvesting energy under real world conditions. The OCV from a single device was recorded and showed the continuous energy generation from both solar and wind.

One of the major contributions of this dissertation is the discovery and the analysis of the self-reciprocation phenomenon for a composite cantilever. This is advantageous for the cantilever based energy harvesting system which traditionally needs an external mechanical vibration source in a certain frequency range to harvest energy; now it can operate as long as light and thermal radiation are present. Another contribution of this research is the development of the fabrication process for the first generation micro-energy harvesting device, which integrated carbon nanotube film (CNF) with a PZT cantilever in order to enhance energy harvesting from the self-reciprocation phenomenon. In addition, the performance of the micro energy harvesting device was studied in detail. The ability to harvest energy from the thermoelectric effect and self-reciprocation makes the device a hybrid energy harvesting system. Furthermore, the feasibility of reclaiming energy outside of the controlled laboratory environment has been demonstrated.

## 8.2 Future Work

### 8.2.1 Improvement of Fabrication Processes

The fabrication process for the micro device has been successfully developed and demonstrated in this dissertation. However, there are a few considerations for further improvement.

Firstly, the PZT annealing process is very time consuming. One layer of PZT needs a whole day to process since the conventional annealing process takes overnight. A 3-layer PZT film plus a seed layer needs 4 days to process. With a rapid thermal annealing (RTA) process, it will only take a day to finish annealing for all the steps mentioned above, which largely reduces the process time. The RTA process also exhibits advantages for improving the properties of PZT over the conventional annealing process. First, it shortens the time for high temperature annealing which reduces the inter-diffusion between bottom electrode Pt atoms and PZT. Second, the shorter time for the high temperature process will reduce the time-temperature product pyrochlore phase, which is not a desired phase in PZT, since it will hamper the piezoelectric coefficient. Meanwhile, the perovskite phase formation will be enhanced by RTA. Third, the multiple parameters of RTA, such as heating rate, hold time, and cooling rate can be adjusted to match the desired characteristics for the applications [99, 100]. A further study needs to be conducted to optimize the piezoelectric properties of PZT.

Secondly, as shown in the micro graphs of the cantilever in Figures 5-11, 5-13, and 7-10, the micro composite cantilever structures were curled due to the residual stress. The residual stress presented to the micro device, introduced during the fabrication, resists the self-reciprocation of the cantilever and lowers the efficiency. The bent

cantilever has less area of CNF facing the incident radiation, so less heat will be converted. Additionally, to generate significant oscillation of the cantilever, it must first overcome the internal residual stress. Thermal annealing is a possible way to relax the residual stress. Another approach to optimize the residual stress and mechanical property of the cantilever is to carefully adjust the residual stress for each layer (i.e. different fabrication method, choosing of material, or deposit additional layers) to compensate the residual stress. An example of utilizing this approach to relax an initially curled cantilever is shown in Figure 8-1[42].

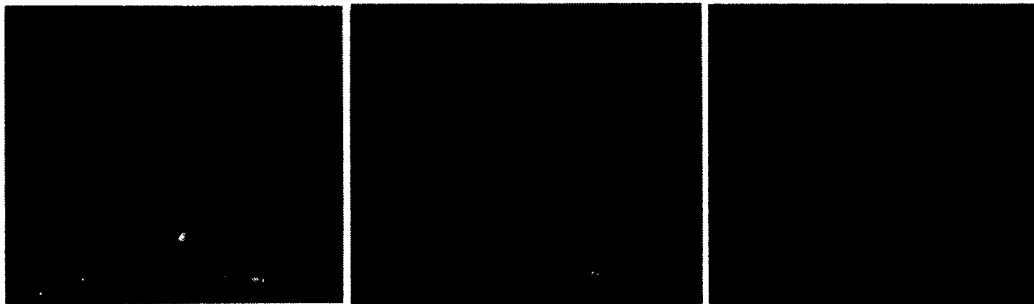


Figure 8-1 Relaxing of a composite micro cantilever by replacing thermal oxide layer with PECVD oxide and add PECVD SiN<sub>x</sub> layer [42].

Some other considerations for the fabrication improvement are listed below:

- (a) Improve the CNF transfer method on the non-flat substrate, such as a printing technique, other than compression loading;
- (b) Improve the etching rate and selectivity for patterning CNF using an SU-8 mask;
- (c) Develop dicing and packaging for the micro device.

### 8.2.2 Power Output Enhancement

Firstly, the power output enhancement might be achieved by integrated nanostructures. As stated in Chapter One, the efficiency of p-n junction based traditional

solar cell has a limitation of 33.7%, assuming a band gap of 1.1 eV, which is called the Shockley-Queisser limit or detailed balance limit [26]. The third generation solar cells, including a group of newly developed concepts, are mainly centered on nano technologies which are aimed to exceed this limit. One research direction is focusing on integrating nanostructures, such as nanoparticles, nanowires, nanoantennas, and sub-wavelength grooves which can introduce the surface plasmon excitation to enhance the absorption of light energy [101-104]. The surface plasmon excitation will introduce high frequency evanescent wave transport along the surface of the nanostructure which, in turn, results in non-uniform distribution of the static charge, and the dissipation of the evanescent wave converts to heat. Some researchers have demonstrated that an aqueous solution containing CuS nanoparticles has increased temperature compared to the same volume of pure water when exposed to a laser beam [105]. The non-uniform distribution of the static charge and heat are essential for the self-reciprocation of the composite cantilever structure, which accounts for the oscillation output (AC), while the thermoelectric effect accounts for the DC output.

Secondly, as illustrated in Section 7.2.1, a higher light intensity and/or temperature leads to the increase in open circuit voltage and short circuit current. Integration of an optical condenser with the micro-scale energy harvesting device to gather more light and thermal energy per unit area is a straight forward way to enhance the power output. The optical condenser is a lens that serves to concentrate radiation over a certain range of wavelengths and focus onto a small area. The maximum energy is concentrated at the focal plane of the condenser [19]. The traditional solar cell has adopted this idea to develop the concentrator photovoltaic system (CPV) which provides a way to increase



overall efficiency and achieve lower cost by increasing the photon flux and decreasing the cost per unit of energy converted [19, 106]. A sketch of the proposed micro-lens enhanced micro energy harvesting system is illustrated in figure 8-2. An experiment has also been completed to prove the feasibility of this method. A handhold magnifier was used to focus the sun light.

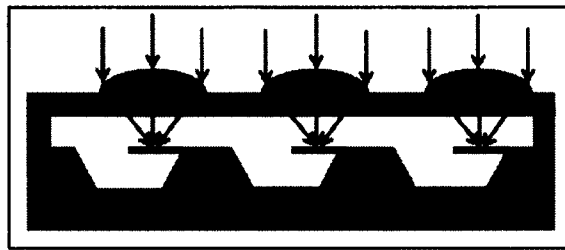


Figure 8-2 Sketch of the micro-lens integrated micro-energy harvesting system.

Figure 8-3 shows the OCV output increased significantly when the focused light spot is scanned across the anchor region of the device. The power density is  $324 \mu\text{W}/\text{cm}^2$ , which has been increased 81 times compared to the result without a lens for power enhancement.

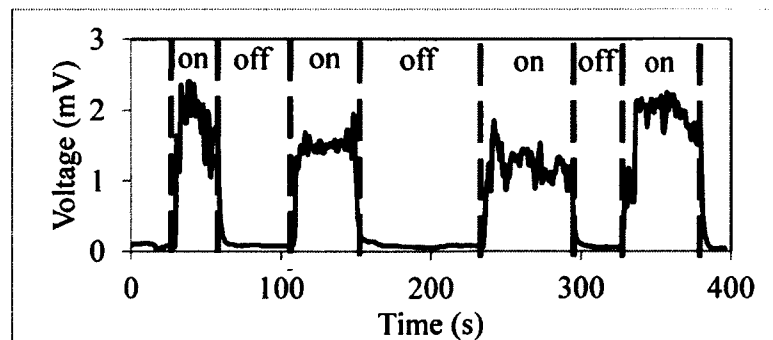


Figure 8-3 OCV output when a focused sun light spot scans across the device. “On” stands for focused light spot on the device; “off” stands for device off focus.

Thirdly, as a conventional approach for the solar cell, the open circuit voltage and short circuit current can be increased by connecting the device in series and in parallel respectively[19]. This idea can also be applied to the micro energy harvesting device to increase the power output by operating arrayed devices. Two micro devices have been connected in series, as shown in Figure 8-4, to demonstrate the possibility of increasing OCV. The recorded OCV output is plotted in Figure 8-5. The maximum OCV output of DC bias (DC output), which is more than 2 mV, has been obviously doubled as compared to a single device. However, the oscillation amplitude (AC output) of the OCV is not doubled. A new approach needs to be found for the synchronization of AC output for arrayed devices.

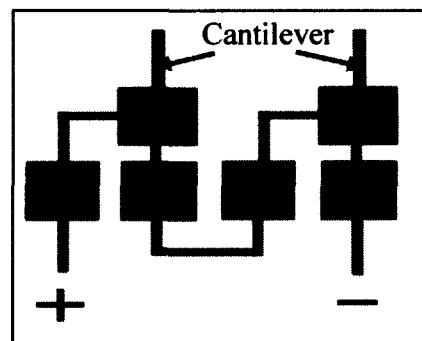
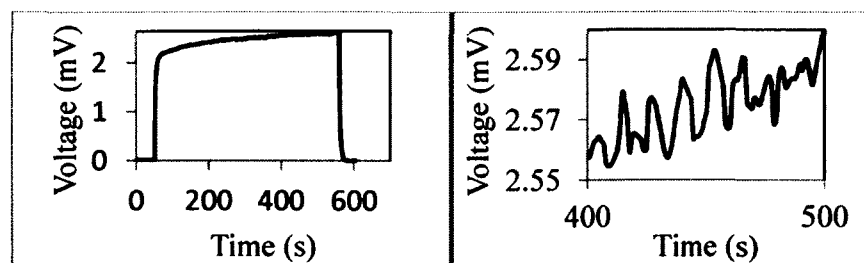


Figure 8-4 Tandem device layout for increasing the OCV output.



(a)

(b)

Figure 8-5 (a) OCV output of a tandem device; (b) close-up view of the AC output.

This is expected since the cantilever of an individual device is operated separately. Some other potential future work involves the investigation of the fundamental physics and modeling for the self-reciprocation phenomenon. The understanding of fundamental physics will help improve the design of the device. To optimize the mechanical properties of the micro cantilever, modeling of the micro cantilever using the finite element method for evaluating different dimension combinations and different materials are needed.

## APPENDIX A

### MATLAB CODE FOR FAST FOURIER TRANSFORM

```
% FFT for Cu-CNF Laser Vibrometer Data by Zhongcheng Gong
```

```
% Time-Domain
```

```
fs=256;           % Sampling frequency of the equipment Hz
```

```
tt=128;          % Total Time (s)
```

```
%t=Sheet1(:,1); % Time
```

```
t=[0:1/fs:fs*tt/fs];
```

```
t=t(1:fs*tt);
```

```
x=Sheet1(:,2);   % Displacement
```

```
%x=1*cos(2*pi*50*t)+1*cos(2*pi*75*t); % Sin wave sample
```

```
plot(t,x)        % Display Time-Domain Signal
```

```
figure;
```

```
% Frequency-Domain
```

```
m=length(x);     % Number of time-domain Sample points
```

```
n=pow2(nextpow2(m)); % Optimal Frequency domain length
```

```
z=1;             % Optimize factor
```

```
y=fft(x,z*n);    % Calculate z*n points DFT of displacement
```

```
f = (0:z*n-1)*(fs/(z*n)); % Frequency range after FFT
```

```
%power = y.*conj(y); % Power of the DFT
```

```
modulus = abs (y);
```

```
lof=length(f);   % Number of frequency-domain points
```

```
%plot(f(1:128*z),power(1:128*z),'o')
```

```
plot(f,modulus)           % Plot the whole frequency domain
xlabel('Frequency (Hz)')
ylabel('FFT Modulus')
title('Periodogram')
a=f(1:128*z);
a=a(:);                   % Row vector to column vector
b=modulus(1:128*z);
dataM=[a,b];             % Frequency data 0-1Hz (frequency, Modulus of FFT complex number)
% Convert y to real amplitude
figure;
Amplitude=modulus/(m/2);
Amplitude(1)=modulus(1)/m;
plot(f(1:1*128),Amplitude(1:1*128));
xlabel('Frequency (Hz)')
ylabel('Displacement(m)')
title('FFT signal with real amplitude');
dataA=[a, Amplitude(1:128*z)]; % Frequency data 0-1Hz (frequency, Real amplitude of
this frequency)
```

## REFERENCES

- [1] J. Brugger, "Nanotechnology impact on sensors," *Nanotechnology*, vol. 20, pp. 1-2, Oct. 2009.
- [2] S. Lu and B. Panchapakesan, "Nanotube micro-optomechanical actuators," *Appl. Phys. Lett.*, vol. 88, pp. 253107, Jun. 2006.
- [3] K. Lux and K. Rodriguez, "Template synthesis of arrays of nano fuel cells," *ACS Nano. Lett.*, vol. 6, pp. 288-295, Feb. 2006.
- [4] E. Serrano, G. Rus, J. Garcia-Martinez, "Nanotechnology for sustainable energy," *Renew. Sust. Energy. Rev.*, vol. 13, pp. 2373-2384, Jun. 2009.
- [5] P. G. Jones, S. P. Beeby and N. M. White, "Towards a piezoelectric vibration-powered microgenerator," *IEEE Proc-A.*, vol. 148, pp. 68-72, Mar. 2001.
- [6] J. A. Turner, "A realizable renewable energy future," *Science*, vol. 285, pp. 687-689, Jul. 1999.
- [7] C. Mitchell, P. Connor, "Renewable energy policy in the UK 1990 - 2003," *Energy Policy*, vol. 32, pp. 1935-1947, May 2004.
- [8] N. Haluzan, (2011, March 14). *Renewable energy sources list*, [Online]. Available: [http://www.renewables-info.com/renewable\\_energy/renewable\\_energy\\_sources\\_list.html](http://www.renewables-info.com/renewable_energy/renewable_energy_sources_list.html).
- [9] L. Mateu and F. Moll, "Review of energy harvesting techniques and applications for microelectronics," in *Proc. SPIE Microtechnologies for the New Millennium*, 2005, pp. 359-373.
- [10] P. Quinlan and R. Crowley, "2010 North Carolina renewable energy & energy efficiency industries census," *NC Sustainable Energy Association*, NC, 2010, pp. 11.
- [11] R. L. Myers, *The Basics of Physics*, Greenwood Press: Westport, Conn, 2006.
- [12] T. Massimo, "The contribution of Francesco Zantedeschi at the development of the experimental laboratory of physics faculty of the Padua University," in *Istituto di Fisica Generale Applicata Università degli Studi di Milano*, 2012, pp. 301-312.

- [13] S. O. Kasap, *Principles of Electronic Materials and Devices: 3<sup>rd</sup> edition*, McGraw-Hill Companies, 2005.
- [14] G. S. Nolas, J. Sharp and H. J. Goldsmid, *Thermoelectrics: Basic Principles and New Materials Developments*, Springer, 2001.
- [15] D. Rowe, *Handbook of Thermoelectrics*, CRC Press, 1995.
- [16] B. C. Sales, "Critical overview of recent approaches to improved thermoelectric materials," *Int. J. Appl. Ceram. Tech.*, vol. 4, pp. 291-296, Jul. 2007.
- [17] D. M. Rowe, *General Principles and Basic Considerations in: Thermoelectric Handbook - Macro to Nano*, Taylor & Francis Group, 2006.
- [18] O. Mah, "Fundamentals of photovoltaic materials," in *Nat. Solar Power Res. Inst.*, 1998, pp. 1-10.
- [19] J. Nelson, *The Physics of Solar Cells*, Imperial College Press, 2003.
- [20] H. Wicht, (2009, November 13). *Thin-film's share of solar panel market to double by 2013*, [Online]. Availbe: <http://www.renewableenergyworld.com/rea/news/article/2009/11/thin-films-share-of-solar-panel-market-to-double-by-2013>.
- [21] G. F. Brown and J. Wu, "Third generation photovoltaics," *Laser & Photonics Rev.*, vol. 3, pp. 394-405, Jan. 2009.
- [22] S. O. Kasap, *Principles of Electronic Materials and Devices: 3<sup>rd</sup> edition*, McGraw-Hill publishing, 2005.
- [23] T. Starner, "Human-powered wearable computing," *IBM Syst. J.*, vol. 36, pp. 618-629, Apr.1996.
- [24] G. Gautschi, *Piezoelectric Sensorics*, Springer-verlag, Berlin, Heidelberg, 2002.
- [25] E. Sawaguchi, G. Shirane and Y. Takagi, "Phase transition in lead zirconate," *J. Phys. Soc. Jpn.*, vol. 6, pp. 333-339, Feb. 1951.
- [26] W. Shockley and H. Queisser, "Detailed balance limit of efficiency of p-n junction solar cells," *J. Appl. Phys.*, vol. 32, pp. 510-519, Mar.1961.
- [27] A. Marti and A. Luque, *Next Generation Photovoltaics: High Efficiency Through Full Spectrum Utilization*, Taylor & Francis, 2003.
- [28] A. J. Nozik, "Quantum dot solar cells," *Physica E*, vol. 14, pp. 115-120, Apr. 2002.



- [29] R. T. Ross and A. J. Nozik, "Efficiency of hot-carrier solar energy converters," *J. Appl. Phys.*, vol. 53, pp. 3813-3818, May 1982.
- [30] T. Trupke, M. A. Green and P. Würfel, "Improving solar cell efficiencies by up-conversion of sub-band-gap light," *J. Appl. Phys.*, vol. 92, pp. 4117-4122, Oct. 2002.
- [31] C. Gould and N. Shamma, "A review of thermoelectric MEMS devices for micro-power generation, heating and cooling applications," *Microelectron. Mech. Syst.*, vol. 2, pp. 15-24, Dec. 2009.
- [32] S. B. Riffat and X. Ma, "Thermoelectrics: a review of present and potential applications," *Appl. Therm. Eng.*, vol. 23, pp. 913-935, Dec. 2002.
- [33] A. I. Hochbaum, R. Chen, R. D. Delgado, W. Liang, E. C. Garnett, M. Najarian, A. Majumdar and P. Yang, "Enhanced thermoelectric performance of rough silicon nanowires," *Nature*, vol. 451, pp. 163-167, Oct. 2007.
- [34] D. M. Rowe, "Review: Thermoelectric waste heat recovery as a renewable energy source," *Int. J. Inno. Energ. Syst. Power*, vol. 1, pp. 13-23, Nov. 2006.
- [35] X. Y. Yu, G. Chen, A. Verma and J. S. Smith, "Temperature dependence of thermophysical properties of GaAs/AlAs periodic structure," *Appl. Phys. Lett.*, vol. 67, pp. 3353-3357, Dec. 1995.
- [36] J. Cornett and O. Rabin, "Thermoelectric figure of merit calculations for nanowires - the moderate confinement regime," in *MRS Proc.*, 2010. pp. 1267-1269.
- [37] H. Glosch, M. Ashauer, U. Pferiffer and W. Lang, "A thermoelectric converter for energy supply," *Sensors Actuat. A-Phys.*, vol. 74, pp. 246-250, Apr. 1999.
- [38] I. H. Kim, "(Bi,Sb)<sub>2</sub>(Te,Se)<sub>3</sub>-based thin film thermoelectric generators," *Mater. Lett.*, vol. 43, pp. 221-224, Apr. 2000.
- [39] M. Umeda, K. Nakamura and S. Ueha, "Analysis of the transformation of mechanical impact energy to electric energy using piezoelectric vibrator," *Jpn. J. Appl. Phys.*, vol. 35, pp. 3267-3273, Jan. 1996.
- [40] M. Umeda, K. Nakamura and S. Ueha, "Energy storage characteristics of a piezo-generator using impact induced vibration," *Jpn. J. Appl. Phys.*, vol. 36, pp. 3146-3151, Feb. 1997.
- [41] J. Park, H. Park and S. Kang, "Fabrication and properties of PZT micro cantilevers using isotropic silicon dry etching process by XeF<sub>2</sub> gas for release process," *Sensors Actuat. A-Phys.*, vol. 117, pp. 1-7, May 2004.

- [42] Y. B. Jeon, R. Sood, J. H. Jeong and S. G. Kim, "MEMS power generator with transverse mode thin film PZT," *Sensors Actuat. A-Phys*, vol. 12, pp. 16-22, Feb. 2005.
- [43] H. Li, A. Lal, J. Blanchard and D. Henderson, "Self-reciprocating radioisotope-powered cantilever," *J. Appl. Phys.*, vol. 92, pp. 1122-1127, Mar. 2002.
- [44] C. Xu, X. Wang and Z. Wang, "Nanowire structured hybrid cell for concurrently scavenging solar and mechanical energies," *J. Am. Chem. Soc.*, vol. 131, pp. 5866-5872, Apr. 2009.
- [45] T. Suzuki, K. Yoshikawa and S. Momose, "Integration of organic photovoltaic and thermoelectric hybrid module for energy harvesting applications," in *Proc. IEEE Int. Electron Dev.*, 2010, pp. 3161- 3164.
- [46] S. Iijima, "Helical microtubules of graphitic carbon," *Nature*, vol. 354, pp. 56-58, Nov. 1991.
- [47] D. S. Bethune, C. H. Kiang, M. S. de Vries, G. Goman, R. Savoy, J. Vazquez and R. Beyers, "Cobalt-catalysed growth of carbon nanotubes with single-atomic-layer walls," *Nature*, vol. 363, pp. 605-607, Jun. 1993.
- [48] M. Endo, T. Hayashi, Y. Kim, M. Terrones and M. Dresselhaus, "Applications of carbon nanotubes in the twenty-first century," *Philosoph. Trans. Ro. Soc. A: Math., Phys. Eng. Sci.*, vol. 362, pp. 2223-2238, Mar. 2007.
- [49] R. H. Baughman, A. A. Zakhidov and W. A. Heer, "Carbon nanotubes – the route toward applications," *Science*, vol. 297, pp. 787-792, Aug. 2002.
- [50] D. S. Hecht, D. Thomas, L. Hu, C. Ladous, T. Lam, Y. Park, G. Irvin and P. Dizaic, "Carbon-nanotube film on plastic as transparent electrode for resistive touch screens," *J. Soc. Inform. Disp.*, vol. 17, pp. 941-946, Nov. 2009.
- [51] M. Zhang, S. Fang, A. A. Zakhidov, S. B. Lee, A. E. Aliev, C. D. Williams, K. R. Atkinson and R. H. Baughman, "Strong, transparent, multifunctional, carbon nanotube sheets," *Science*, vol. 309, pp. 1215-1219, Aug. 2005.
- [52] S. Lu and B. Panchapakesan, "Optically driven nanotube actuators," *Nanotechnology*, vol. 16, pp. 2548-2554, Nov. 2005.
- [53] M. E. Itkis, F. Borondics, A. Yu and R. C. Haddon, "Bolometric infrared photoresponse of suspended single-walled carbon nanotube films," *Science*, vol. 312, pp. 413-414, Apr. 2006.
- [54] P. Harris, "Carbon nanotube composites," *Int. Mater. Rev.*, vol. 41, pp. 31-43, Feb. 2004.

- [55] A. Lau and D. Hui, "The revolutionary creation of new advanced materials - Carbon nanotubes composites," *Compos. Part B-Eng.*, vol. 33, pp. 263-277, Apr. 2002.
- [56] B. Bharat, *Hand book of Nanotechnology*, Springer, 2004.
- [57] D. J. Lockwood, B. W. Smith and D. E. Luzzi, *Introduction to Nanoscale Science and Technology*, Springer, 2004.
- [58] S. Belluci, "Carbon nanotubes: physics and applications," *Phys. Status Solidi*, vol. 2, pp. 34-47, Jan. 2005.
- [59] M. Meo and M. Rossi, "Prediction of Young's modulus of single wall carbon nanotubes by molecular-mechanics based finite element modelling," *Compos. Scis Technol.*, vol. 66, pp. 1597-1605, Feb. 2006.
- [60] T. Dulrkoop, S. Getty, C. Enrique and M. Fuhrer, "Extraordinary mobility in semiconducting carbon nanotubes," *Nano Lett.*, vol. 4, pp. 35-39, Dec. 2003.
- [61] J. Che, T. Caqin and W. A. Goddard III, "Thermal conductivity of carbon nanotubes," *Nanotechnology*, vol. 11, pp. 65-69, Jun. 2000.
- [62] W. Michael and H. Jang-Yu, "Thermal conductivity of carbon nanotubes with quantum correction via heat capacity," *Nanotechnology*, vol. 20, pp. 1-6, Apr. 2009.
- [63] W. Zhang, Z. Zhu, F. Wang, T. Wang, L. Sun and Z. Wang, "Chirality dependence of the thermal conductivity of carbon nanotubes," *Nanotechnology*, vol. 15, pp. 936-939, Aug. 2004.
- [64] G. Etienne, I. Nicolas, V. Laurent, K. Said, M. Delphine and C. Eric, "Enhancement of semiconducting single-wall carbon nanotubes photoluminescence," *Opt. Lett.*, vol. 34, pp. 3845-3847, Dec. 2009.
- [65] H. Jin, K. Masakazu, S. Daisuke, M. Hiroyuki, C. Yong, H. Takuya, A. Yoong, E. Morinobu, S. Jin and S. Riichiro, "Raman and fluorescence spectroscopic studies of a DNA-dispersed double-walled carbon nanotube solution," *ACS Nano*, vol. 4, pp. 1060-1066, Jan. 2010.
- [66] S. Maruyama, E. Einarsson, Y. Murakami and T. Edamura, "Growth process of vertically aligned single-walled carbon nanotubes," *Chem. Phys. Lett.*, vol. 403, pp. 320-323, Jan. 2005.
- [67] H. Kataura, Y. Kumazuwa, Y. Maniwa, I. Umezu, S. Suzuki, Y. Ohtsuka and Y. Achiba, "Optical properties of single-wall carbon nanotubes," *Synthetic. Met.*, vol. 103, pp. 2555-2558, Mar. 2000.

- [68] M. Freitag, Y. Martin, J. A. Misewich, R. Martel and P. H. Avouris, "Photoconductivity of single carbon nanotubes," *Nano Lett.*, vol. 3, pp. 1067-1071, Jun. 2003.
- [69] J. U. Lee, "Photovoltaic effect in ideal carbon nanotube diodes," *Appl. Phys. Lett.*, vol. 87, pp. 073101, Aug. 2005.
- [70] K. Balasubramanian, M. Burghard, K. Kern, M. Scolari and A. Mews, "Photocurrent imaging of charge transport barriers in carbon nanotube devices," *Nano Lett.*, vol. 5, pp. 507-510, Feb. 2005.
- [71] M. Freitag, J. C. Tsang, A. Bol, D. Yuan, J. Liu and P. Avouris, "Imaging of the Schottky barriers and charge depletion in carbon nanotube transistors," *Nano Lett.*, vol. 7, pp. 2037-2042, Jun. 2007.
- [72] Z. Wu, Z. Chen, X. Du, J. M. Logan, J. Sippel, M. Nikolou, K. Kamaras, J. R. Reynolds, D. B. Tanner, A. F. Hebard and A. G. Rinzler, "Transparent, conductive carbon nanotube films," *Science*, vol. 305, pp. 1273-1276, Aug. 2004.
- [73] P. V. Kamat, "Harvesting photons with carbon nanotubes," *Nano Today*, vol. 1, pp. 20-27, Nov. 2006.
- [74] R. H. Baughman, C. Cui, A. A. Zakhidov, Z. Iqbal, J. N. Barisci, G. M. Spinks, G. G. Wallace, A. Mazzoldi, D. D. Rossi, A. G. Rinzler, O. Jaschinski, S. Roth and M. Kertesz, "Carbon nanotube actuators," *Science*, vol. 284, pp. 1340-1344, May 1999.
- [75] K. Mizuno, J. Ishii, H. Kishida, Y. Hayamizu, S. Yasuda, D. Futaba, M. Yumura and K. Hata, "A black body absorber from vertically aligned single-walled carbon nanotubes," *in Proc. Nat. Acade. Sci. USA*, 2009, pp. 6044-6051.
- [76] Y. Zhang and S. Iijima, "Elastic response of carbon nanotube bundles to visible light," *Phys. Rev. Lett.*, vol. 82, pp. 3472-3475, Apr. 1999.
- [77] A. Gupta, D. Akin and R. Bashir, "Single virus particle mass detection using microresonators with nanoscale thickness," *Appl. Phys. Lett.*, vol. 84, pp. 1976-1978, Jan. 2004.
- [78] G. Binnig, C. F. Quate and C. Gerber, "Atomic force microscope," *Phys. Rev. Lett.*, vol. 56, pp. 930-933, Mar. 1986.
- [79] P. Sheehan, L. Whitman, W. King and B. Nelson, "Nanoscale deposition of solid inks via thermal dip pen nanolithography," *Appl. Phys. Lett.*, vol. 85, pp. 1589-1591, Jul. 2004.
- [80] H. J. Mamin and D. Rugar, "Thermomechanical writing with an atomic force microscope tip," *Appl. Phys. Lett.*, vol. 61, pp. 1003-1005, Aug. 1992.

- [81] S. Beeby, M. Tudor and N. White, "Energy harvesting vibration sources for microsystems applications," *IOP Meas. Sci. Tech.*, vol. 17, pp. 175-195, Dec. 2006.
- [82] Y. Wang, M. Bachman, G. P. Li, S. Guo, B. J. F. Wong and Z. Chen, "Low-voltage polymer-based scanning cantilever for *in vivo* optical coherence tomography," *Opt. Lett.*, vol. 30, pp. 53-55, Jan. 2005.
- [83] A. Lal, R. Duggirala and H. Li, "Pervasive power: A radioisotope-powered piezoelectric generator," *IEEE Perva. Comput.*, vol. 4, pp. 53-61, Jan. 2005.
- [84] J. W. Cooley and J. W. Turkey, "An algorithm for the machine calculation of complex fourier series," *Math. Comput.*, vol. 19, pp. 297-301, Apr. 1965.
- [85] E. O. Brigham and R. E. Morrow, "The fast fourier transform," *IEEE Spectrum*, vol. 4, pp. 63-70, Oct. 1967.
- [86] V. Kotipalli, Z. Gong, P. Pathak, T. Zhang, Y. He, S. Yadav and L. Que, "Light and thermal energy cell based on carbon nanotube films," *Appl. Phys. Lett.*, vol. 97, pp. 21-23, Sept. 2010.
- [87] P. Avouris, M. Freitag and V. Perebeinos, "Carbon-nanotube photonics and optoelectronics," *Nature Phot.*, vol. 2, pp. 341-350, Nov. 2008.
- [88] M. E. Itkis, F. Borondics, A. Yu and R. C. Haddon, "Bolometric infrared photoresponse of suspended single-walled carbon nanotube films," *Science*, vol. 312, pp. 415-416, Apr. 2006.
- [89] J. Abrahamson, W. Choi, N. Schonenbach, J. H. J. Park, M. Walsh, K. Kalantar-zadeh and M. Strano, "Wavefront velocity oscillations of carbon-nanotube-guided thermopower waves: nanoscale alternating current sources," *ACS Nano*, vol. 5, pp. 367-375, Dec. 2010.
- [90] H. A. Sodano and D. J. Inman, "Comparison of piezoelectric energy harvesting devices for recharging batteries," *J. Intel. Mat. Syst. Str.*, vol. 16, pp. 799-807, Oct. 2005.
- [91] C. Easter and C. O'Neal, "Annealing procedures and their effects on PZT/nanoparticle thin films via a modified sol-gel process," *in Proc. IMECE07*, 2007, pp. 1225-1231.
- [92] J. W. Lee, J. J. Choi, G. T. Park, C. S. Park and H. E. Kim, "Thick Pb(Zr, Ti)O<sub>3</sub> film fabricated by inducing residual compressive stress during the annealing process," *J. Mat. Res.*, vol. 20, pp. 2898-2901, Jul. 2005.

- [93] A. Behnam, Y. Choi, L. Noriega, Z. Wu, I. Kravchenko, A. G. Rinzler and A. Ural, "Nanolithographic patterning of transparent, conductive single-walled carbon nanotube films by inductively coupled plasma reactive ion etching," *J. Vac. Sci. Technol. B*, vol. 25, pp. 348-354, Feb. 2007.
- [94] A. Kholkin, D. Taylor and N. Setter, "Poling effect on piezoelectric properties of lead zirconate titanate thin films," in *Proc. Int. Symp. Appl. Ferroelec.*, 1998, pp. 69-72.
- [95] J. Cheng, L. He, L. Che and Z. Meng, "Lead zirconate titanate thin films prepared on metal substrates by the sol-gel methods," *Thin Solid Films*, vol. 515, pp. 2398-2402, Jun. 2006.
- [96] T. S. Philips, *Dynamo-Electric Machinery: A Manual for Students of Electrotechnics*, BiblioLife, 2009.
- [97] M. A. Green, "Intrinsic concentration, effective densities of states, and effective mass in silicon," *J. Appl. Phys.*, vol. 67, pp. 2944-2954, Mar. 1990.
- [98] F. Salleh, K. Asai, A. Ishida and H. Ikeda, "Seebeck coefficient of ultrathin silicon-on-insulator layers," *Appl. Phys. Exp.*, vol. 2, pp. 071203, Jul. 2009.
- [99] J. Chen, K. R. Udayakumar, K. G. Brooks and L. E. Cross, "Rapid thermal annealing of sol-gel derived lead zirconate titanate thin films," *J. Appl. Phys.*, vol. 71, pp. 4465-4469, May 1992.
- [100] J. Lu, Y. Zhang, T. Ikehara, T. Mihara and R. Maeda, "Effects of rapid thermal annealing on nucleation, growth, and properties of lead zirconate titanate films," *IEEE T. Ultrason. Ferr.*, vol. 54, pp. 2548-2554, Dec. 2007.
- [101] D. M. Schaadt, B. Feng and E. T. Yu, "Enhanced semiconductor optical absorption via surface plasmon excitation in metal nanoparticles," *Appl. Phys. Lett.*, vol. 86, pp. 61-63, Feb. 2005.
- [102] C. Rockstuhl, S. Fahr and F. Lederer, "Absorption enhancement in solar cells by localized plasmon polaritons," *J. Appl. Phys.*, vol. 104, pp. 1231021-1231027, Dec. 2008.
- [103] D. K. Kotter, S. D. Novack, W. D. Slafer and P. Pinhero, "Solar nantenna electromagnetic colletors," in *Proc. ES2008*, 2008, pp. 1-7.
- [104] V. E. Ferry, L. A. Sweatlock, D. Pacifici and H. A. Atwater, "Plasmonic nanostructure design for efficient light coupling into solar cells," *Nano Lett.*, vol. 8, pp. 4391-4397, Nov. 2008.

- [105] Y. Li, W. Lu, Q. Huang, M. Huang, C. Li and W. Chen, "Copper sulfide nanoparticles for photothermal ablation of tumor cells," *Nanomedicine*, vol. 5, pp. 1161-1171, Oct. 2010.
- [106] P. Benitez and J. C. Minano, *Concentrator optics for the next-generation photovoltaics*, Taylor & Francis, 2004.